Dissertation

zur Erlangung des Grades eines
Doktors der Naturwissenschaften (Dr. rer. nat.)

Functionalisation of 2D-Semiconductors with Organic Molecules

---

vorgelegt von

J. Rika Simon

Freie Universität Berlin
Fachbereich Physik

28.03.2024
Berlin

Berlin, den 28. März 2024
Erstgutachterin: Prof. Dr. Katharina J. Franke
Zweitgutachter: Prof. Dr. Wolfgang Kuch
Datum der Disputation: 10. Juli 2024

Ad astra per aspera.

Abstract

Combining organic molecules with inorganic substrates, especially two-dimensional materials such as transition-metal dichalcogenides (TMDCs), is a wide field with much interest and many possibilities. Finding the right combination to achieve a purposeful union with desired properties requires a detailed examination of the fundamental processes that occur in these hybrid systems. Scanning tunnelling microscopy (STM) and spectroscopy (STS) are ideal tools for investigating these hybrid systems, as they allow us to employ their powerful capabilities of local spatial resolution on the atomic scale, resulting in direct access to the local electronic structure. The locality of electronic effects is a crucial piece of information in reaching a full understanding of the various mechanisms at play.

In this thesis, we utilise STM and STS to investigate three different hybrid systems under three different aspects: In the first part, we create and explore the system of trifluoromethyl-terphenyl-thiol (CF_3-3P-SH) molecules on Au(111) and MoS_2/Au(111) and the various adsorption properties. We compare physisorption on both surfaces of Au(111) and MoS_2/Au(111), and chemisorption, facilitated by successfully anchoring the CF_3-3P-S(H) molecules to purposefully created S-vacancies in the MoS_2 monolayer. The anchoring molecules are identified by their rotation around one of their terminations. We observe two different species of anchored molecules that differ only in their electronic structure: the majority shows nothing around the Fermi energy, whereas a small percentage exhibits a peak at zero bias which we assign to a Kondo resonance. This chemisorption process is disentangled at the atomic level by combining experiment and theory in collaboration. Detailed analysis of the stability of the hybrid system, *ab-initio* molecular dynamics simulations and DFT calculations confirm that two different molecular species are involved: intact CF_3-3P-SH and dehydrogenated CF_3-3P-S. Both show electronic states inside the bandgap of MoS_2 which crucially differ in their occupation.

Secondly, we further explore the capabilities of MoS_2 as a decoupling layer that enhances the lifetime of molecular states inside its bandgap. Using the model system of single vanadyl-naphthalo-cyanine (VONc) molecules adsorbed on MoS_2/Au(111), we study the electronic states of this molecule in detail. We identify the observable in-gap states and analyse the local variations in the electronic structure which are determined to be caused by the tip-perturbation potential as well as vibration-induced effects such as vibration-assisted tunnelling.

In the last part, we investigate the capabilities of bulk 2H-$MoTe_2$ as a substrate for STM, identifying and exploring its inherent n-type semiconductor characteristics and the importance of choosing suitable molecular adsorbates such as tetrathiofulvalene (TTF) molecules which show signs of charge transfer with the substrate. Various naturally occurring defects of $MoTe_2$, showing strong states in the bandgap of $MoTe_2$, are observed as well. These states are imaged spatially using $\mathrm{d}I/\mathrm{d}V$ maps.

Kurzfassung

Das Kombinieren von organischen Molekülen mit anorganischen Substraten, insbesondere zweidimensionalen Materialien wie Übergangsmetalldichalcogeniden, spannt ein weites Feld auf, an dem intensiv geforscht wird und das unzählige Möglichkeiten bietet. Innerhalb dieser Vielzahl von Möglichkeiten die richtige Kombination an Materialien mit den gewünschten Eigenschaften zu finden, benötigt detailliertes Wissen über die Prozesse, die in diesen Systemen stattfinden. Insbesondere in Fällen, die räumliche Auflösung auf atomarer Ebene benötigen, ist das Rastertunnelmikroskop (RTM) das Instrument der Wahl. Zusammen mit Rastertunnelspektroskopie (RTS) ermöglicht uns das RTM, hochlokalisierte elektronische Strukturen und Prozesse zu untersuchen, und liefert uns damit essentielle Informationen über die verschiedensten Effekte in diesen Systemen.

In der vorliegenden Arbeit werden drei verschiedene solcher Systeme unter drei verschiedenen Gesichtspunkten mithilfe von RTM/RTS untersucht: Zunächst beschäftigen wir uns mit dem Molekül Trifluoromethyl-terphenyl-thiol (CF_3-3P-SH) auf Au(111) und MoS_2/Au(111), das verschiedene Adsorptionseigenschaften zeigt. Ein besonderer Fokus liegt hierbei auf der erfolgreichen Bindung von CF_3-3P-S(H) Molekülen an eigens dafür erzeugten, einzelnen Schwefeldefekten in der obersten Schicht der MoS_2-Monolage. Diese verankerten Moleküle lassen sich anhand ihrer Rotation um eines ihrer Enden identifizieren. Außerdem finden sich zwei verschiedene Varianten an verankerten Molekülen, die sich nur in ihrer elektronischen Struktur voneinander unterscheiden lassen: Die meisten Moleküle zeigen nichts um die Fermienergie herum, während ein kleiner Anteil eine Resonanz bei 0 V aufweist, welche wir dem Kondo-Effekt zuweisen. Durch erfolgreiche Kooperation zwischen Experiment und Theorie erreichen wir ein fundamentales Verständnis des Verankerungsprozesses auf atomarer Ebene. Detaillierte Stabilitätsanalysen, *ab-initio* Molekulardynamik-Simulationen und Dichtefunktionaltheorie-Rechnungen bestätigen die Existenz von zwei molekularen Varianten: intaktes CF_3-3P-SH and dehydriertes CF_3-3P-S, welche unterschiedliche Zustände in der Bandlücke von MoS_2 aufweisen, die in maßgeblicher Weise unterschiedlich besetzt sind.

Als nächstes wird MoS_2 als Entkopplungsschicht weiter untersucht, welches die Lebensdauer der molekularen Zustände innerhalb der Bandlücke verlängert. Wir untersuchen die elektronischen Zustände innerhalb des Modellsystems Vanadyl-naphthalo-cyanine (VONc) auf MoS_2/Au(111) und identifizieren die molekularen Zustände innerhalb der Bandlücke von MoS_2. Außerdem lässt sich eine Verschiebung in der Energie der Zustände beobachten, die mit der Position über dem Molekül korreliert. Dieser Effekt wird identifiziert als eine Auswirkung des Spitzenstörpotentials in Kombination mit vibrationsbasierten Effekten wie das Tunneln über die Vibrationszustände.

Im letzten Teil dieser Arbeit wird der Halbleiter 2H-$MoTe_2$ in Hinsicht auf seine Möglichkeiten in der RTM untersucht, wobei inhärente n-Halbleitereigenschaften identifiziert werden und die damit verbundene notwendige gezielte Auswahl an zu adsorbierenden Molekülen ergründet wird. Eines dieser Moleküle ist der Elektronendonator Tetrathiofulvalene (TTF), welcher Anzeichen von Ladungstransfer mit dem Substrat aufweist. Außerdem werden verschiedene natürlich vorkommende Defekte in $MoTe_2$ untersucht, welche Zustände in der Bandlücke von $MoTe_2$ zeigen. Diese Zustände werden mithilfe von $\mathrm{d}I/\mathrm{d}V$-Messungen auf ihre räumliche Verteilung untersucht.

Contents

1 Introduction

Es ist ein weites Feld.
— Theodor Fontane, *Effi Briest*

In a world that always aches for constant improvement, to be newer, better, faster, be it personally, socially or economically, technology is one of the main driving forces of progress. This driving force has been founded on silicon-based systems in the last ~ 30 years, specifically the continuous improvement of the transistor, but we are reaching the physical limits of this approach, even though innovation continues to push the boundaries. But once innovation inevitably stops, it comes with the price of relying on outdated technology which is squeezed and optimised to its very limits, long past the point of diminishing returns with whole sectors unable or unwilling to embrace change. The costs of missing a structural change are grave.

Hence it is time to look for alternatives, and no small amount of research has already been invested in finding them. Two popular avenues to pursue are the quantum computer, creating qubits utilising structures on the atomic scale, and the use of two-dimensional systems to create new hybrid materials with better properties than their silicon-based ancestors, for example in the field of solar cells. Both avenues naturally overlap in some areas.

On the side of hybrid systems lies the wide field of transition-metal dichalcogenides (TMDCs), a group of materials already investigated for more than 60 years, where new and exciting properties are still being discovered to this day. TMDCs offer a staggering amount of different possible material properties and range from insulators to metals to semimetals to semiconductors to even superconductors. This is coupled to their two-dimensional nature, as they are layered materials with their layers only weakly bound together by van-der-Waals forces, allowing for relatively straightforward extraction or growth of single layers. This in turn opens up the door to combined materials, a subject where the Lego-brick analogy is often enlisted to illustrate the cornucopia of choice. This analogy rightfully remains a popular picture, regardless of its limitations that come from neglecting the aspects of strain, twist and defects.

But when talking about hybrid materials, adsorbates on TMDCs are another common ingredient. These can be atomic – most commonly single metal atoms – or molecular in nature. Naturally, the field of 'molecules' is a wide one as well, with chemists able to produce almost any imaginable molecular structure – with limits, of course. These molecules can have many different properties as well, from electron acceptors to electron donors, from flat to three-dimensional, with different spin states or the ability to self-assemble. If you combine these molecules with TMDCs, you cannot but quote Fontane once more: 'Es ist ein weites Feld.' – 'It's a wide field.'

But simply throwing together random molecules and substrates is not a sustainable approach, at least not without foresight. The magic lies in finding the correct combination. This obviously relies on being able to fall back on previous work, and this is the point where working in a field that has already been extensively plowed becomes a real asset and does not imply that no new discoveries are possible, quite the contrary. Because there is a lot of knowledge to rely on, systems can be more specifically tailored to produce the desired results, such as self-assembly, localised spins for spintronics, creation of in-gap states, bandgap engineering, suitable energy structures for optoelectronics, and the list goes on. To be able to combine materials in a successful way, fundamental understanding of what happens at the interface is necessary.

Frequently, very local effects need to be explored to gain this knowledge, for example when studying single molecules or defects on a surface. The measurement technique of choice is therefore scanning tunnelling microscopy (STM), since its spatial resolution on the atomic scale makes it ideally suited to explore highly local effects. Scanning tunnelling spectroscopy (STS) makes it possible to probe the local electronic structure, and the precise control over the STM tip gives us the ability to manipulate atomic and molecular structures. Exploring the fields of hybrid systems with STM as the tool allows us to utilise many of its powerful capabilities.

Aspects of hybrid systems that can be explored with STM exceptionally well are the physisorption and chemisorption properties of single molecules. The interactions between adsorbate and substrate are highly local effects which allow for careful tuning of the electronic structure of the hybrid system. At the same time, the pristine, unmodified substrate can be studied, which allows for precise comparison between the systems.

In this thesis we will explore what is possible when combining materials purposefully for three different hybrid systems, and the physical insights that can be gained from the STM/STS measurements. We will compare the interaction between organic molecules and inorganic 2D-semiconductors of these three systems, focusing on different aspects in each part:

The first system is specifically chosen to anchor molecules on a TMDC monolayer, creating atomic surface defects as anchoring points for the tailored endgroup of the molecules. Through the covalent bond formed between adsorbate and substrate, the electronic structure of the resulting hybrid system is modified. This anchoring mechanism could be used to carefully tune the electronic structure by adjusting the properties of the anchored molecule.

The second system explores how the stable physisorption of molecules on TMDC monolayers allows us to access molecular states with an energy resolution not achievable on metals. This in turn makes it possible to explore the vibronic states of the molecule and how they influence the measured electronic structure.

The last system to be investigated is not a monolayer on a metal, but a bulk 2D-semiconductor TMDC. Here we can explore how the lack of direct access to the electron reservoir of a metal affects the electronic properties, and what might be possible in regard to defect functionalisation and adsorption of molecules, and how this changes the electronic structure of the system.

Following these phenomena, this thesis is structured in the following way: After the general introduction and exposition given in this chapter, *Chapter 2* will begin by introducing the theoretical background that forms the foundation upon which the results of this thesis are built. Starting with the fundamental principles behind the STM and the technique of STS, without which none of the measurements in this thesis would be possible, we continue with a general introduction to the main characters of this thesis: transition-metal dichalcogenides (TMDCs). The materials MoS_2 and $MoTe_2$ are introduced, followed by a brief overview of the properties of molecular adsorbates. The physics behind double-barrier junctions and the effects on the measured electronic structure by the tip-perturbation potential are explored, as well as vibronics and the processes involved in vibration-assisted tunnelling (VAT), acting as a basis for the measurements shown in Ch. 4. Lastly, the fundamental aspects of the Kondo effect are briefly introduced, utilising the historical developments around it as a guide.

Chapter 3 acts as an introduction to the more technical aspects needed for this thesis, giving a general overview of the STM as a machine and presents the substrates used in this thesis from a technical point of view: Au(111), MoS_2/Au(111), defected MoS_2/Au(111) and bulk 2H-$MoTe_2$. The chapter details the preparation, growth and cleaning procedures involved to allow the measurements presented in the following three chapters.

Chapter 4 shows different adsorption scenarios of the organic molecule 4"-(trifluoromethyl)-[1,1':4',1"-terphenyl]-4-thiol (CF_3-3P-SH), both on Au(111) and on MoS_2/Au(111). After introducing the molecule and detailing the preparation steps, we explore the behaviour of CF_3-3P-S(H) in detail on the two substrates, culminating in the anchoring of CF_3-3P-S(H) molecules on purposefully created S-vacancies in the terminating chalcogen layer of the MoS_2 monolayer. We investigate and identify two different species of anchored molecules that differ in their electronic structure, with one of them exhibiting a zero-bias resonance that we attribute to a Kondo resonance. Through the combination of experiment and theory in a fruitful collaboration, the mechanism behind the anchoring process to the S-vacancies is investigated at an atomic level and we identify the two molecular species as the intact CF_3-3P-SH and the dehydrogenated CF_3-3P-S molecule which both create in-gap states with different occupations. The latter molecule's defect state is singly occupied which gives rise to the Kondo resonance.

Chapter 5 explores the system of vanadyl-naphthalo-cyanine (VONc) molecules on MoS_2/Au(111) with a special focus on the electronic and vibronic properties of the molecular states, showcasing the strength of MoS_2 as a decoupling layer from the metal substrate underneath that enhances the lifetime of molecular states. We identify these molecular states visible inside the bandgap of MoS_2 and observe the local variations in the electronic structure when moving across the molecule. Using DFT calculations of the gas-phase molecule, we identify and investigate the effects of the tip-perturbation potential and vibration-assisted tunnelling.

Chapter 6 introduces bulk 2H-$MoTe_2$ as a substrate for STM. We explore its general properties in STM and the challenges involved in contacting a 2D-material. Moreover, we identify 2H-$MoTe_2$ as an inherent n-type semiconductor, as well as taking a detailed look at the different species of defects naturally present. Finally, we investigate adsorption properties of the electron acceptor molecule 2,3,5,6-tetrafluoro-7,7,8,8-tetracyanoquino-

dimethane (F_4-TCNQ) and the electron donor molecule tetrathiofulvalene (TTF) on the n-type semiconductor.

Now let us raise the curtain with the words of J. W. Goethe in *Faust*: 'Der Worte sind genug gewechselt, Laßt mich auch endlich Taten sehn!' – 'The words you've bandied are sufficient; 'Tis deeds that I prefer to see!'.

2 Theoretical Background

2.1 Scanning Tunnelling Microscopy

In 1982, the invention of the scanning tunnelling microscope (STM) by Gerd Binnig and Heinrich Rohrer brought on a new era for surface science [1–3]: Now it was possible to image beyond the optical diffraction limit on a subatomic scale coupled with the ability to measure the local electronic structure with high spatial resolution. The scientific community acknowledged the groundbreaking nature of their invention and only four years later, in 1986, the two inventors were honoured with half a Nobel prize [4].

This chapter will give a general introduction into the working principle of the STM and the physical background needed to interpret the obtained data.

At the heart of the STM lies the tunnelling effect: A current can flow between two contacts, even though they are separated by a classically insurmountable barrier. The electrons therefore 'tunnel' through the barrier, or more precisely: the wavefunction ψ of the electron crosses the barrier with an exponentially decaying amplitude, as sketched in Fig. 2.1a.

In an STM, the two contacts are a conducting sample surface and a conducting tip that are a few Ångstrom apart and therefore separated by a vacuum barrier. The height of the vacuum barrier is governed by the material specific workfunctions of tip Φ_t and sample Φ_s. Without an external bias voltage applied to the junction, the Fermi levels of both materials are aligned, as sketched in Fig. 2.2a. Even though tunnelling events are already possible, they occur in both directions with the same probability and thus cancel each other out. No measurable tunnelling current is produced.

Applying a bias voltage between tip and sample shifts the chemical potentials of tip and sample with respect to each other as shown in Fig. 2.2b. Now tunnelling from the occupied states into the unoccupied states produces a directed, and therefore measurable, current flow. The ability to change and sweep the applied bias voltage also allows for probing the local electronic structure, as will be shown in more detail in the next section.

The theoretical description of the tunnelling current in an STM and how it relates to the (local) density of states ((L)DOS) was developed by J. Tersoff and D. R. Hamann in 1983 [5]. To analytically describe the tunnelling processes in an STM, they assume an atomically sharp, spherical conducting tip with radius R at position $\boldsymbol{r_0}$ in a distance z from the flat conducting surface, as sketched in Fig. 2.1b. The details of these assumptions will enter at a later point in their derivation, which we will follow here.

To begin, Tersoff and Hamann evaluate the tunnelling current $I_{t\to s}$ from tip to sample between all possible initial states of the tip ψ_μ at energy E_μ and final states ψ_ν of the

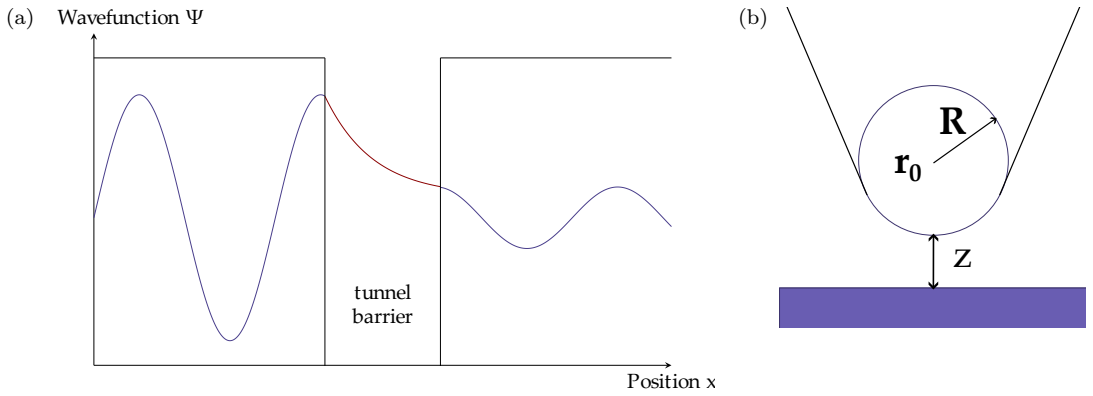

Figure 2.1: (a) An exemplary wavefunction ψ passing through a tunnelling barrier with the amplitude decaying exponentially inside the barrier. (b) Model of the STM tunnelling junction in the Tersoff-Hamann approach. An atomically sharp, spherical tip with radius R at position $\boldsymbol{r_0}$ is at a distance z from the flat sample surface.

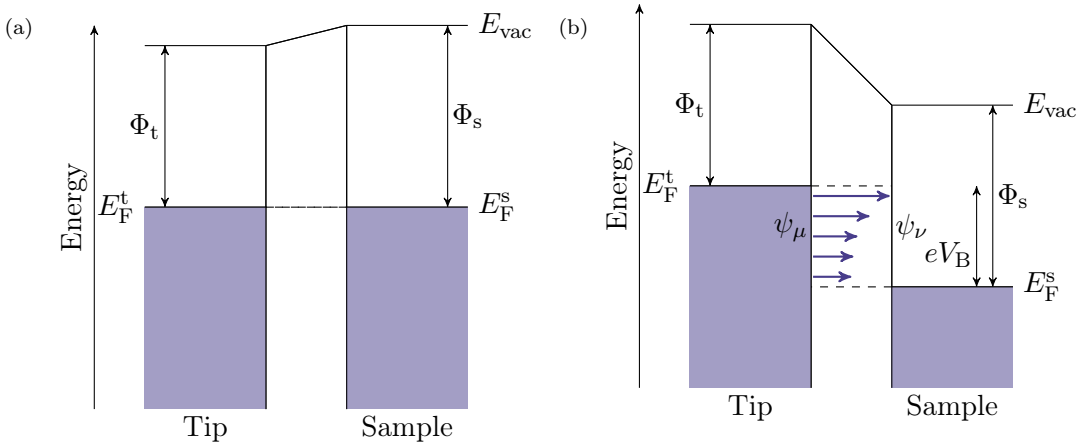

Figure 2.2: Energy level diagram of the STM tunnelling junction: Tip and sample are separated by a tunnelling barrier, the height of which is governed by the workfunctions Φ_t and Φ_s of tip and sample. (a) When no external bias voltage is applied, the Fermi energies E_F of tip and sample align. Random tunnelling processes can occur, but without any set direction. No measurable tunnelling current is produced. (b) The applied bias voltage V_B shifts the Fermi levels of tip and sample. Now, directed tunnelling can occur between the occupied states of the tip (as depicted here) into the unoccupied states of the sample. This primarily probes the unoccupied states of the sample that align with the Fermi level of the tip.

sample at energy E_ν given by first order perturbation theory [5]:

$$I_{t\to s} = \frac{4\pi e}{\hbar} \sum_{\mu\nu} f(E_\mu)[1 - f(E_\nu)] \, |M_{\mu\nu}|^2 \, \delta(E_\mu - E_\nu - eV) \; . \tag{2.1}$$

Here, the Fermi-Dirac distribution $f(E) = \left(\exp\left(\frac{E-E_F}{kT}\right) + 1\right)^{-1}$ describes the occupation probability of a state at energy E, the applied bias voltage enters as V and $M_{\mu\nu}$ is the tunnelling matrix element, which will be evaluated in more detail later on in this section. An additional factor of two takes the two possible spin orientations into account.

The total tunnelling current I flowing between tip and sample consists of both directions $I_{t\to s}$ and $I_{s\to t}$ [6], where the latter is derived in the same way as Eq. (2.1). We therefore get:

$$\begin{aligned} I &= I_{t\to s} + I_{s\to t} && (2.2)\\ &= \frac{4\pi e}{\hbar} \sum_{\mu\nu} f(E_\mu)[1 - f(E_\nu)] \, |M_{\mu\nu}|^2 \, \delta(E_\mu - E_\nu - eV) \\ &\quad - \frac{4\pi e}{\hbar} \sum_{\mu\nu} f(E_\nu)[1 - f(E_\mu)] \, |M_{\mu\nu}|^2 \, \delta(E_\nu - E_\mu - eV) && (2.3)\\ &= \frac{4\pi e}{\hbar} \sum_{\mu\nu} [f(E_\mu) - f(E_\nu)] \, |M_{\mu\nu}|^2 \, \delta(E_\mu - E_\nu - eV) \; . && (2.4) \end{aligned}$$

Utilising the fact that the DOSes of tip $\rho_\mathrm{t}(E)$ and sample $\rho_\mathrm{s}(E)$ are continuous, this sum over individual states can be turned into an integral over energies, with the assumption that the same $M_{\mu\nu}$ governs all states with equal energy:

$$I = \frac{4\pi e}{\hbar} \int_{-\infty}^{\infty} \mathrm{d}E_\mu \int_{-\infty}^{\infty} \mathrm{d}E_\nu \, |M_{\mu\nu}|^2 \, [f(E_\mu) - f(E_\nu)] \, \rho_\mathrm{t}(E_\mu)\rho_\mathrm{s}(E_\nu)\delta(E_\nu - E_\mu - eV) \; . \tag{2.5}$$

After evaluating the integral over E_μ without loss of generality and renaming the remaining E_ν to E, we arrive at:

$$I = \frac{4\pi e}{\hbar} \int_{-\infty}^{\infty} \mathrm{d}E \, |M_\mathrm{E}|^2 \, [f(E - eV) - f(E)] \, \rho_\mathrm{t}(E - eV)\rho_\mathrm{s}(E) \; . \tag{2.6}$$

Now some experimental aspects enter the derivation. The experiments are conducted at low temperatures which means room temperature or usually even lower temperatures (4 K or 77 K for the data shown in this thesis). In this case, the features to be measured are mostly much broader than the temperature broadening of the Fermi-Dirac distribution $f(E)$, which can therefore be approximated with a step function. Since only states between the Fermi energies E_F of tip and sample contribute to the tunnelling current (as depicted in Fig. 2.2b), we can change the limits of our integral to E_F and $E_\mathrm{F} + eV$.

Keeping all these considerations in mind, our integral turns into:

$$I = \frac{4\pi e}{\hbar} \int_{E_\mathrm{F}}^{E_\mathrm{F}+eV} \mathrm{d}E \, |M_\mathrm{E}|^2 \, \rho_\mathrm{t}(E - eV)\rho_\mathrm{s}(E) \ . \tag{2.7}$$

Here we can already see that the tunnelling current depends on the convoluted DOSes of tip and sample, we can thus access ρ_s through measuring I. This is an essential aspect for scanning tunnelling spectroscopy, which will be elaborated on in the following section.

But first we turn our attention to the topographical imaging capabilities of the STM. So far, Eq. (2.7) shows no apparent dependence on the tip-sample distance and therefore the real-space features of the sample to be measured. To understand this connection, we have to consider the tunnelling matrix element $M_{\mu\nu}$ in more detail.

In 1961, more then twenty years before the invention of the STM, J. Bardeen evaluated the tunnelling matrix element $M_{\mu\nu}$ for a system consisting of two separated regions governed by two independent wavefunctions (let us call them ψ_μ and ψ_ν) in a many-body point of view [7]. $M_{\mu\nu}$ relates these two wavefunctions with each other, or, more precisely, describes how ψ_μ is projected onto ψ_ν upon perturbation with the surface potential. In such a case, $M_{\mu\nu}$ can be expressed as a surface integral over the surfaces inside the tunnelling barrier [7]:

$$M_{\mu\nu} = -\frac{\hbar^2}{2m} \int_S \mathrm{d}\boldsymbol{S} \cdot (\psi_\mu^* \nabla\psi_\nu - \psi_\nu \nabla\psi_\mu^*) \ . \tag{2.8}$$

Since the described case is directly applicable to an STM tunnelling junction with wavefunctions ψ_μ and ψ_ν for the tip and sample, respectively, Tersoff and Hamann utilise Eq. (2.8) to continue their evaluation. They now turn their attention to the surface potential and assume that it is periodic in space within the region contributing to tunnelling, which is the case for the majority of substrates. This means that the surface wavefunction ψ_ν can be expanded with Bloch wavevectors into [5]:

$$\psi_\nu = \frac{1}{\sqrt{\Omega_\mathrm{s}}} \sum_G a_G \exp\left\{-\sqrt{\kappa^2 + \left|\boldsymbol{k}_\parallel + \boldsymbol{G}\right|^2} z\right\} \cdot \exp\left\{i\left(\boldsymbol{k}_\parallel + \boldsymbol{G}\right) \cdot \boldsymbol{r}_\parallel\right\} \ , \tag{2.9}$$

where Ω_s is the sample volume, a_G a normalisation constant, κ the inverse decay length for the wavefunction into vacuum, $\boldsymbol{r}_\parallel$ the spatial vector parallel to the surface, $\boldsymbol{k}_\parallel$ the surface Bloch wavevector and $\boldsymbol{G}$ a surface reciprocal-lattice vector. In the case of a non-periodic surface, the sum over G turns into an integral [5].

As initially stated, the wavefunction of the tip ψ_μ is assumed to be of s-wave character and therefore spherical[1)]. In a similar expansion as in Eq. (2.9), ψ_μ therefore becomes [5]:

$$\psi_\mu = \frac{1}{\sqrt{\Omega_\mathrm{t}}} c_\mathrm{t} \kappa R \frac{\exp\{\kappa R\}}{\kappa \left|\boldsymbol{r} - \boldsymbol{r_0}\right|} \exp\{-\kappa \left|\boldsymbol{r} - \boldsymbol{r_0}\right|\} \ , \tag{2.10}$$

[1)] For treatment of non-s-wave tips see for example: [8–10].

where Ω_t is the probe volume, c_t a normalisation constant, and R and $\boldsymbol{r_0}$ are defined as in the beginning and shown in Fig. 2.1b.

At this point we take a moment to consider the decay constant κ in more detail. For κ, the model assumed for the shape of the tunnelling barrier plays an important role. Usually, the non-constant barrier is simplified by using the average barrier height approximation from the Wentzel-Kramers-Brillouin (WKB) approach, meaning that the workfunctions Φ_t and Φ_s are simply averaged with $\Phi_\mathrm{avg} = \frac{\Phi_\mathrm{t}+\Phi_\mathrm{s}}{2}$, leading to a rectangular barrier with height of $\Phi_\mathrm{avg} + eV$. In such a case, κ becomes [11]:

$$\kappa = \sqrt{\frac{2m}{\hbar^2}\left(\Phi_\mathrm{avg} - E + \frac{eV}{2}\right)} \ , \tag{2.11}$$

assuming that only electrons close to the Γ point are involved in the tunnelling [11]. If this is not the case, an additional term of $\boldsymbol{k}_\parallel$, the parallel momentum of the surface state, has to be taken into account and κ becomes [11]:

$$\kappa = \sqrt{\frac{2m}{\hbar^2}\left(\Phi_\mathrm{avg} - E + \frac{eV}{2}\right) + \boldsymbol{k}_\parallel^2} \ . \tag{2.12}$$

The bigger $\boldsymbol{k}_\parallel$ becomes, the bigger the decay constant κ. It follows that states with a high $\boldsymbol{k}_\parallel$ do not contribute significantly to the tunnelling current, or, put differently, that STM is not very sensitive to these states.

Tersoff and Hamann continue their derivation by inserting Eq. (2.9) and (2.10) into Eq. (2.8) and evaluate the resulting expression further. They finally arrive at [5]:

$$M_{\mu\nu} = \frac{4\pi\hbar^2}{2m}\frac{R}{\sqrt{\Omega_\mathrm{t}}}\exp(\kappa R)\psi_\nu(\boldsymbol{r_0}) \ , \tag{2.13}$$

which is proportional to $\psi_\nu(\boldsymbol{r_0})$. Combining this with Eq. (2.7) leads to:

$$I \propto \int_{E_\mathrm{F}}^{E_\mathrm{F}+eV} \mathrm{d}E \left|\exp(\kappa R)\psi_\nu(\boldsymbol{r_0})\right|^2 \rho_\mathrm{t}(E-eV)\rho_\mathrm{s}(E) \ . \tag{2.14}$$

Since the wavefunction decays into the tunnelling barrier exponentially, we can use [5]:

$$|\psi_\nu(\boldsymbol{r_0})|^2 \propto \exp(2\kappa(R+z)) \ . \tag{2.15}$$

Adding once more the assumption of low temperatures and small bias voltages, we reach a linear dependence of the tunnelling current I on the bias voltage V, the DOS of the sample ρ_s, an exponential dependence on κ and finally, the vertical distance between tip and sample z. This captures the ability of the STM to record highly resolved topographic information through the tunnelling current. As a rule of thumb, a change in z of 1 Å leads to a change in current of approximately one order of magnitude.

The topography can be recorded in two different main working modes of the STM: constant height and constant current, depicted in Fig. 2.3. In constant-height mode, the

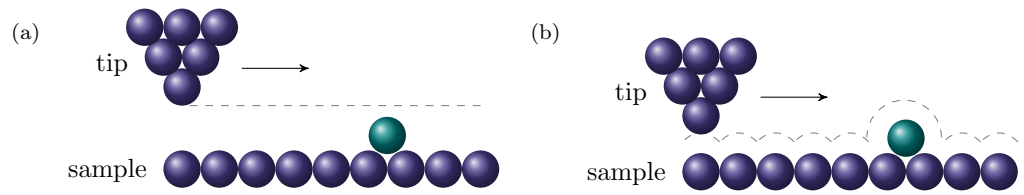

Figure 2.3: Visual representation of the two measuring modes of STM: (a) Constant height mode, where the tip is kept at a fixed absolute position. The topographic information is recorded in the changes of the current. A sufficiently high tip position has to be chosen to avoid unintentional contact with the surface while being close enough to maintain a good signal-to-noise ratio. (b) Constant current mode, where the current between tip and sample is kept constant, and the tip moved vertically to accommodate. The topographic information is therefore contained in the changes of z.

tip is kept at a constant absolute distance from the substrate and the changes in current are recorded. These reflect the changes in the topography. This mode has the advantage of directly recording I which will become useful in imaging 'maps' of different physical properties, as will be explained in the following section. A main drawback is that sudden changes in topography might lead to either a loss of signal or an uncontrolled crash into the sample surface which can lead to deformation of the tip and/or destruction of the locality to be probed.

This risk is mitigated in the second mode, constant current. Here, a feedback loop keeps the tunnelling current constant at the so-called current setpoint, meaning that the relative distance between tip and substrate stays constant (not considering drastic changes in conductivity). The topographic information is therefore recorded in the z-channel.

For both modes it has to be kept in mind that the 'topography' measured with an STM is always the convolution of topography in the sense of surface structure, the electronic structure, i. e. the surface wavefunctions, and the shape and properties of the tip.

2.2 Scanning Tunnelling Spectroscopy

STM is not only a powerful tool to resolve surface features, but also to probe the local electronic structure with atomic precision. This technique is called scanning tunnelling spectroscopy (STS). As shown in the previous section in Eqs. (2.14) and (2.15), the tunnelling current depends on the DOSes of tip and sample. If we now reinsert the variable $M_{\mu\nu}$ for brevity and neglect its energy dependence, we reach:

$$I \propto |M_{\mathrm{E}}|^2 \int_{E_{\mathrm{F}}}^{E_{\mathrm{F}}+eV} \mathrm{d}E \rho_{\mathrm{t}}(E - eV)\rho_{\mathrm{s}}(E) \ . \tag{2.16}$$

For metallic tips, we can now assume a constant ρ_t and move it out of the integral[2)]. Deriving this expression with respect to the bias voltage V with the help of the Leibniz integral rule yields:

$$\frac{\mathrm{d}I}{\mathrm{d}V} \propto |M_\mathrm{E}|^2 \, \rho_\mathrm{t}(E_\mathrm{F})\rho_\mathrm{s}(E_\mathrm{F}+eV) \; . \tag{2.17}$$

This is the differential conductance $\mathrm{d}I/\mathrm{d}V$, which is directly related to the sample DOS ρ_s. By measuring the $\mathrm{d}I/\mathrm{d}V$, we can therefore probe the local DOS of the sample directly.

To do this experimentally, the tip is kept at a lateral position to be probed and the bias voltage is swept in the desired energy range. $\mathrm{d}I/\mathrm{d}V$ spectra can be recorded in both constant height and constant current mode, as introduced in the previous section, where constant current is the more common of the two. It is also possible to record $\mathrm{d}I/\mathrm{d}V$ 'maps'. Here the spatial distribution of the DOS at a specific energy is recorded by scanning across an area of interest and measuring the amplitude of the $\mathrm{d}I/\mathrm{d}V$ signal at every measurement pixel.

Regardless of measuring mode, the $\mathrm{d}I/\mathrm{d}V$ signal is usually not numerically derived from the tunnelling current I but measured directly. This is achieved with a lock-in amplifier.

The basic working principle of the lock-in measurement technique – also applied in many different scenarios outside of STM/STS – is the mixing of two oscillating voltages, signal V_S and reference V_R, at frequencies ω_S and ω_R:

$$V_\mathrm{S}(t) = V_\mathrm{S}\sin(\omega_\mathrm{S}t+\phi_\mathrm{S}) \tag{2.18}$$

$$V_\mathrm{R}(t) = V_\mathrm{R}\sin(\omega_\mathrm{R}t+\phi_\mathrm{R}) \; , \tag{2.19}$$

with ϕ_S and ϕ_R being the phases of reference and signal, respectively.

Mixing these signals together and utilising a trigonometric identity gives [14]:

$$V_\mathrm{S}(t)V_\mathrm{R}(t) = V_\mathrm{S}V_\mathrm{R}\sin(\omega_\mathrm{S}t+\phi_\mathrm{S})\sin(\omega_\mathrm{R}t+\phi_\mathrm{R}) \tag{2.20}$$

$$= \frac{1}{2}V_\mathrm{S}V_\mathrm{R}\left[\cos(\omega_\mathrm{S}t-\omega_\mathrm{R}t+\phi_\mathrm{S}-\phi_\mathrm{R}) - \cos(\omega_\mathrm{S}t+\omega_\mathrm{R}t+\phi_\mathrm{S}+\phi_\mathrm{R})\right] \; . \tag{2.21}$$

This output consists of two AC signals at the difference and sum frequencies $\omega_\mathrm{S} \pm \omega_\mathrm{R}$. After mixing, a low-pass filter is applied to this output that blocks the AC signal of the second term in Eq. (2.21) completely. The first term would share this fate, unless $\omega_\mathrm{S} = \omega_\mathrm{R}$ holds true. Therefore, only the following DC signal remains [14]:

$$V_\mathrm{S}(t)V_\mathrm{R}(t) = \frac{1}{2}V_\mathrm{S}V_\mathrm{R}\cos(\phi_\mathrm{S}-\phi_\mathrm{R}) \tag{2.22}$$

which is proportional to the amplitude of the signal voltage V_S. This means that all frequencies except the one matching the reference are cancelled out, and therefore only the desired signal is recorded.

[2)] This is not the case for e. g. superconducting tips. There the convolution with the tip DOS has to be taken into account. For more information, see for example: [12, 13].

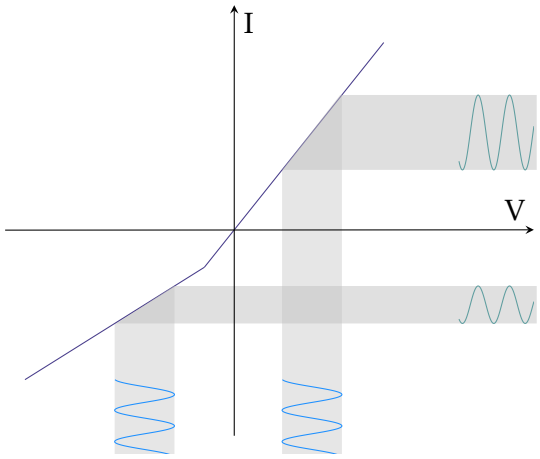

Figure 2.4: Schematic depiction of the lock-in amplifier applied to an I/V curve. The voltage modulation of the lock-in amplifier at a certain frequency and amplitude is applied to certain bias. This modulation in turn leads to a modulation in current, where the amplitude of the resulting signal depends on the slope of the I/V curve. We can therefore measure the $\mathrm{d}I/\mathrm{d}V$ directly.

Additionally, the relative phase between ϕ_S and ϕ_R has to stay constant in time, or the resulting signal will cease to be a DC signal and will consequently be filtered out. This 'locking of phases' is achieved by a phase-locked loop (PLL) of the lock-in amplifier [14], where the phase shift between the phases is kept constant.

How does this now relate to the $\mathrm{d}I/\mathrm{d}V$ in scanning tunnelling spectroscopy? First we have to create a system that allows for lock-in-based signal detection. We therefore add an AC modulation

$$V_\mathrm{mod} = V_\mathrm{S} \sin(\omega_\mathrm{R} t) \tag{2.23}$$

with ϕ_R set to zero for convenience on top of the DC bias voltage V. This results in a total voltage applied to the STM junction of:

$$V_\mathrm{applied} = V + V_\mathrm{mod} \ . \tag{2.24}$$

In this thesis, we follow the convention to give the modulation amplitude as the root-mean-square (RMS) amplitude V_RMS, with $V_\mathrm{RMS} = V_\mathrm{mod}/\sqrt{2}$ for the sinusoidal V_mod. The oscillation frequency of the applied modulation has to be chosen so that it is faster than the feedback loop of the STM, otherwise the z-position of the tip would be influenced by the change in bias. It is also helpful to choose a frequency with little to no inherent noise contribution from the system, so for example no multiples of 50 Hz.

The oscillating bias causes the tunnelling current to oscillate with the same frequency, as illustrated in Fig. 2.4. The figure also shows the effect that changing slopes in the I/V-curve have on the resulting signal: The steeper the slope, the greater the resulting signal. This qualitative relation can be understood in a more formal way by considering the Taylor expansion of the tunnelling current, assuming the modulation V_mod is small

compared to the DC bias:

$$\begin{aligned} I(V_{\text{applied}} = V + V_{\text{mod}}) = I(V) & \\ & + \frac{\mathrm{d}I(V)}{\mathrm{d}V} V_{\text{mod}} \\ & + \frac{\mathrm{d}^2 I(V)}{\mathrm{d}V^2} \frac{V_{\text{mod}}^2}{2} \\ & + \mathcal{O}\left(V_{\text{mod}}^3\right) \ . \end{aligned} \tag{2.25}$$

The first term is the usual tunnelling current at corresponding bias voltage as detected by the STM itself. The second term is of amplitude $\mathrm{d}I/\mathrm{d}V$ and depends through V_{mod} on ω_{R}. This current signal is amplified by the lock-in amplifier, thereby converted to a voltage signal, and, as explained above, multiplied (mixed) by the reference V_{R}. We therefore gain direct experimental access to the $\mathrm{d}I/\mathrm{d}V$, which is in turn proportional to the DOS of the sample to be measured, with a greatly improved signal-to-noise ratio.

2.3 Transition-Metal Dichalcogenides (TMDCs)

Back in 1987, a paper opens with the words '[...] transition metal dichalcogenides [...] have proved a fruitful area of study for solid state physicists for about 20 years [...]' [15]. Now, in 2024, we can still write 'Transition-metal dicalchogenides (TMDCs) have proven to be a fruitful area of study for solid state physicists for more than 50 years'. After a brief lull in popularity, the veritable boom in the world of 2D-materials started by the extraction of graphene via mechanical exfoliation by Andre Geim[3)] and Konstantin Novoselov [17, 18], earning them the Nobel prize in 2010 [17], propagated itself to TMDCs. It was realised that the process of mechanical exfoliation could also be applied to TMDCs, as one – if not the most – intriguing property of TMDCs is that multiple layers are only held together weakly by van-der-Waals forces, much like graphene. The properties of TMDCs can change quite severely depending on the number of layers, and these layers can then also be combined in different ways into new stacked materials [19–23] and even functionalised with molecules [24–26].

All this has opened up a whole new slew of possible applications: TMDCs are mentioned when it comes to the tunability of electronic and optical properties and therefore opto-electronics [27], different states of matter (semiconductors, superconductors, semimetals, etc.) [28], they get attention for possible applications in solar cells [29, 30], nanomechanical systems [31], biosensors [32, 33], field effect transistors [34], and the list goes on.

In this thesis we will focus on two TMDCs, namely MoS_2 and $MoTe_2$. The next subchapter will give a general introduction to the geometrical properties of TMDCs, while the two subchapters 2.3.2 and 2.3.3 will explore the individual materials, their idiosyncrasies and electronic properties in more detail. Later on, in Chapters 4 and 5, we will utilise MoS_2 to study molecular adsorbates in more detail and tune the electronic properties of a composite system.

[3)] Incidentally, the same Andre Geim that made a live frog levitate using the repulsion of diamagnetic objects by magnetic fields [16].

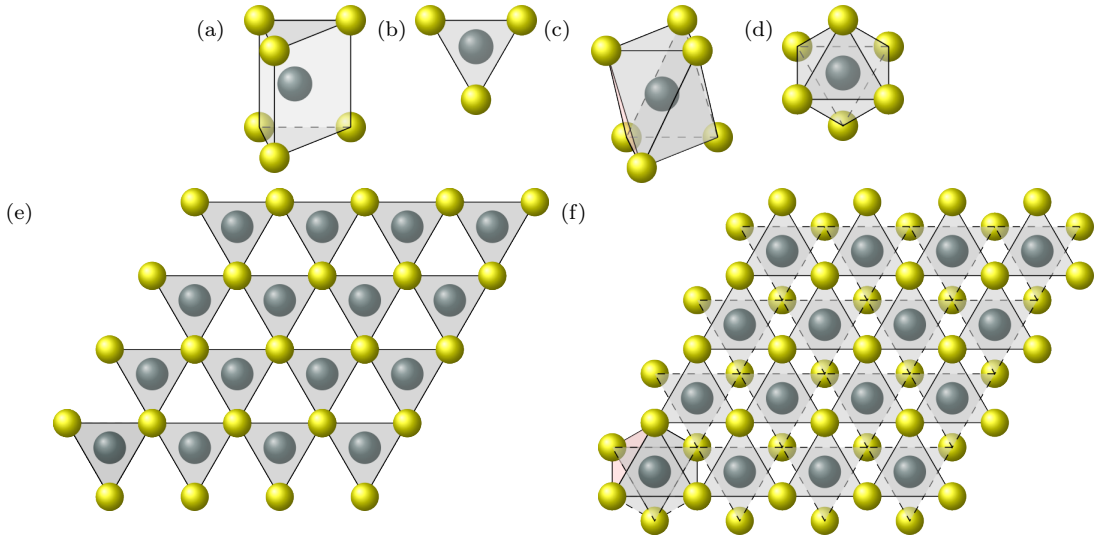

Figure 2.5: Different possible unit cell configurations for TMDCs, with the yellow balls representing chalcogen atoms, and the grey balls representing the metals atoms. (a) Side view and (b) top view of a trigonal prismatic configuration. The chalcogen atoms of the top and bottom layer are right on top of each other. (c) Side view and (d) top view of an octahedral configuration. The chalcogen atoms of the top and bottom layer are rotated by 60° with respect to one another. (e) One layer of a repeated trigonally prismatic unit cell, and (f) repeated octahedral unit cell.

2.3.1 Geometry of TMDCs

TMDCs take the chemical form of MX_2, where M stands for a transition metal (any element in group 3 to 12 in the periodic table of elements, common examples are Mo, W, Nb, etc.) and X for a chalcogen (group 16, therefore S, Se, Te, etc.). The metal layer is 'sandwiched' between two chalcogen layers, in either a trigonal prismatic (AbA, Fig. 2.5a and 2.5b) or an octahedral (AbC, Fig. 2.5c and 2.5d) configuration [35]. Here it has to be kept in mind that while the depicted group consists of one metal atom and six chalcogen atoms, the underlying unit cell is still of the form MX_2. This unit cell is contained to one 'layer' – with TMDCs, the 'sandwich' of the two chalcogen and one metal layer is considered 'one layer' –, so repeated in space it forms two-dimensional sheets as depicted in Fig. 2.5e and 2.5f.

When stacked on top of each other, these 2D-layers can form different stacking sequences. The notation commonly used to denote these sequences is called Ramsdell notation, which classifies stacking sequences of the polytypes with nX, where n is the identity period (the number of layers in a unit cell) and X the lattice type (e. g. H for hexagonal, T for trigonal, R for rhombohedral, etc.) [35, 36]. The stacking sequences most relevant to the materials used in this work are 2H (Fig. 2.6a), 3R (Fig. 2.6b), and 1T (Fig. 2.6c). Distorted forms of 1T are also possible: 1T' and T_d are two different forms of a distorted 1T structure, where a superlattice structure is formed by a structural phase transition [28, 37, 38].

These stacking sequences influence the electronic properties of TMDCs quite severely. Depending on the polytype, the bandstructure of the TMDC changes in such a way that

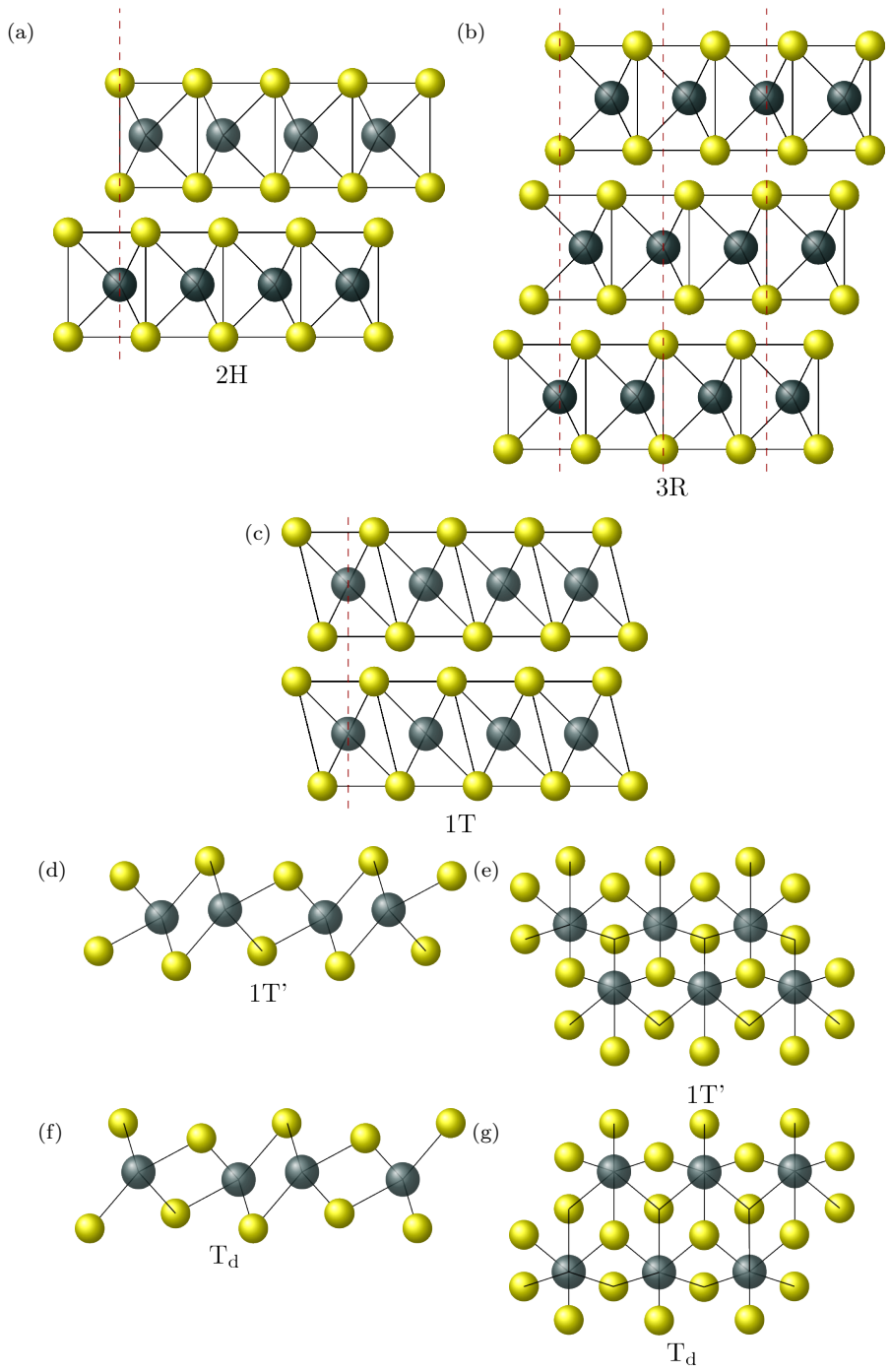

Figure 2.6: Selection of possible stacking sequences of a TMDC: For a trigonally prismatic unit cell, two possible stacking orders are (a) 2H-stacking, where the individual layers are vertically mirrored and slightly shifted with respect to one another, and (b) 3R-stacking, where the layers are only laterally shifted from each other. For an octahedral unit cell, (c) 1T-stacking is commonly observed, where the layers sit directly on top of one another, with no lateral shift. This stacking configuration can also be distorted and form derivative structures, such as the (d) 1T' and (f) T_d configurations. In these two cases, the octahedral unit cell is distorted in a similar manner, but the resulting layers for (e) 1T' and (g) T_d have slightly different geometries.

it can be metallic, semiconducting, semimetallic or even superconducting [28]. We will now continue our exploration of TMDCs with the two materials used in this thesis, MoS_2 and $MoTe_2$.

2.3.2 MoS_2

MoS_2 is a TMDC consisting of a layer of molybdenum atoms 'sandwiched' between two layers of sulphur atoms. It can occur naturally in both 2H and 3R [35], with the trigonal prismatic phase and therefore 2H-stacking more commonly observed than the rarer octahedral phase, which seems to need specific conditions to grow [39]. The growth process can also be influenced to produce mixed stacking order [40]. In this section, we will focus on the 2H-stacked MoS_2 (as sketched in Fig. 2.6a) which is used in the measurements for this thesis.

In a 2H configuration, bulk MoS_2 is a semiconductor with an indirect bandgap of 1.23 eV [41]. If it is thinned down to a monolayer, it changes character and becomes a direct bandgap semiconductor with a gap of 1.9 eV [42], as first observed by Splendiani et al. in 2010 by the emergence of photoluminescence in monolayer MoS_2 [43]. This is illustrated in Fig. 2.7, where the changes in band structure have been calculated using DFT [43]. It can be seen that the main changes do not occur at the K point, where the resulting direct bandgap lies, but at the indirect bandgap which increases with decreasing number of layers, until it is finally bigger than the direct gap at K.

This stems from the different orbitals that form the band structure at the different symmetry points in the Brillouin zone: The K point mostly consists of strongly localised d-orbitals at the Mo atoms, which due to their being in the middle of the TMDC 'sandwich' have minimal interlayer coupling [43]. They are therefore barely influenced by changing layer thickness. Near the Γ point and the point between Γ and K involved in the formation of the indirect bandgap, the situation is different: These states consist mostly of the linear combination of d-orbitals of Mo and antibonding p_z-orbitals of S [43]. They therefore have strong interlayer coupling and are influenced directly by a changing number of layers.

But a monolayer of a 2D-material does not (easily) exist in vacuum, it has to be supported by a bulk material underneath, especially if it is to be measured by scanning probe techniques. In our case, the support material is a Au(111) crystal, upon which the (sub-)monolayer of MoS_2 is grown (details about the preparation can be found in chapter 3.2.2).

When a monolayer of MoS_2 is grown on top of Au(111), another topographic effect comes into play: a characteristic moiré pattern emerges (see Fig. 2.8). This moiré pattern with a periodicity of about 3.3 nm [44, 45] stems from the lattice mismatch between the MoS_2 and the underlying Au(111): MoS_2 has a lattice constant of 3.15 Å [46] and Au(111) one of 2.88 Å [46]. The S atoms of MoS_2 can either be in a top-site with respect to the Au atoms (i. e. S directly on top of Au), or in a hollow-site (i. e. S in-between Au). The latter is also divided in an fcc (Mo atoms also in-between Au) and an hcp (Mo on top of Au) configuration [44]. While there is also a slight difference between the hollow-sites (see Ref. [44] for more details), generally the top-sites have a higher apparent height in STM topography ('domes') while the hollow-sites appear more recessed ('valleys').

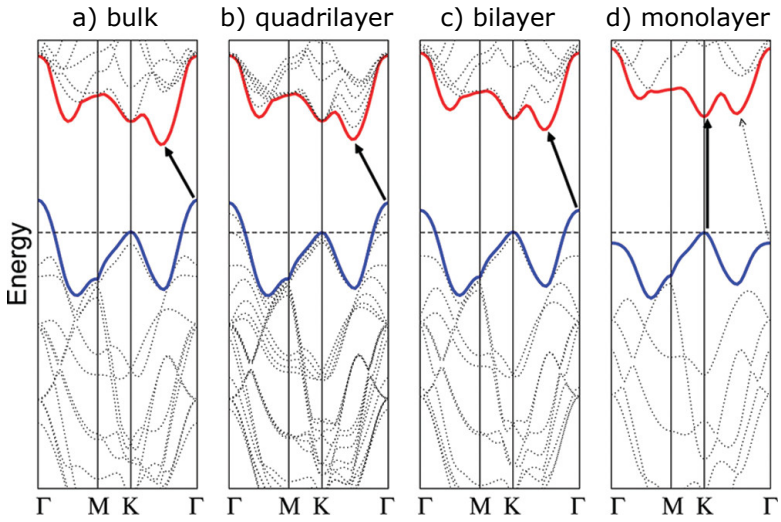

Figure 2.7: Calculated band structure of freestanding MoS_2 with decreasing number of layers. a) Bulk MoS_2 with an indirect bandgap, b) quadrilayer MoS_2 with still an indirect bandgap, c) bilayer MoS_2 with an increasing indirect bandgap, d) monolayer MoS_2 with a direct bandgap. It can be seen that the band structure at the K point barely changes while the Γ point and the terminating point of the indirect bandgap are changed severely by the decreasing number of layers. (Figure taken and adapted from [43]. Reprinted (adapted) with permission from A. Splendiani, L. Sun et al. 'Emerging Photoluminescence in Monolayer MoS_2'. In: *Nano Letters* 10.4 (2010), pp. 1271–1275. DOI: 10.1021/nl903868w. Copyright 2010 American Chemical Society.)

This is confirmed as a topographic effect by AFM measurements [44]. Additionally, both materials 'rumple' slightly to accommodate each other, meaning that the bottom S layer of MoS_2 and the top layer of Au are slightly distorted from the pristine lattice structures [47].

The aforementioned moiré structure also has an influence on the electronic states of MoS_2/Au(111): depending on the positioning at either a dome or valley, the electronic signature is slightly shifted. This can be utilised for e. g. the tuning of electronic properties [45].

The close proximity to a metal and therefore its electron bath naturally also influences the electronic states of MoS_2. There have been multiple attempts to calculate the band structure of MoS_2 on Au(111) which is a non-trivial problem because of the aforementioned moiré structure: the unit cell needed for an accurate calculation simply becomes very big.

Bruix et al. have calculated in Ref. [48] how the bandstructure of MoS_2 changes when put into contact with Au, and a strong hybridisation is the result. As shown in Fig. 2.9a, the hybridisation with the Au leads to a complex band structure, with the semiconducting nature of MoS_2 compromised. Fig. 2.9b shows the projected DoS calculated by Tumino et al. in Ref. [47], and while the semiconducting gap is still clearly visible, there are now states accessible within it.

This is in accordance with $\mathrm{d}I/\mathrm{d}V$ spectra measured by STS: Fig. 2.10 shows such a spectrum recorded on MoS_2/Au(111) in red and a reference spectrum on Au(111)

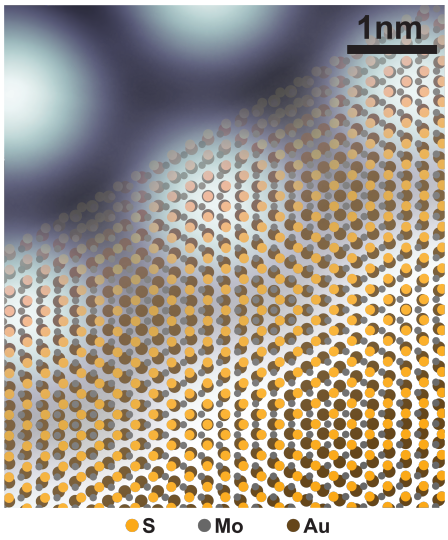

Figure 2.8: STM topography of the moiré pattern of MoS_2/Au(111) visible as a regular pattern of 'domes' and 'valleys', overlayed with a schematic representation of the MoS_2 (yellow and grey) and Au (brown) lattices. On the moiré domes, the S atoms are directly on top of the Au atoms (top-site), while they are in-between the Au atoms in the moiré valleys (hollow-sites). (Figure taken and adapted from [44]. Reprinted from *Surface Science* 678, N. Krane, C. Lotze and K. J. Franke, 'Moiré structure of MoS_2 on Au(111): Local structural and electronic properties', pp. 136–142, Copyright (2018), with permission from Elsevier.)

in gold. MoS_2 shows a shoulder at $-2\,\mathrm{V}$ and a double peak structure at $0.9\,\mathrm{V}$ and $1.4\,\mathrm{V}$. The differential conductance drops almost to zero in-between these peaks, but tunnelling is still possible. The valence band maximum (VBM) and the conduction band minimum (CBM) are also marked, at $-1.4\,\mathrm{V}$ and $0.5\,\mathrm{V}$, respectively. These are noticeably not at the observed peak structures. This stems from the fact that the CBM and VBM are at the K point (as shown before in Fig. 2.7d) and STS measurements are not very sensitive to states at the K point, as they have a large $\boldsymbol{k}_\parallel$ component (see also Chapter 2.1, Eqs. 2.11 and 2.12).

To circumvent the insensitivity of STS to $\boldsymbol{k}_\parallel$, a special technique is employed where the tip height is oscillated using a lock-in amplifier to measure the resulting $\mathrm{d}I/\mathrm{d}z$ signal which in turn is proportional to the decay constant κ [44, 49]. While this allows for identification of the states' origin in the Brillouin zone and gives access to more states with high $\boldsymbol{k}_\parallel$, it has to be kept in mind that the measured signal is still convoluted with the states with low $\boldsymbol{k}_\parallel$, thereby making observation difficult in case of dominating states at Γ. In Ref. [44], this technique was employed by Krane et al. to identify the origin of the peaks visible in Fig. 2.10. Utilising the κ-values, it was determined that the two peaks at $0.9\,\mathrm{V}$ and $1.4\,\mathrm{V}$ originate from the Γ point, and the shoulder at $-2\,\mathrm{V}$ is localised mostly at the Q point, while the CBM lies at the expected energy of $0.5\,\mathrm{V}$. Only the VBM could not be accessed experimentally, most likely due to the strong influence of Au states at the Γ point that dominate this energy region [44].

All in all, this shows that MoS_2 on Au(111) retains enough of its semiconducting properties to still act as a decoupling layer, while at the same time being hybridised

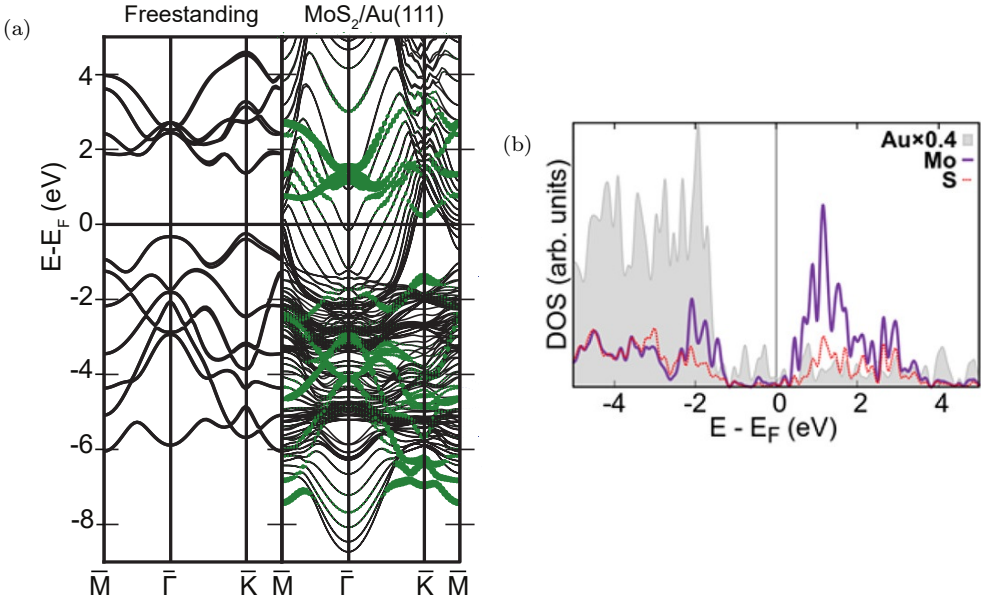

Figure 2.9: (a) Calculated band structure of MoS_2 on Au(111) (right), compared to the bandstructure of freestanding MoS_2 (left). The hybridisation of the states of both materials can be seen by the convoluted structures, and the semiconducting nature of freestanding MoS_2 is compromised by the metal bands from the Au. The green markers represent the states stemming from the MoS_2 orbitals [48]. (Figure taken from [48]. Reprinted figure with permission from A. Bruix, J. A. Miwa, et al., *Phys. Rev. B* 93, 165422, 2016. Copyright (2016) by the American Physical Society.) (b) Projected density of states (PDoS) for MoS_2/Au(111), separated into the individual components of Au (grey), Mo (purple) and S (orange). The Au states populate the bandgap of MoS_2. (Figure taken from [47].)

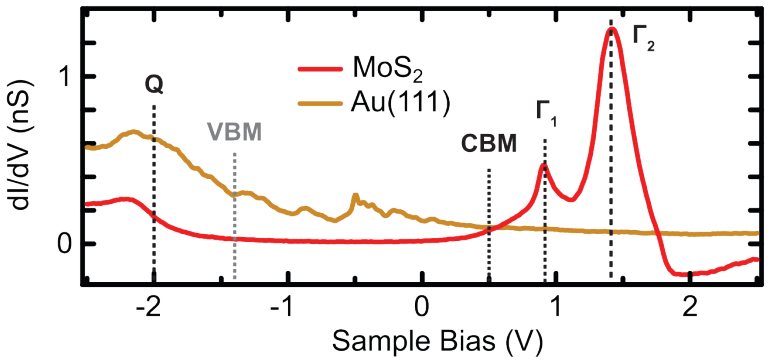

Figure 2.10: dI/dV spectrum of MoS_2/Au(111) (red) with a reference spectrum on Au(111) (gold). The MoS_2 spectrum shows a double peak structure at 0.9 V and 1.4 V, and a shoulder at −2 V, all marked with a dashed line. The origin of these states was determined using a measurement technique sensitive to the decay constant κ [44] and determined to be the result of tunnelling into bands at the Γ point for 0.9 V and 1.4 V, and into bands at the Q point for −2 V. The energies of the valence band maximum (VBM) and conductance band minimum (CBM) at −1.4 V and 0.5 V are marked by dashed lines. (Figure taken and adapted from [44]. Reprinted from *Surface Science* 678, N. Krane, C. Lotze and K. J. Franke, 'Moiré structure of MoS_2 on Au(111): Local structural and electronic properties', pp. 136–142, Copyright (2018), with permission from Elsevier.)

enough to not prove problematic for STM. The effect of the decoupling layer on e. g. molecular adsorbates will be explored in more detail in sections 2.4 and 2.5.

To sidestep the hybridisation with Au and to explore 'freestanding' MoS_2 in more detail, efforts have been made to grow MoS_2 on other substrates, such as HOPG [50, 51] and Al_2O_3 (sapphire) [52, 53], to name two examples[4)]. It has, however, proven to need specific growth conditions to succeed [54].

No (real) material is perfect, there are always intrinsic defects present. For MoS_2, there are three commonly observed ones: S vacancies in both the top and bottom S layer, and missing patches of Au underneath an MoS_2 island (so-called 'pits'). These pit-area defects are of interest, because they approximate a freestanding layer of MoS_2: As investigated by Krane et al. in Ref. [55], this pit shows a much sharper bandgap in the $\mathrm{d}I/\mathrm{d}V$ spectrum with conductance dropping to basically zero, showing that the hybridisation with the Au is greatly reduced by the missing layer.

The single S vacancies in MoS_2 also show interesting properties that are of particular interest to the measurements shown in this thesis. They appear as dark centres with a surrounding triangular rim of two different orientations and slight differences in appearance. As revealed by AFM measurements [56], these are S vacancies in the top and bottom layer of the MoS_2 'sandwich'. These also show intriguing electronic properties: When measured using STS, they show a resonance close to E_F that has been attributed to a Kondo resonance [56]. Measurements of the local contact potential difference (LCPD) reveal that this stems from the localisation of a negative charge at these defect sites through charge transfer from the Au underneath [56], which is consistent with DFT calculations [57]. We will utilise these defects to anchor thiol-based molecules in chapter 4.

2.3.3 $MoTe_2$

$MoTe_2$ is another member of the family of TMDCs. Quite similarly to MoS_2, it consists of a Mo layer sandwiched between two layers of Te. Unlike MoS_2, $MoTe_2$ does not occur naturally and has to be grown under laboratory conditions. Depending on the growth method, it can form in 2H, 1T' and T_d structures [58–61] (see Figs. 2.6a, 2.6d and 2.6f), with phase-transitions possible between the different structures [28, 62, 63], which can be utilised in strain engineering [20, 64]. The stacking sequence influences the properties of $MoTe_2$ quite significantly: Depending on the structure, $MoTe_2$ is reported to be a semiconductor [35], a Weyl-semimetal [35, 65, 66], or even a superconductor under specific conditions [67, 68] and can show a charge density wave [69, 70]. Here, we will focus on the semiconducting 2H-stacked $MoTe_2$.

The calculated bandstructure of bulk 2H-$MoTe_2$ can be seen in Fig. 2.11. In its bulk form, 2H-$MoTe_2$ has an indirect bandgap of 1.0 eV [71, 72] between the K point and a point between K and Γ [73, 74], which makes it one of the smallest reported bandgap of TMDCs. This is of special interest because of its similarity to the bandgap of silicon with 1.1 eV [75, 76], opening up the possibilities of integration in silicon-based circuits, such as for optoelectronic applications [77]. Relevant for STS is, again, the band structure

[4)] MoS_2 on these substrates was also briefly investigated by the author.

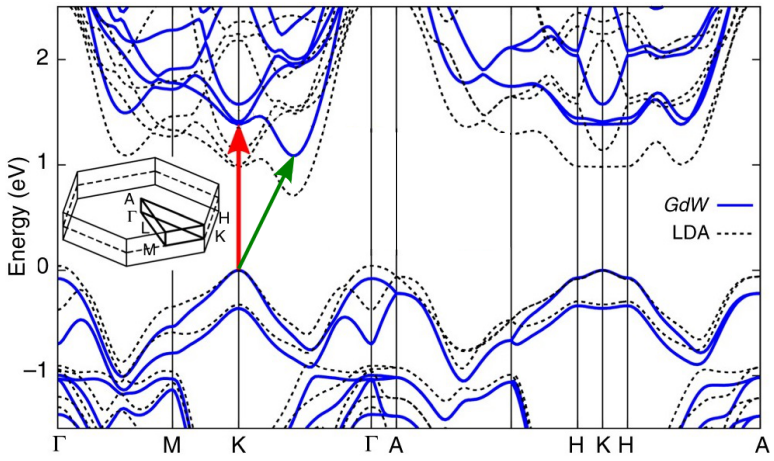

Figure 2.11: Calculated bandstructure of bulk 2H-$MoTe_2$. The indirect bandgap is marked with the green arrow and has a width of 1.0 eV. The red arrow shows the direct bandgap. The bandgap at the Γ point exceeds 2 eV. (Figure taken and adapted from [73].)

at the Γ point. As visible in Fig. 2.11, the conductance and valence bands are furthest apart in energy at Γ and A, making the bandgap at these points wider than 2 eV. This will be observed in the STS measurements on $MoTe_2$ in Ch. 6 as well.

When thinned to a monolayer, 2H-$MoTe_2$ becomes a direct bandgap semiconductor with a bandgap of 1.1 eV [78]. In contrast to MoS_2 and other TMDCs, there is evidence that the crossing from an indirect to a direct bandgap already occurs before monolayer thinness is reached [79].

As for all grown substrates, point defects are intrinsic to $MoTe_2$ as well. While literature already reports multiple different defect types, such as Te-vacancies [80, 81], Mo-vacancies [82] and chalcogen antisites [82, 83] (i. e. a Mo atom replacing a Te atom), there are only circumstantial identifications and correlations to the appearance of these defects in STM/STS. Interestingly, Ref. [80] and [81] seem to contradict each other with their identification of the Te-vacancies.

A particularly interesting observation has been made by Z. Guguchia et al. in Ref. [82] and P. M. Coelho in Refs. [81, 83] that the chalcogen antisites can ferromagnetically dope the host material, and allow for the creation of long-range magnetic order via these intrinsic defects [82]. Coelho et al. have additionally shown that these interstitials are mobile and can diffuse at ~ 200 K. They utilise this property to create mirror twin boundaries in the surface of $MoTe_2$. Their measurements and DFT calculations also show that for $MoTe_2$, in contrast to e. g. MoS_2, when evaporating additional metal atoms such as Mo, V or Ti onto the $MoTe_2$ substrate, adatom/cluster formation is *dis*favoured and incorporation into the $MoTe_2$ layer as interstitials much more likely. They claim that it is the Te-vacancies that are now being filled with transition metal adatoms and that charge transfer between Te-vacancies and neighbouring V-interstitials is possible as well [81].

In Ch. 6, we will investigate bulk 2H-$MoTe_2$, where we will take a closer look at these defects and the behaviour of adsorbed molecules.

2.4 Molecular Adsorbates

To measure molecules with a scanning probe technique, they have to be adsorbed on a surface. In the case of STM, it additionally has to be a conducting surface. This leads to different possible interactions between the molecule and the substrate that have to be taken into account.

When a molecule attaches itself to a surface (adsorption), its properties are changed when compared to a gas-phase molecule. There are geometric changes (usually the molecular structure is 'flattened' because of the interaction with the surface [84]) and the electronic structure is affected as well. The severity of the changes depends on how exactly a molecule is adsorbed. Generally speaking, a molecule can be either physisorbed or chemisorbed. These terms describe the strength of the interaction between the adsorbed molecule and the surface it is placed upon. A physisorbed molecule interacts weakly with the surface, bound only through van-der-Waals forces. They usually require a low temperature to inhibit their molecular diffusion and their electronic properties are not severely influenced by the characteristics of the surface. Chemisorbed molecules, on the other hand, form a strong localised chemical bond with the surface they are placed on. This also means that the electronic structure of the molecule (and – locally – the surface) is quite significantly changed when compared to a molecule in gas phase (i. e. 'free').

When the electronic states of a (hypothetical) gas-phase molecule were to be probed by STS, we would see the frontier orbitals (HOMO: highest occupied molecular orbital and LUMO: lowest unoccupied molecular orbital) not at their intrinsic energy, but shifted in energy by the Coulomb repulsion E_C[5)]. This stems from the fact that in STS, as the name implies, single electrons are tunnelled at a specified energy (see chapter 2.1). We would therefore not measure the HOMO and the LUMO, but rather the electron affinity (EA) ('How easy is it to put an additional electron in?') and the ionisation potential (IP) ('How hard is it to remove an electron?').

When placed on a metal surface (i. e. Au), the Coulomb repulsion is reduced through the formation of image charges in the electron bath of the metal. For the states measured in STS this means that they shift closer in energy to the position of the 'bare' HOMO and LUMO. Additionally, the lifetime of the charged state is greatly reduced because the charge is easily transmitted to the metal. Due to the Heisenberg uncertainty principle, this leads to a state broadened in energy. These effects are schematically depicted in Fig. 2.12.

This energy broadening on a metal substrate is counteracted by utilising a decoupling layer (such as MoS_2 as introduced in section 2.3.2), which gives both a physical distance from the metal and an energetical separation because of e. g. a semiconducting bandgap. The energy resolution of molecular states is thereby greatly increased and allows e. g. for the resolution of vibronic states [85].

While the effects described in this section are generally present for any molecular adsorbate, there are many more possible interactions with the surface depending on the specifics of the system used. Some examples are charge transfer between the molecule and

[5)] In this hypothetical scenario we neglect the fact that the tunnelling process would quickly come to a standstill because of a Coulomb blockade.

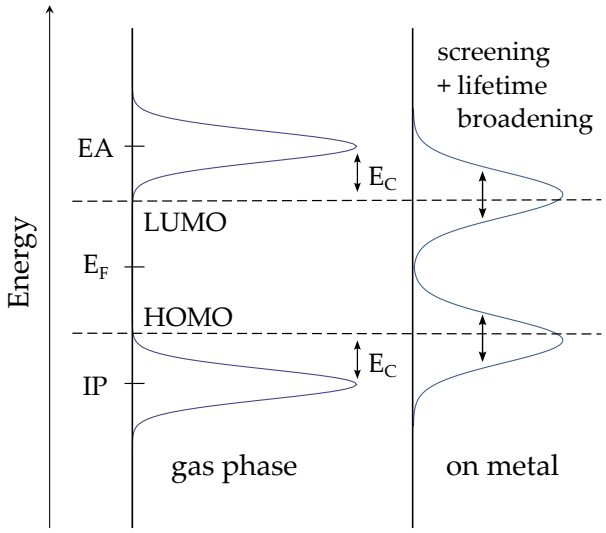

Figure 2.12: Schematic representation of molecular states being probed by STS. For a gas-phase molecule, not the frontier orbitals (HOMO and LUMO) are probed by a tunnelling electron, but rather the electron affinity (EA) and the ionisation potential (IP), because the Coulomb repulsion E_C has to be overcome additionally. When the molecule is placed on a metal, E_C is reduced by the screening through the electron bath of the metal. Additionally, the lifetime of the state is shorter, which in turn leads to a broadening of the state in energy.

the surface [86, 87], which can lead to energy level alignment [88], formation of surface dipoles [87, 89, 90], just to name a few. Chapter 4 of this thesis shows a chemisorbed molecule and the changes that stem from this interaction.

2.5 Double Barrier Junctions & Tip-Perturbation Potential

In the case of a decoupling layer on top of a metal substrate (as is the case for MoS_2 on Au(111)), the picture of only one tunnelling junction as shown in Chapter 2.1 is not sufficient anymore. A second tunnelling barrier between decoupling layer and metal comes into play, additionally to the vacuum barrier: we have a 'double barrier junction'. This situation is sketched in Fig. 2.13a for no bias voltage applied, where the Fermi levels E_F of tip and sample align with the chemical potential μ_{mol} of the molecule. A bias voltage V_B applied between tip and sample is distributed over the two barriers:

$$V_B = V_{vac} + V_{DL} \ , \tag{2.26}$$

with V_{vac} being the voltage dropping over the vacuum barrier and V_{DL} the voltage dropping across the decoupling layer. In almost all cases, the vacuum barrier is still dominating, and the voltage drop over the decoupling layer therefore small. This voltage drop becomes relevant when dealing with molecular adsorbates on the decoupling layer, since the additional voltage means that the molecular states are not pinned to the Fermi level of the substrate anymore, i. e. the relative alignment between Fermi energy of the metal substrate and the chemical potential of the molecule can change, as shown in Fig. 2.13b.

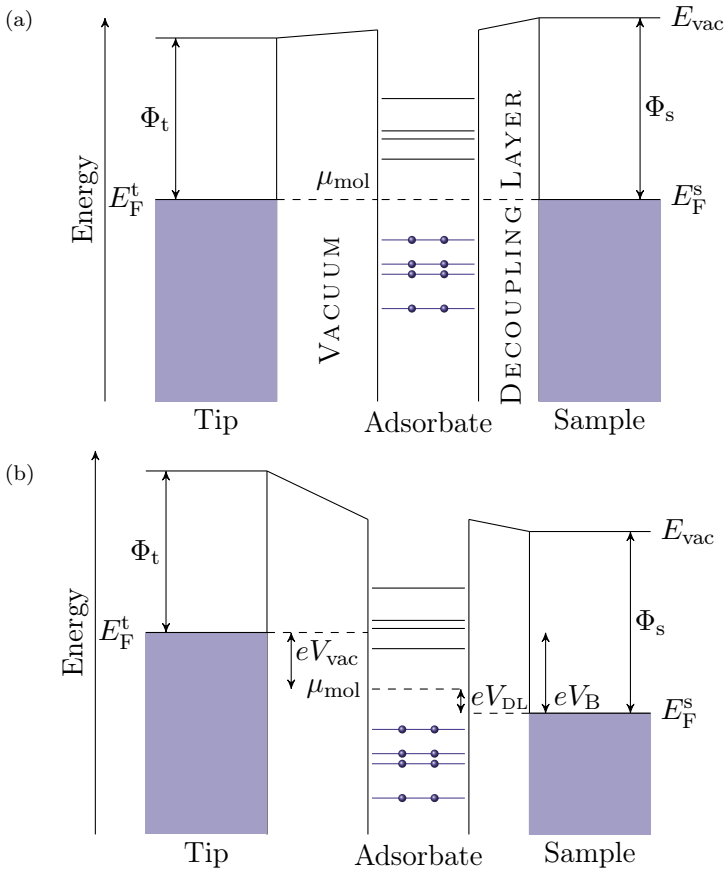

Figure 2.13: Schematic depiction of a double barrier junction with a vacuum barrier between tip and adsorbate, and a decoupling layer between adsorbate and sample. (a) No external bias voltage is applied, so Fermi energies E_{F} of tip and sample are aligned with each other and the chemical potential μ_{mol} of the adsorbate. (b) Double barrier junction with applied bias voltage V_{B}. The bias voltage drops over both the vacuum barrier and the decoupling layer, thereby shifting the relative alignment between μ_{mol} and $E_{\mathrm{F}}^{\mathrm{s}}$. The distribution between V_{vac} and V_{DL} depends on the properties of the system, and the width of the vacuum barrier is influenced by the tip-sample distance.

This also means that the distance between tip and sample changes the amount of voltage dropping over the second junction, as the width of the vacuum tunnelling barrier is changed by the tip position. Going further away with the tip means that the vacuum barrier increases, and therefore the percentage of voltage dropping over the decoupling layer decreases, leading in turn to an apparent shift of states towards E_F, and vice versa for approaching with the tip.

Here it is not only the vertical distance to the tip, but also the lateral distance of the tip to the adsorbate to be probed that influences the relative energy level alignment. As detailed by Nils Krane et. al. in Ref. [91], the electric field surrounding the tip is laterally not homogeneous, thereby influencing the voltage drop.

To understand this in more detail, we will follow the derivation in Ref. [91]. If we consider the case of a V_B chosen such that we tunnel from the tip into a molecular state at energy $E_0 = eV_0$, this means that $V_\mathrm{vac} = V_0$, i. e. the E_F of the tip is aligned with the molecular state. The voltage dropping over the decoupling layer can also be expressed as a percentage of V_B, so

$$V_\mathrm{DL} = \alpha V_\mathrm{B} \ , \tag{2.27}$$

where $0 \leq \alpha \leq 1$ is the system dependent factor that reduces the bias voltage applied to the adsorbate.

Now, to understand the interaction between tip, sample and adsorbate in a double barrier junction, understanding the factor α is crucial. We can approach it by considering the electric potential $\phi_B(\boldsymbol{r})$ of the tip. Since our tunnelling junction is not a simple plate capacitor, as is often pretended in schematic drawings such as Fig. 2.13 for simplicity, $\phi_B(\boldsymbol{r})$ is highly inhomogeneous, both laterally and vertically. It can be described as [91]:

$$\phi_B(\boldsymbol{r}) = \varphi(\boldsymbol{r}) V_\mathrm{B} \ , \tag{2.28}$$

with $\varphi(\boldsymbol{r})$ being the unitless shape of the potential. By considering the boundary conditions of our tunnelling junction, we see that $\phi_B(\mathrm{tip}) = 0$ (tip is grounded) and $\phi(\mathrm{sample}) = V_\mathrm{B}$ (sample is biased) [91]. We can therefore express the voltage dropping across the vacuum barrier V_vac with the tip at position $\boldsymbol{r}_a$ as

$$V_\mathrm{vac} = \varphi(\boldsymbol{r}_a) V_\mathrm{B} \ , \tag{2.29}$$

assuming no contact potential difference (CPD) [91]. Using Eqs. (2.26) and (2.27), the voltage dropping across the decoupling layer V_DL can be expressed as:

$$V_\mathrm{DL} = \alpha(\boldsymbol{r}_a) V_\mathrm{B} = V_\mathrm{B} - V_\mathrm{vac} = V_\mathrm{B} \left(1 - \varphi(\boldsymbol{r}_a)\right) \ . \tag{2.30}$$

To evaluate $\varphi(\boldsymbol{r}_a)$ further, Krane et. al. approximate the tip as a point charge q with its corresponding mirror charge of $-q$ separated by twice the tip height z_t and twice the radius of the spherical tip R [91]. After considering the boundary conditions, they reach the following for the potential shape $\varphi(x, z)$ [91]:

$$\varphi(x,z) = 1 - \left(\frac{R^2}{2z_\mathrm{t}} + R\right) \left[\frac{1}{\sqrt{x^2 + (z - R - z_\mathrm{t})^2}} - \frac{1}{\sqrt{x^2 + (z + R + z_\mathrm{t})^2}}\right] \ . \tag{2.31}$$

The resulting model shows that $\varphi(x, z)$ is minimal when the lateral distance between tip and adsorbate is minimal (tip placed right above molecule). Considering Eq. (2.30), this means that V_{DL} becomes maximal in this case (naturally assuming the same vertical distance). As a consequence, a higher V_{B} of [91, 92]

$$V^* = \frac{E_0}{e\varphi(x, z)} \tag{2.32}$$

is needed to access the same molecular state at E_0, leading to an apparent shift to higher energy in the $\mathrm{d}I/\mathrm{d}V$ spectra. We will observe this effect in Ch. 5 for VONc molecules on MoS_2/Au(111).

2.6 Vibronics and Vibration-Assisted Tunnelling (VAT)

When we consider tunnelling into molecules, we also have to take into account that the molecule is transiently charged by the tunnelling electron/hole. When the molecule is placed on a metal, the lifetime of such a charged state is usually too short to induce changes in the molecule itself. When we, however, place our molecule on a decoupling layer such as MoS_2, the lifetime of such an excited state is greatly prolonged due to the decoupling from the metal's electron bath. We therefore have to consider the changes induced in the molecule by the additional charge.

Depending on the sign of the applied bias voltage, an electron is either added or removed from the molecule, and therefore changes the molecule's charge distribution. This in turn causes a deformation of the molecule as it tries to accommodate the additional charge/hole. In a more formal way, this can be understood as the excitation of vibrational modes caused by an electronic excitation. This coupling of vibrations and electronic excitation is called vibronics.

This can be understood within the well-known Franck-Condon principle [93, 94]: The electronic transition is quasi-instantaneous, so that the positions of the nuclei do not change, and only adjust to the excited state afterwards. We can therefore consider both processes separately.

Fig. 2.14 shows an energy diagram, depicting the ground state M^0 and the excited state M^1, simplified as parabolas. Here we consider the injection of an electron without loss of generality. Both parabolas are offset from each other not only in energy, but also in normal coordinates, since the molecule deforms upon excitation.

By injecting an electron with our STM tip, we excite a transition from the vibrational ground state of M^0 (the so-called fundamental progression [96]), into M^1. In a semi-classical picture, we consider our nuclei to be static during this electronic excitation, and we consequently have a so-called vertical transition, illustrated by the green arrow in Fig. 2.14. We therefore reach a vibrationally excited state within M^1, where the green arrow intersects with the M^1 parabola.

In a quantum-mechanical point of view, the overlap of the wave function of the ground state ψ_{g} with the individual vibrational states $\psi_{\mathrm{k,n}}$ of the excited state have to be considered. The transition rate Γ between a (ground) state ψ and an excited state ψ' is,

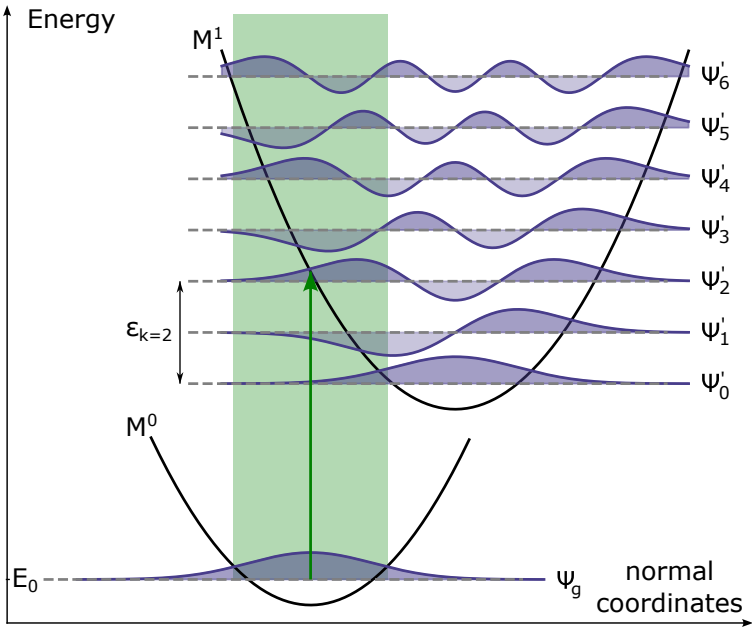

Figure 2.14: Schematic depiction of a vibrational excitation from the vibrational ground state of the neutral state M^0 to the vibrational modes of the excited state M^1. The green arrow depicts the vertical Franck-Condon transition, and the green shaded area represents the wavefunction overlap between the ground state ψ_g and the vibrational states which have to be considered when determining the transition probability. Wavefunctions of vibronic modes created using code from [95].

according to Fermi's golden rule:

$$\Gamma = \frac{2\pi}{\hbar} \left|\left\langle \psi' \right| H' \left| \psi \right\rangle\right|^2 \delta(E' - E) \ , \tag{2.33}$$

where H' is the perturbation which in this case is the electric dipole moment (operator) $\boldsymbol{\mu}$. According to the Born-Oppenheimer approximation, the wavefunctions can be split into an electron component ψ_e and a nuclear component [96] which in the context of vibronics means a vibrational component ψ_ν [97][6]:

$$\psi = \psi_\mathrm{e}\psi_\nu \ . \tag{2.34}$$

Assuming that the perturbation can also be separated in this manner into parts acting on both components separately, which is a reasonable approximation when considering electric dipole moments [96], then:

$$H' = \boldsymbol{\mu} = \mu_\mathrm{e} + \mu_\nu \ , \tag{2.35}$$

[6] Since the molecules in question are adsorbed on a surface in STM, we neglect rotational components.

our transition moment becomes:

$$\langle \psi' \,|\, H' \,|\, \psi \rangle = \langle \psi' \,|\, \boldsymbol{\mu} \,|\, \psi \rangle \tag{2.36}$$

$$= \langle \psi'_\mathrm{e} \psi'_\nu \,|\, \mu_\mathrm{e} + \mu_\nu \,|\, \psi_\mathrm{e} \psi_\nu \rangle \ . \tag{2.37}$$

If we further assume that the operators only act on operands of their own sphere, this becomes:

$$\langle \psi' \,|\, \boldsymbol{\mu} \,|\, \psi \rangle = \langle \psi'_\mathrm{e} \,|\, \mu_\mathrm{e} \,|\, \psi_\mathrm{e} \rangle \langle \psi'_\nu \psi_\nu \rangle + \langle \psi'_\mathrm{e} \,|\, \psi_\mathrm{e} \rangle \langle \psi'_\nu \,|\, \mu_\nu \,|\, \psi_\nu \rangle \ . \tag{2.38}$$

The last term becomes zero, as ψ'_e and ψ_e are orthogonal to each other and therefore $\langle \psi'_\mathrm{e} \,|\, \psi_\mathrm{e} \rangle = 0$. Inserting this into Eq. (2.33) yields:

$$\Gamma = \frac{2\pi}{\hbar} \underbrace{\left| \langle \psi'_\mathrm{e} \,|\, \mu_\mathrm{e} \,|\, \psi_\mathrm{e} \rangle \right|^2}_{\substack{\text{tunnelling} \\ \text{matrix element}}} \underbrace{\left| \langle \psi'_\nu \,|\, \psi_\nu \rangle \right|^2}_{\substack{\text{Franck-Condon} \\ \text{factor}}} \delta(E' - E) \ . \tag{2.39}$$

The first part is the probability of an electronic excitation which in STM is of course nothing else than the tunnelling matrix element, as discussed in detail in Ch. 2.1. The second part is the so-called Franck-Condon factor that governs the transition between vibrational states. It can clearly be seen that vibrational states with a larger overlap have a larger transition rate.

To return to the diagram of Fig. 2.14, this means that not only the vertical transition is possible, but also the excitation of the other vibrational states along the green arrow in the figure, schematically depicted as the green shaded area. This leads to a progression of transitions [96], i. e. multiple satellite peaks that stem from vibronic excitations.

This can be observed in STM with $\mathrm{d}I/\mathrm{d}V$ spectra: If the energy resolution is high enough to resolve individual peaks, we first observe an elastic peak, i. e. the tunnelling into a molecular state, e. g. the LUMO of a molecule. This corresponds to the ground state M^0 at energy E_0[7)].

Now we increase our bias voltage and reach an energy where the tunnelling path into the higher vibrational modes opens up: we record the vibronic satellite peaks. When recording such a vibronic spectrum, it quickly becomes apparent that not all modes appear with the same intensity.

The intensity of the transition between each excited vibrational state $\psi_{\mathrm{k,n}}$ and the ground state ψ_g is governed by a Poisson distribution [85, 100]:

$$|\langle \psi_{\mathrm{k,n}} \,|\, \psi_\mathrm{g} \rangle|^2 = e^{-S_\mathrm{k}} \frac{S_\mathrm{k}^n}{n!} \ , \tag{2.40}$$

[7)] This already excites the molecule into M^1, but this process cannot be observed with conventional STM. Light-emission STM is a technique that allows for the probing of the excited states. For more information, see for example [98, 99].

where S_k is the so-called Huang-Rhys factor [101] which is the relation between the relaxation energy ε_k and the energy of the vibrational mode $\hbar\omega_\mathrm{k}$ [85]:

$$S_\mathrm{k} = \frac{\varepsilon_\mathrm{k}}{\hbar\omega_\mathrm{k}} \ . \tag{2.41}$$

The relaxation energy ε_k is the energy difference between a higher vibrational mode and its ground vibrational state. The total relaxation energy of a molecule ε_rel is the sum over these individual energies:

$$\varepsilon_\mathrm{rel} = \sum_\mathrm{k} \varepsilon_\mathrm{k} = \sum_\mathrm{k} S_\mathrm{k}\hbar\omega_\mathrm{k} \ . \tag{2.42}$$

The Huang-Rhys factor can be seen as the indicating entity for the electron-phonon coupling of certain modes and therefore how strong the resonance we record in the $\mathrm{d}I/\mathrm{d}V$ spectrum is.

To complicate matters further, not only the fundamental vibrational modes of a molecule can be excited, but also the combination of modes [85, 97]. All these effects put together create the peak structure we record in $\mathrm{d}I/\mathrm{d}V$ spectroscopy.

But this is still not the complete picture. We now also have to take the geometry of the probed molecule into account, and thereby the spatial extend of its MOs.

When a molecule vibrates in one of its vibrational modes, it deforms physically, i. e. the individual atoms are displaced from their normal position. These displacements can be in all spatial dimensions. If we now consider a vibrational mode with its main displacement perpendicular to the surface (up and down when looking at a molecule from the side), the vibration can break the symmetry of the nodal planes of an MO. This is schematically illustrated in Fig. 2.15.

Why is this relevant to tunnelling? Let us remind ourselves that tunnelling in an STM junction is governed mainly by the overlap of the wave function of the tip and of those on the surface. If we now consider the usual case of an *s*-wave tip and the tunnelling into a highly modulated MO as sketched in Fig. 2.15, for the static molecule the wavefunction overlap is greatly reduced in the middle of the molecule because of the nodal planes; the different phases cancel each other out. This leads to a decrease in tunnelling probability and therefore in current which in turn leads to much lower peak intensities in the $\mathrm{d}I/\mathrm{d}V$ spectra in the middle of the molecule when compared to the edges.

If we now consider our vibrational mode, the vibration changes the distribution of the phases as explained above. For our *s*-wave tip this means that there is less cancellation of phases and that the overlap is therefore much greater, leading to an enhanced peak in the $\mathrm{d}I/\mathrm{d}V$. This is called vibration-assisted tunnelling (VAT) [102, 103].

From an energetical point of view, these transitions occur at $E_\mathrm{bias} > E_\mathrm{MO} + \hbar\omega$ [103], which means that part of the energy of the tunnelling particle is used for the vibrational excitation, after which the 'regular' Franck-Condon vibronic transition occurs (see Fig. 2.16). In the recorded $\mathrm{d}I/\mathrm{d}V$ this means that we see a replica of the vibronic spectrum shifted to higher energies, while the original spectrum is suppressed. This effect will be explored on a model system in Ch. 5.5.

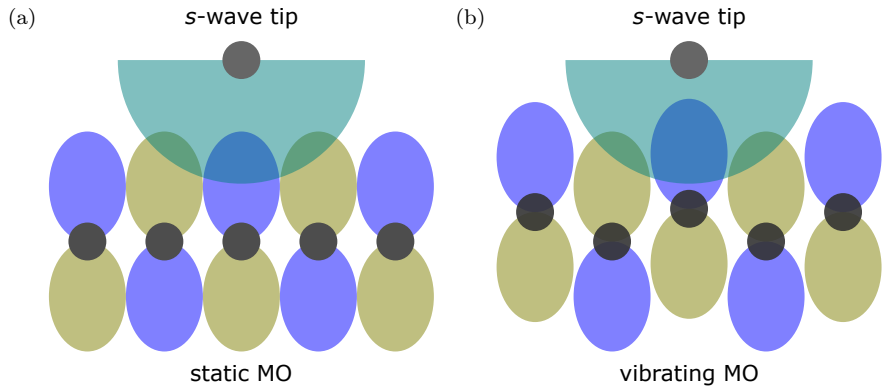

Figure 2.15: Schematic depiction of the molecular orbitals (MOs) of a molecule with many nodal planes (yellow and blue represent the different phases), and an *s*-wave tip wavefunction probing this molecule. The overlap of the wavefunctions is an integral part for the tunnelling probability. (a) The molecule is not vibrating, i. e. static. The overlap between tip and molecule wavefunctions is reduced in the middle of the molecule, as the different phases cancel each other out. The tunnelling current is reduced in comparison to the edges. (b) The molecule is excited into a vibrational mode, with the nuclei being displaced perpendicular to the surface. This leads to an enhanced overlap with the tip wavefunction and therefore a higher tunnelling current.

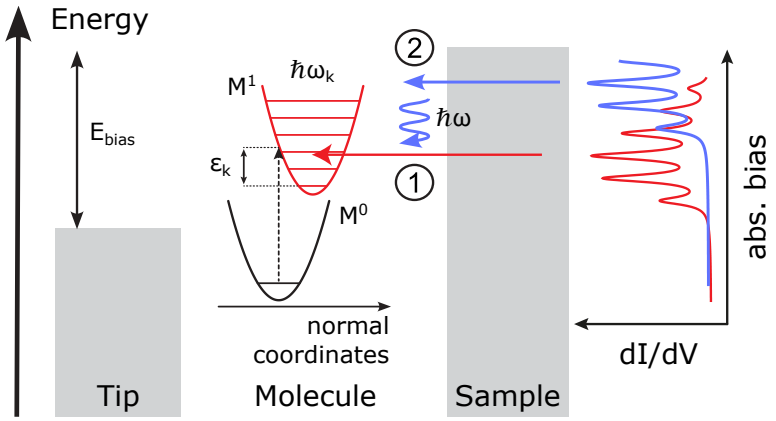

Figure 2.16: Schematic depiction of vibration-assisted tunnelling (VAT) and the Franck-Condon process in an STM junction with a molecule. At bias voltages of $E_{\mathrm{bias}} > E_{\mathrm{MO}}$, the regular Franck-Condon process (red arrow, process 1) occurs, as shown in more detail in Fig. 2.14, resulting in the red $\mathrm{d}I/\mathrm{d}V$ spectrum on the right. At higher energies of $E_{\mathrm{bias}} > E_{\mathrm{MO}} + \hbar\omega$, VAT (blue arrow, process 2) comes into play: the energy of the tunnelling particle is partially used to traverse the vibrational excitations, after which the regular Franck-Condon process follows. This results in a replica of the vibronic spectrum at higher energies (blue $\mathrm{d}I/\mathrm{d}V$ spectrum). (Figure taken and adapted from [103]. Reprinted figure with permission from G. Reecht, N. Krane et al., *Phys. Rev. Lett.* 124, 116804, 2020. Copyright (2020) by the American Physical Society.)

2.7 The Kondo Effect

In this chapter we will give a brief introduction to the Kondo effect while following along with the historical developments. This chapter is mainly based on Refs. [104, 105], and for a more expansive treatment of Kondo physics, the reader is referred to Refs. [104, 106]. The story begins in the 1950s, where J. Friedel et al. observed that magnetic impurities in noble metals have an effect on their resistance [107]. This manifests especially in the by-then well-known behaviour that noble metals exhibit a resistance minimum with temperature [108], meaning that the resistance goes up again with decreasing temperature. This did not fit the model of electrical resistance being essentially caused by scattering of electrons with lattice phonons, which should see a continuous decrease in resistance as the number of phonons decreases with temperature.

In 1961, P. W. Anderson developed the eponymous 'Anderson model' [109] which shows how a localised electron interacts with an electron bath. Since a localised single electron carries a spin of $S = \frac{1}{2}$, it is a singly occupied magnetic impurity. The corresponding doubly occupied state is separated from the singly occupied state by the Coulomb repulsion energy U, as visualised in Fig. 2.17. The singly occupied state has the energy $E_\mathrm{s} = e_\mathrm{d}$, and the doubly occupied state $E_\mathrm{d} = 2e_\mathrm{d} + U$ [104]. For the assumed single localised electron, the ground state of the system is of course singly occupied, which naturally means that e_d is below E_F and $e_\mathrm{d} + U$ is above. Additionally, it is assumed that the broadening of the states Γ caused by hybridisation is less than the separation of the states U. This is called the local moment regime [104][8].

The system now interacts with the electron bath of the metal substrate which is described by the following Hamiltonian [104]:

$$H = \underbrace{\sum_\sigma e_\mathrm{d} n_{\mathrm{d},\sigma}}_{\substack{\text{occupancy of}\\ \text{non-degen. e}^- \text{ states}}} + \underbrace{U_{\mathrm{n_{d,\uparrow}n_{d,\downarrow}}}}_{\substack{\text{Coulomb}\\ \text{interaction}}} + \underbrace{\sum_{\boldsymbol{k},\sigma} e_{\boldsymbol{k}} c^\dagger_{\boldsymbol{k},\sigma} c_{\boldsymbol{k},\sigma}}_{\text{electron bath}} + \underbrace{\sum_{\boldsymbol{k},\sigma} \left(V_{\boldsymbol{k}} c^\dagger_{d,\sigma} c_{\boldsymbol{k},\sigma} + V^*_{\boldsymbol{k}} c^\dagger_{\boldsymbol{k},\sigma} c_{d,\sigma} \right)}_{\text{hybridisation}} , \tag{2.43}$$

with $V_{\boldsymbol{k}}$ being the hybridisation matrix element [104]:

$$V_{\boldsymbol{k}} = \sum_\delta e^{i\boldsymbol{k}\cdot\boldsymbol{d}_\delta} \langle \phi_\mathrm{d} \,|\, H \,|\, \psi_{\mathrm{d}\delta} \rangle \ , \tag{2.44}$$

and ϕ_d the atomic d-level, $\psi_{\mathrm{d}\delta}$ the electron bath states, $c^\dagger_{\boldsymbol{k},\sigma}$ the creation operator for electrons with momentum $\boldsymbol{k}$ and spin σ, $c^\dagger_{d,\sigma}$ the creation operator for electrons in the d-level, $n_{\mathrm{d},\sigma}$ the number operator giving the occupation number.

To better understand the interaction between impurity and electron bath, let us now quickly consider the s-d-model (also called Kondo model) developed by J. Kondo in 1964 [110]. This model is a different approach when compared to Anderson's, and shows that the local impurity with spin S couples to the bath electrons via exchange

[8] Other possible regimes are the intermediate valence regime, the empty orbital regime and the regime of double occupation [104]. Depending on the regime, the interactions change. For more information, see Ref. [104].

interaction J. In 1966, J. R. Schrieffer and P. A. Wolff devised a canonical transformation that shows that the Anderson model is (under certain conditions) equivalent to the s-d-model [111]. After some calculation steps, that can be followed in detail in Ref. [104], the Hamiltonian from Eq. (2.43) can be transformed to [112]:

$$H = \sum_{\boldsymbol{k},\boldsymbol{k'}} J_{\boldsymbol{k}\boldsymbol{k'}} \left(S^+ c^\dagger_{\boldsymbol{k}\downarrow} c_{\boldsymbol{k'}\uparrow} + S^- c^\dagger_{\boldsymbol{k}\uparrow} c_{\boldsymbol{k'}\downarrow} + S_z \left(c^\dagger_{\boldsymbol{k}\uparrow} c_{\boldsymbol{k'}\uparrow} - c^\dagger_{\boldsymbol{k}\downarrow} c_{\boldsymbol{k'}\downarrow} \right) \right) + \sum_{\boldsymbol{k},\boldsymbol{k'}} K_{\boldsymbol{k},\boldsymbol{k'}} c^\dagger_{\boldsymbol{k}\sigma} c_{\boldsymbol{k'}\sigma} \ , \tag{2.45}$$

where S_z and $S^\pm = S_x \pm i S_y$ are the spin operators for the spin S of the d-level, $J_{\boldsymbol{k},\boldsymbol{k'}}$ the effective exchange coupling and $K_{\boldsymbol{k},\boldsymbol{k'}}$ the potential scattering. These can be related back to the Anderson model by [104]:

$$J_{\boldsymbol{k},\boldsymbol{k'}} = V^*_{\boldsymbol{k}} V_{\boldsymbol{k'}} \left(\frac{1}{U + e_\mathrm{d} - e_{\boldsymbol{k'}}} + \frac{1}{e_{\boldsymbol{k}} - e_\mathrm{d}} \right) \tag{2.46}$$

$$K_{\boldsymbol{k},\boldsymbol{k'}} = \frac{V^*_{\boldsymbol{k}} V_{\boldsymbol{k'}}}{2} \left(\frac{1}{e_{\boldsymbol{k}} - e_\mathrm{d}} + \frac{1}{U + e_\mathrm{d} - e_{\boldsymbol{k}}} \right) \tag{2.47}$$

In a condensed form Eq. (2.45) can be expressed as [112]:

$$H = J \boldsymbol{s} \cdot \boldsymbol{S} + K \boldsymbol{I} \ , \tag{2.48}$$

where J is the exchange scattering and K the potential scattering in real space, $\boldsymbol{s}$ the local conduction electron spin and $\boldsymbol{I}$ the identity matrix.

This interaction is shown in an illustrative manner in Fig. 2.17: On the left is the system in its ground state, with the impurity singly occupied and in direct contact with the electron bath of the metal. This ground state is two-fold degenerate, meaning that it can host one electron with spin up or down. Now a so-called 'spin-flip' process can occur. Electrons from the bath scatter at the impurity and the Heisenberg uncertainty principle allows for virtual excitations, so that either the impurity state is entirely unoccupied (the electron of the impurity is scattered into the electron bath) or that it becomes doubly occupied (an electron from the bath is scattered into the impurity). When relaxing back into the degenerate ground state, the spin orientation of the impurity electron can change. Naively speaking, it does not have to be the 'same' electron that comes back from the bath (lower path) or that goes back to the bath (upper path).

If we turn our attention back to the original problem of the resistivity minimum in metals, Kondo's model leads to a logarithmic increase in resistance at low temperatures [113]. Thus, the mystery of increasing R at low T was finally solved.

However, this in turn leads to a new problem: Kondo's model also predicted that the resistance becomes infinite with dropping temperatures [113]. This became known as the 'Kondo problem' and continued to baffle the scientific community. Anderson approached the issue in 1970 with his 'poor man's scaling approach' [114], but it was only finally proven and generalised to the 'numerical renormalisation group' by K. Wilson in 1975, a breakthrough significant not only to Kondo physics but so groundbreaking for perturbation theory in general that it earned him the Nobel prize in 1982 [115].

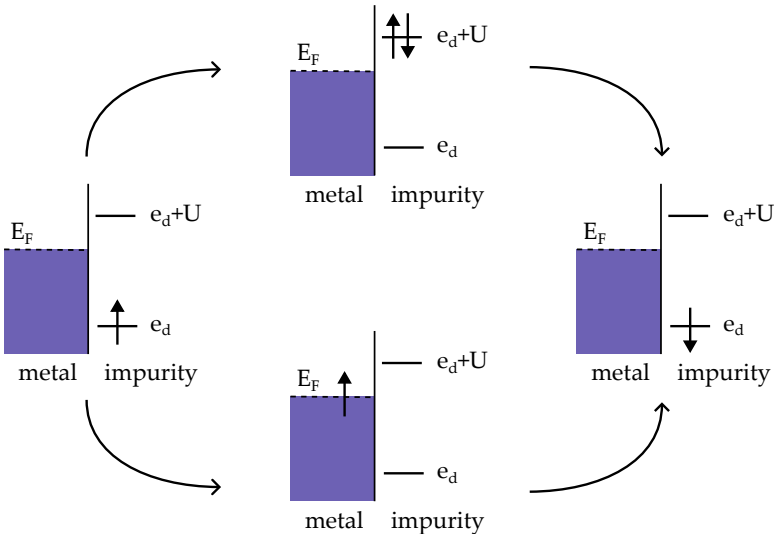

Figure 2.17: Illustration of the spin-flip processes of the Kondo effect: A singly-occupied impurity state with energy e_d is in contact with the electron bath of a metal substrate. The singly occupied state is separated from the doubly occupied state by the Coulomb repulsion U. Two possible virtual excitation paths are possible within the Heisenberg uncertainty relation: An electron from the metal can scatter into the impurity, leading to a doubly occupied virtual state (upper path), or the electron in the impurity can scatter into the electron bath, leading to an unoccupied virtual state (lower path). The system then relaxes back into its ground state, but the orientation of the impurity's spin can be reversed.

Many developments followed, that will only be briefly mentioned here, such as N. Andre and P. B. Wigman independently finding the exact solutions to the s-d-model with the Bethe ansatz in 1980 and 1981 [116, 117], so that finally an analytical model over the full temperature range existed. Many new systems started to be investigated as well, such as the Kondo lattice [118, 119] and heavy fermion systems [120, 121], just to name a few.

In the 80s, the approximate dynamic response functions were developed, which allow to calculate the one-electron DoS and its dynamic susceptibility [104]. This is especially relevant to STM/STS, as it shows that the Kondo effect creates a new many-body ground state close to E_F: a narrow resonance known as the Kondo resonance[9)] [104, 122]. This is illustrated in Fig. 2.18.

An important parameter to characterise the Kondo resonance is the Kondo temperature T_K, which relates to the halfwidth of the resonance Γ [122]:

$$T_\mathrm{K}(T=0) = \frac{\Gamma}{k_\mathrm{B}} \approx \Gamma \cdot 11.6 \, \frac{\mathrm{K}}{\mathrm{meV}} \, , \tag{2.49}$$

where k_B is the Boltzmann constant. The Kondo temperature divides two regimes: if the temperature of a system is below T_K, it is usually in the strong-coupling regime, if it is above, it is in the weak-coupling regime [104].

While the experimental existence of the Kondo resonance had been shown by bulk methods before [122–125], these methods did not have the spatial resolution necessary

[9)] Sometimes also called Abrikosov-Suhl resonance.

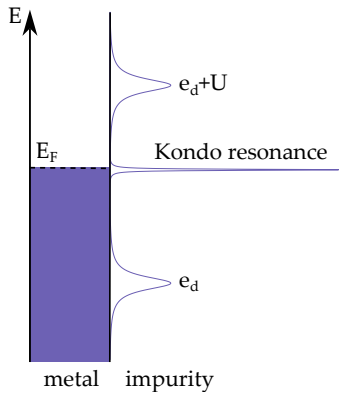

Figure 2.18: Schematic energy diagram of the DoS of an impurity in contact with a metal. The singly occupied state sits at energy e_d below the Fermi energy and the doubly occupied state at energy $e_\mathrm{d} + U$ above. The Kondo effect creates a new many-body ground state which can be detected as a narrow resonance close to E_F.

to probe single impurities, measuring an ensemble of impurities instead. But in 1998, the Kondo resonance was finally experimentally observed on single magnetic impurities with the high spatial resolution of STM/STS [126, 127].

In Ch. 4 we will also see a Kondo resonance in STS data of an investigated system where it will serve as a fingerprint for a magnetic interaction that allows us to probe the underlying mechanism.

3 Experimental Setup & Sample Preparation

After considering the theoretical background, we will now explore some of the more technical aspects that are necessary for conducting STM experiments. This chapter will give a brief introduction to the STM not as a method, but as a machine that needs to be operated, as well as the substrates used and how they were prepared to enable the measurements shown in Chapters 4, 5 and 6.

3.1 The Machine

The measurements in this thesis were conducted on three different low temperature STMs in ultra-high vacuum (UHV), with base temperatures of 4 K[1)]. While these three machines have slightly different capabilities, their essential working principle and setup is the same. A technical drawing of one of the three machines is shown in Fig. 3.1.

As visible in this figure, each machine is built out of two UHV chambers: the preparation chamber and the STM chamber, separated by a gate valve. Both chambers are individually pumped with an ion pump that allows us to reach pressures in the range of 10^{-10} mbar (depending on the setup, this can rise to 10^{-9} mbar or go down to 10^{-11} mbar). These pressures are reached from ambient conditions after extensive pumping with turbo-molecular pumps and 'baking', i. e. heating all UHV chambers up to above 100 °C to evaporate the water clinging to all surfaces. To improve pressure even further, the ion pumps are also equipped with titanium-sublimation pumps (TSP) that release titanium atoms into the chambers at regular intervals. These then bind to lighter molecules that could otherwise not be pumped and either immobilise them at the chamber walls or are pumped away together. These low pressures are needed to prevent contamination of the tip and sample, not only while measuring but also during the preparation stage. Additionally, the entire machine is decoupled from vibrations of the outside world by air-cushion feet.

The actual STM sits inside the STM chamber on the so-called STM head. It consists of the STM tip, which is grounded through the pre-amplifier, with which the tunnelling current is recorded, and the biased sample. Piezo-electric crystals allow for the precise positioning of the tip and a controlled scanning motion. The entire head is decoupled from the other parts of the machine by suspension from springs that are only in contact with the bottom of the cryostat. A permanent magnet reduces mechanical vibrations further through eddy-current damping.

[1)] One of the machines has the capability to go to a base temperature of 1 K. However, this was not used in the measurements conducted for this thesis.

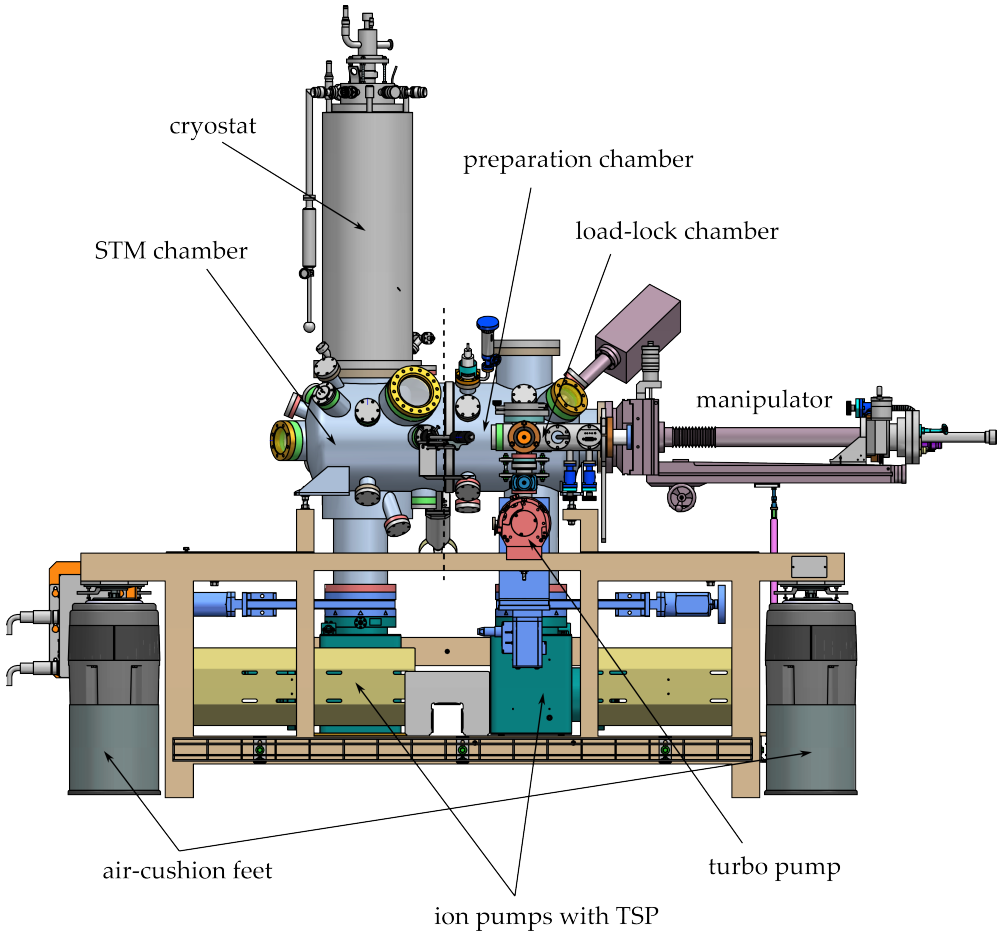

Figure 3.1: Technical drawing of one of the STMs used for measurements in this thesis ('Etna'). The main part of the machine are the two UHV chambers separated by a gate valve: The STM chamber holding the STM head that is cooled by the cryostat on top, and the preparation chamber used, as the name suggests, for sample preparation. The latter chamber offers many ports for connecting additional equipment. Movement between and within the chambers is facilitated by the XYZ and rotational manipulator. Both chambers are pumped to UHV conditions by ion pumps that are also equipped with titanium-sublimation pumps (TSP) to improve pressure even further. Additionally, a turbo-molecular pump is attached to the load-lock chamber. This chamber allows for relatively quick access from the outside to UHV. The entire system is decoupled from the outside world by air-cushion feet (image courtesy of Createc Fischer & Co. GmbH).

The cryostat consists of an outer tank filled with liquid nitrogen (77 K) and an inner tank with liquid helium (4 K). The measurement temperature can therefore be reduced to ~ 4 K which inhibits thermal drift and reduces the mobility of molecular and atomic adsorbates on the substrate to be measured.

Such a sample to be measured is usually prepared in the preparation chamber. This chamber therefore offers many ports for connecting, for example, Knudsen-cell evaporators for molecular evaporation, electron-beam evaporators for metal deposition, as well as needle valves for controlled dosing with gases such as Ne, Ar or H_2S. The preparation chamber also offers ovens for sample heating and the possibility to cool the sample down with liquid He or N. If the need arises, the chamber can also be extended with tools for a specific usecase, such as a cleaving mechanism for 2D materials.

To allow quick access to the outside world, a load-lock system is also attached. This small, separable chamber is directly attached to the turbo-molecular pump and therefore functions, as the name suggests, as a lock between UHV and ambient pressure.

Movement between and within chambers is facilitated by a manipulator. The design varies slightly from machine to machine, but in its essence it can transport the sample to different positions inside the UHV in a controlled manner via manual XYZ stages with rotational control.

All electronics are connected to the main control unit by Specs ('Nanonis') and controlled via the Nanonis software. The measurement data is acquired also via the Nanonis software (or, in parts of this thesis, by the CreaTec software) and treated using SpectraFox [128], WSxM [129], Igor Pro 7 and code written in Python, utilising the Nanonispy library [130].

3.2 The Surfaces

This section gives an overview of the different surfaces used for the measurements presented in this thesis as well as the preparation steps needed to achieve a good surface and how to ascertain one as such. The following two sections will detail how to achieve a good Au(111) surface and how to grow MoS_2 on top. Afterwards, the creation of additional S-vacancies in MoS_2 will be described. In the last section of this chapter, we will show how to work with the 2D-material $MoTe_2$ in its bulk form: how to achieve a good surface and the special considerations needed for working with a bulk 2D-material in an STM.

3.2.1 Au(111)

Au(111) is cleaned by a standard procedure of repeated sputter and anneal cycles: First, the surface is bombarded with focused Ne ions that are created by filling the preparation chamber with Ne gas to a pressure of $\sim 2 \times 10^{-6}$ mbar and operating the sputter gun at an acceleration voltage of 1.5 keV and an emission current of 4 mA for 10 min to 20 min. This removes unwanted adsorbates on the surface. Subsequently, the sample is heated to $\sim 530\,^{\circ}$C for 5 min to regain the flat crystal structure at the surface. Repeated cycles yield a pristine Au(111) surface as shown in Fig. 3.2. The herringbone

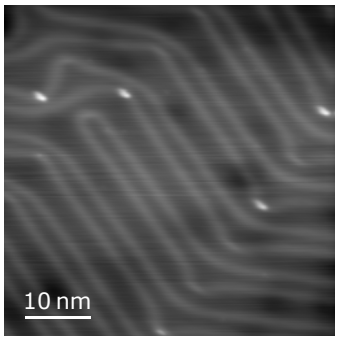

Figure 3.2: STM topography of a clean Au(111) surface. The bright lines crossing the image are the characteristic soliton lines of the herringbone reconstruction that separates the narrow hcp regions from the wider fcc regions. The bright protrusions are dirt that is pinned to the corners of this reconstruction (setpoint: 400 pA and 2 V).

reconstruction can be recognised clearly by the soliton lines separating the alternating hexagonal close-packed (hcp) and face-centred cubic (fcc) regions, that are of 2.5 nm and 3.8 nm width, respectively [131]. This surface reconstruction is the result of the surface breaking the symmetry of the crystal structure and the atomic structure yielding to the acting stresses [132]. It is both a topographical and an electronic effect, where the soliton lines are formed by Au atoms sitting on the bridge sites in-between the two regions and standing waves forming because of electrons scattering at these atoms [131]. In STS, Au(111) shows a characteristic Shockley surface-state [133] at −490 mV.

3.2.2 MoS_2/Au(111)

MoS_2 is grown on an atomically clean Au(111) surface after an adapted recipe from [134]: First, the Au(111) crystal is annealed to ∼ 550 °C. Once this temperature is reached, H_2S gas is filled into the preparation chamber with a pressure of about 1×10^{-5} mbar. At the same time, elemental Mo atoms are evaporated onto the Au(111) surface from a Mo rod mounted inside an electron-beam evaporator at a flux current of roughly 10 nA. Depending on the desired coverage and island size, the exact flux values and the evaporation times have to be adjusted. In this step, the hot Au(111) surface acts as a catalyst to 'crack' the H_2S into its H and S components. The elemental S in turn reacts with the Mo atoms to form MoS_2 on the surface.

Once the Mo evaporation is stopped, the Au(111) sample is kept at the same temperature in the H_2S atmosphere for 10 min to continue to provide S atoms to potentially 'heal' any S defects stemming from S insufficiencies. Afterwards, the H_2S is pumped out from the chamber and the Au(111) annealed for a few minutes longer to remove potential unwanted adsorbates and to prevent further contamination. When working with H_2S it has to be kept in mind that it cannot be efficiently pumped with turbomolecular pumps. The vacuum chamber filled with H_2S therefore remains contaminated for at least a few hours after the preparation procedure[2)].

[2)] It can therefore also be helpful to post-anneal the grown MoS_2 to ∼ 300 °C one more time after the pressure in the vacuum chamber has normalised to remove more adsorbates.

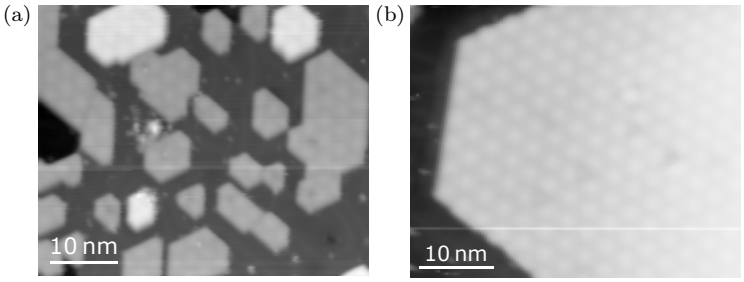

Figure 3.3: STM topographies of MoS_2 islands grown on Au(111). Different preparation procedures yield differently sized islands: (a) small ones of < 10 nm size, clustered closely together, covering the entire Au(111) surface rather evenly, and (b) big islands of > 100 nm in size, with large areas of clean Au(111) between them (setpoints: 2 V, 200 pA).

Monolayer MoS_2 grown on Au(111) in this manner appears in STM topography as in Fig. 3.3. Depending on the evaporation parameters of Mo flux current and deposition time chosen, it can grow in either small islands of less than 10 nm-size close together (Fig. 3.3a, high flux for a short period of time, 'fast growth'), or large islands of more than 100 nm in size with large areas of clean Au(111) in-between (Fig. 3.3b, lower flux for a longer period of time, 'slow growth'). These islands, regardless of size, appear with their characteristic moiré pattern, the origin of which was detailed in the previous chapter in section 2.3.2.

While the majority of MoS_2 grown in this fashion can be considered 'pristine', some defects, intrinsic to any growth process, cannot be avoided. Depending on the requirements for the experiment planned, it is advisable to examine the islands for defects at low bias voltages (~ 50 mV), as they do not appear clearly in the STM topography at the high bias voltages (~ 2 V) frequently used for this system for stability.

For the measurements presented in Ch. 5, the surface is now ready for molecular deposition (details in Ch. 5.1). For the system in Ch. 4, one additional preparation step is needed: creation of S-defects.

3.2.3 Top-layer S-defects in MoS_2/Au(111)

Following a successful MoS_2 growth as detailed in the previous section, the sample is annealed again to $\sim 300\,^{\circ}$C to remove any unwanted adsorbates remaining from the growth process. The sample is then left to cool down to room temperature. Top-layer S vacancies are created in the pristine MoS_2/Au(111) by sputtering with Ne ions at low energy (~ 550 eV) for 4 s under a 45°-angle. The sputter gun is kept at the same conditions for 10 min before the actual sputtering, to allow for the dissipation of any possible contaminations present on the sputter gun itself.

This results in MoS_2 with significantly more top-layer S-vacancies than naturally present after the growth process. As described in Ch. 2.3.2, these defects appear as a dark centre with a triangular rim around them (see Fig. 3.4) and a characteristic electronic signature. An appropriate number of defects with enough separation from one another is necessary for anchoring of molecules, as will be shown in Ch. 4.4.

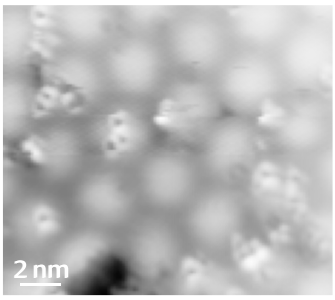

Figure 3.4: STM topography of MoS_2/Au(111) after additional low-energy sputtering. The MoS_2 island is sprinkled with triangular bright features with a dark centre: S-vacancies in the upper S-layer of MoS_2 (setpoint: 50 mV, 200 pA).

3.2.4 $MoTe_2$

2H-$MoTe_2$ differs in the preparation needed from the substrates described in the previous sections, since it is a bulk 2D-material. It can, for example, not be cleaned like metal substrates such as Au(111) with sputtering and annealing, because the two-dimensional layers would break or undergo a phase transition to a different crystal phase (see Ch. 2.3.3 for more details).

The 2H-$MoTe_2$ crystal used for the measurements in this thesis is a commercial crystal purchased from HQ Graphene. Prior to mounting the crystal to a sample plate, it had to be cut into smaller pieces with a scalpel to fit the sample holder size. While care was taken to cut cleanly, some shearing of layers could probably not be avoided.

To create a good electrical contact, the crystal shard was glued to the Mo sample holder with conducting silver epoxy. To ensure electrical contact to the uppermost layer, notoriously difficult to achieve with TMDCs [135–138], we created a 'sidecontact' with conducting carbon paste. Everything was hardened in an oven at $\sim 100\,^{\circ}\mathrm{C}$ and the resulting $MoTe_2$ shard on-top of the sample holder can be seen in Fig. 3.5a.

To ensure that the surface of the substrate is devoid of contaminants, we 'cleave' the uppermost layer(s) with sticky tape. Here, the best direction for the cleave while considering the geometries of the sample holder and the cleaving mechanism has to be determined before glueing the crystal in place. A few test cleaves are recommended in ambient conditions.

For cleaving inside the UHV chamber, we utilise a cleaving mechanism that consists of a ball bearing on a movable part (e. g. a transfer bar) wrapped with sticky tape (sticky side up), as shown in Fig. 3.5b. This allows for multiple cleaves *in vacuo*.

An 2H-$MoTe_2$ crystal prepared as such can then be investigated in the STM without exposure to ambient conditions after the cleave. When measuring with the STM, there has to be taken care that the STM tip does not come into contact with the substrate in an uncontrolled fashion. Since the material is very prone to 'flaking', the tip can easily become contaminated. Removing such a flake from the tip requires a tedious amount of tip cleaning procedures, from controlled indentations into a metal surface of choice, exposing the tip to high voltages and currents, to even more drastic methods such as sputtering the tip or even macroscopically shortening it. It is therefore highly advisable to

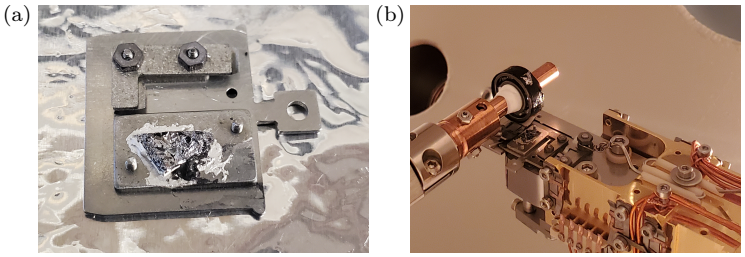

Figure 3.5: (a) Photograph of a $MoTe_2$ shard glued on a (dual) sample holder with conducting silver epoxy and a small 'blob' of black carbon paste. (b) Photograph of the cleaving mechanism inside the preparation chamber of one of the machines used in this thesis. A ball bearing is attached to the transfer bar of the load-lock chamber (left-hand side of image). On the ball bearing, double-sided carbon tape is attached to the rotating part (black tape). The sample holder with the $MoTe_2$ shard is directly below the ball bearing on the manipulator, hidden from view. The two silver traces on the carbon tape are two previous cleaves of $MoTe_2$.

exercise caution and often err on the side of protecting the tip. Additionally, it is advisable to first approach the surface with a high bias voltage applied, to minimise the risk of using a setpoint inside the bandgap of the material, and to maximise the probabilities of creating a tunnelling current even if the electrical contact to the uppermost layer is not ideal.

After all these preparation steps, we can finally turn our attention to the results of the measurements conducted on the samples presented in this chapter.

4 Different adsorption scenarios of CF_3-3P-S(H) on Au(111) and MoS_2/Au(111)

As introduced in Chapter 2.3, transition-metal dichalcogenides (TMDCs) are a group of materials which, due to their inherent 2D-nature, create a plentiful playground for exploring composite materials. But their two-dimensionality also has drawbacks: very small amounts of (atomic) defects, that mostly cannot be avoided, have a significant effect on their electronic properties. This has already been utilised in a positive way to selectively tune systems by including defects purposefully [139–141]. This is often taken a step further by functionalising these defects with molecular adsorbates [24–26] which can lead to further modifications to the electronic structure [86, 142], leading to different possible applications [32, 33, 143], as has already been explored in Chapter 2.3.

In this chapter, we study a molecular system based on the thiol-terminated organic molecule 4"-(trifluoromethyl)-[1,1':4',1"-terphenyl]-4-thiol (CF_3-3P-SH) (see Fig. 4.1a) and investigate its bonding properties to purposefully created S vacancies in the terminating S layer of MoS_2 on Au(111). As detailed in Ch. 2.3.2, the interaction of MoS_2 with the Au substrate localises a single negative charge at the vacancy [56, 57]. The vacancy sites are therefore expected to be highly reactive and offer potential anchoring sites, especially as thiol-based molecules tend to form covalent bonds with S vacancies [142, 144] and passivate them in turn.

This chapter will first give a short overview of the sample preparation procedure, and then give details about the behaviour of CF_3-3P-SH both on the bare Au(111) substrate and on MoS_2/Au(111) with and without the creation of additional S-defects. The latter part is also divided in two to reflect the two possible electronic structures that have been observed.

4.1 Molecular Details & Sample Preparation

The CF_3-3P-SH molecules were synthesised by B. Kobin and J. Schwarz of the AG Hecht at the HU Berlin. The molecules consist of a para-terphenyl group (three phenyl groups in a tilted configuration) with a trifluoromethyl-endgroup on one end and a thiol-endgroup on the other (see Fig. 4.1a). Macroscopic amounts appear as a white-yellowish powder, as shown in the photograph in Fig. 4.1b.

The relaxed structure of the gas-phase CF_3-3P-SH molecule is calculated using Gaussian16 [145] with the functional B3LYP and the basis set 6-31++g(d,p)[1)]. For the free

[1)] For an introduction into the different basis sets and their properties, see for example [146].

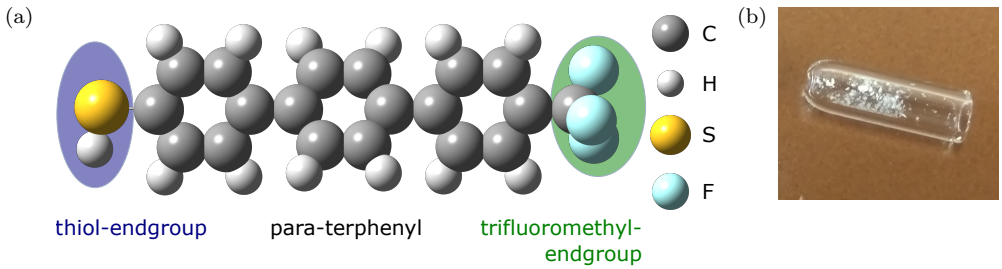

Figure 4.1: (a) Molecular model of CF_3-3P-SH in gas-phase: a para-terphenyl group of three phenyl rings tilted with respect to each other with a thiol-endgroup attached on one end (shaded in blue) and a trifluoromethyl group on the other (shaded in green). (b) Photograph of a quartz-crucible filled with yellowish-white CF_3-3P-SH powder used for evaporation in a Knudsen cell.

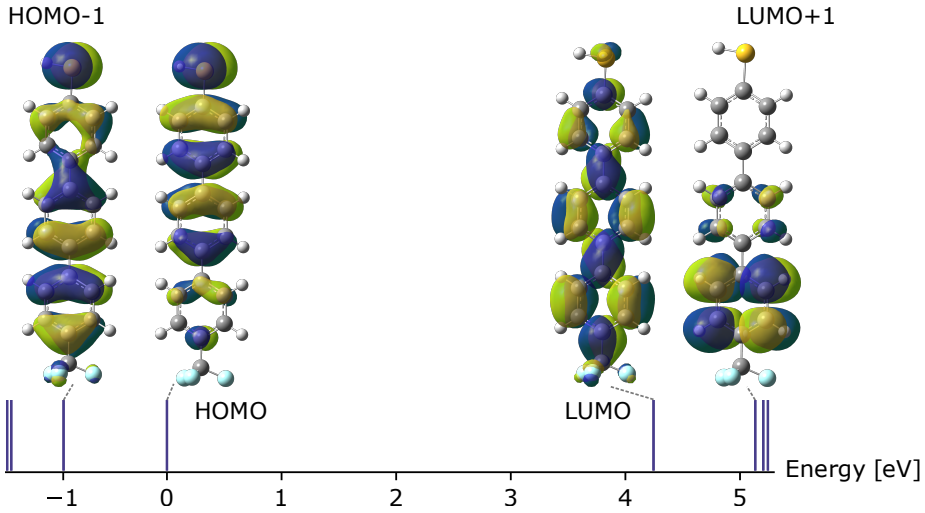

Figure 4.2: Simulated molecular orbitals of gas-phase CF_3-3P-SH calculated using Gaussian16 with the functional B3LYP and the basis set 6-31++g(d,p), and their relative energies. The energy scale is aligned to the energy of the HOMO. The calculated HOMO-LUMO gap is $\sim 4.2\,\mathrm{eV}$.

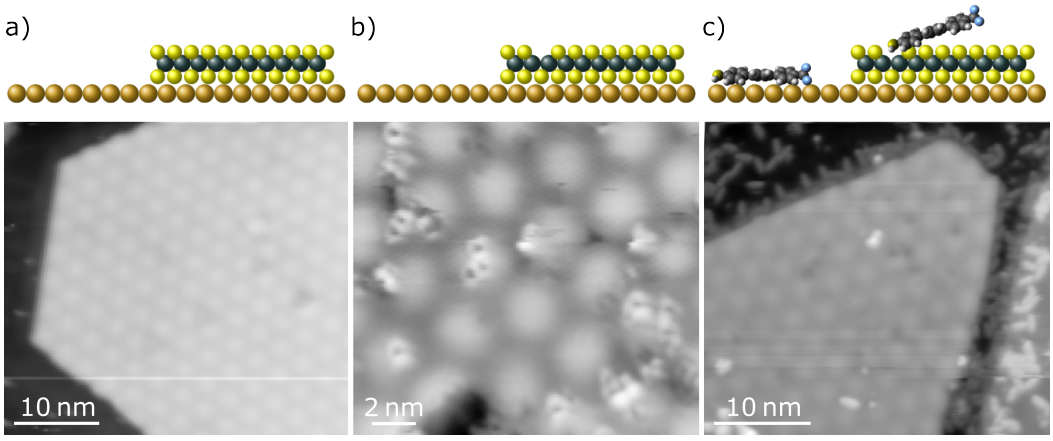

Figure 4.3: Overview of the preparation steps: a) Growth of MoS_2 on Au(111), resulting in large MoS_2 islands (Setpoint: 2 V, 200 pA). b) Creation of top-layer sulphur vacancies in MoS_2 on Au(111), visible as triangular shapes, by sputtering with low-energy Ne ions. (Setpoint: 50 mV, 200 pA). c) Evaporation of CF_3-3P-SH and subsequent post-annealing: Most molecules adsorb on the Au(111) surface, with only few remaining on the MoS_2. (Setpoint: 2 V, 30 pA).

molecule, the phenyl rings are slightly rotated along the molecular backbone with respect to each other. Electronically, the free molecule is calculated to have a HOMO-LUMO gap of ~ 4.2 eV, with molecular orbitals (MOs) as shown in Fig. 4.2. While these energies will change when placed upon a surface, mainly because of Coulomb interaction as described in Ch. 2.4, as well as deformation of the molecular structure when placed on a surface, this relatively simple calculation gives us a good first approximation of the molecular characteristics.

To measure these CF_3-3P-SH molecules in STM, the substrates of Au(111) for the first section and MoS_2/Au(111) for the following section were prepared as described in Ch. 3.2.1 and 3.2.2, respectively. This results in clean, flat Au(111) surfaces with large terraces (> 100 nm) and large MoS_2 islands (> 50 nm) as shown in Fig. 4.3a. For the last section in this chapter, top-layer S-defects as detailed in Ch. 3.2.3 were subsequently created in the MoS_2/Au(111) substrate, resulting in a defect-rich surface as shown in Fig. 4.3b. The density of the defects can be tuned by changing the sputtering conditions. For molecular evaporation, we use a Knudsen cell filled with CF_3-3P-SH molecules heated to an evaporation temperature of 80 °C to 90 °C.

As we will explore in the following sections in more detail, different sample temperatures during molecular deposition lead to quite different adsorption behaviour of the CF_3-3P-SH molecules. Especially for evaporation on MoS_2, a cold sample temperature of < -110 °C has to be chosen since large molecules such as CF_3-3P-SH have a low diffusion barrier on MoS_2 [85]. For the anchored CF_3-3P-SH molecules on MoS_2/Au(111) in the last section of this chapter, the substrate is additionally heated to -50 °C for roughly 5 min directly after evaporation which causes most CF_3-3P-SH molecules to diffuse to the Au, with only a few remaining on the MoS_2, as visible in Fig. 4.3c.

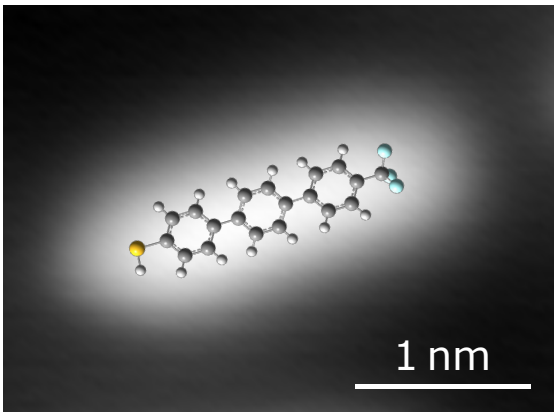

Figure 4.4: STM topography of a single CF_3-3P-SH molecule adsorbed on Au(111), with gas-phase molecular model laid on top. The molecule appears as an elongated oval protrusion, with no internal modulation. The endgroups cannot be distinguished from each other in STM topography, and the model has been placed in an arbitrary orientation (setpoint: 100 mV, 30 pA).

4.2 Physisorption of CF_3-3P-SH on Au(111)

After molecular deposition of CF_3-3P-SH on Au(111), uniform elongated oval protrusions appear on the Au(111), as shown with a molecular model overlay in Fig. 4.4. From the shape and dimensions of these protrusions it is most likely that the CF_3-3P-SH molecules are adsorbed flat on the Au(111) surface. No internal modulation is visible in the STM topography, and the two endgroups are not distinguishable from each other, so an arbitrary orientation was chosen for the molecular model in Fig. 4.4.

Different sample temperatures during molecular deposition result in different molecular structures forming on the Au(111) surface. A few examples of such structures are shown in Fig. 4.5 (details about the respective preparation conditions can be found in the figure caption): At low sample temperatures ($< -150\,°C$), the molecules are stochastically distributed across the Au(111) surface (Fig. 4.5a), with slight clustering, as shown in more detail in Fig. 4.6. The herringbone surface reconstruction is still visible next to the molecules, and does not influence the adsorption position of the molecules. The molecules can move laterally upon interaction with the STM tip during the scanning motion or by ramping the bias voltage in the range of $-0.6\,V$ to $1\,V$, as also shown in Figs. 4.6a and 4.6b. It can therefore be concluded that there is no strong interaction between the CF_3-3P-SH molecules and the Au(111) surface at these evaporation conditions. As expected, the molecules have minimal kinetic energy at these low temperatures, so that they are physisorbed close to their place of arrival on the surface, without enough energy to overcome the diffusion barrier to diffuse to possibly energetically more favourable adsorption sites.

This picture changes with increasing sample temperature during deposition. At a sample temperature of $-120\,°C$ (and double the deposition time than in the previous preparation, so a higher total number of deposited molecules), the molecules form bigger clusters on Au(111). In smaller clusters (~ 10 molecules, marked in green in Fig. 4.5b), they begin to follow the herringbone reconstruction, avoiding the soliton lines and

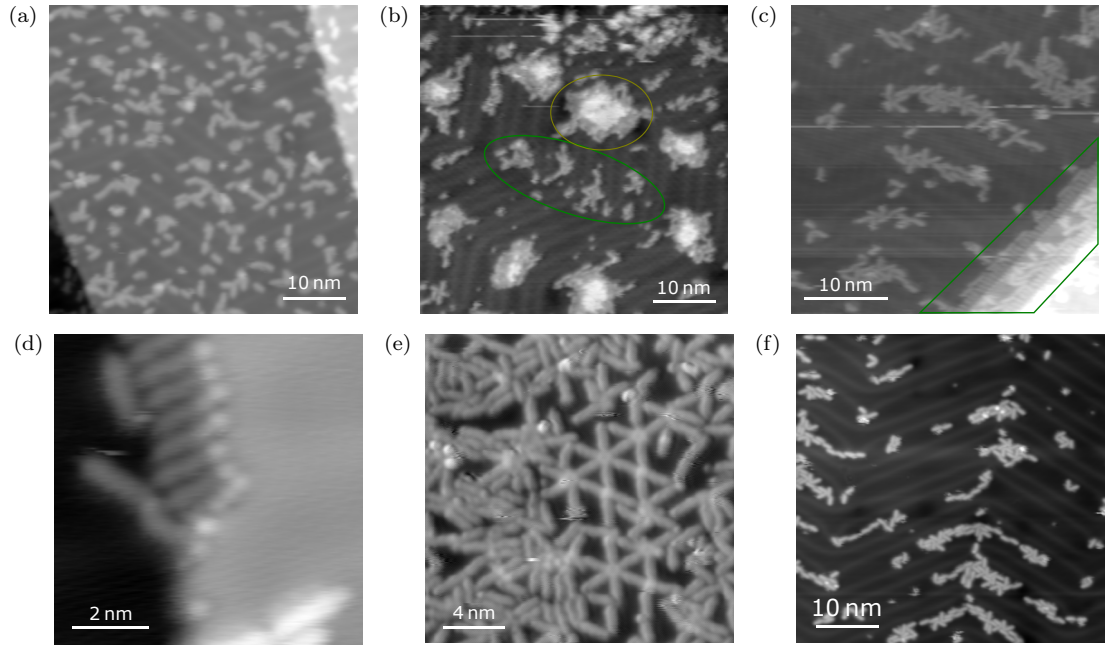

Figure 4.5: STM topography of CF_3-3P-SH on Au(111) under different evaporation conditions. (a) $T_{\text{sample}} = -150\,°\text{C}$, $T_{\text{evap}} = 80\,°\text{C}$, $t = 5\,\text{min}$: The CF_3-3P-SH molecules are adsorbed stochastically distributed across the surface, forming small clusters of ~ 5 molecules. See Fig. 4.6 for a detailed view (setpoint: 330 mV, 50 pA).
(b) $T_{\text{sample}} = -120\,°\text{C}$, $T_{\text{evap}} = 80\,°\text{C}$, $t = 10\,\text{min}$: The molecules form bigger clusters that align along the soliton lines of the herringbone reconstruction, preferably on the wider fcc phases. Big clusters show double the apparent height in their middle. See Fig. 4.7 for a detailed view (setpoint: 150 mV, 50 pA).
(c) $T_{\text{sample}} = -130\,°\text{C}$ to $-150\,°\text{C}$, $T_{\text{evap}} = 80\,°\text{C}$, $t = 5\,\text{min}$, post-anneal to $T_{\text{sample}} = 20\,°\text{C}$: The molecules still form unordered clusters that follow the herringbone reconstruction (setpoint: 260 mV, 100 pA).
(d) Same preparation as in (c): At the step edges, CF_3-3P-SH molecules align parallel to each other and nearly perpendicular to the edge. At the point of contact, a bright circular protrusion is visible (setpoint: 530 mV, 190 pA).
(e) Two consecutive evaporation procedures: First, $T_{\text{sample}} = -110\,°\text{C}$, $t = 4\,\text{min}$, post-anneal to $T_{\text{sample}} = -50\,°\text{C}$, then $T_{\text{sample}} = -110\,°\text{C}$, $t = 10\,\text{min}$, post-anneal to $T_{\text{sample}} = -70\,°\text{C}$, $T_{\text{evap}} = 80\,°\text{C}$ for both: The molecular coverage is very high, the herringbone reconstruction is not visible anymore. The molecules begin to form ordered structures of either parallel alignment or 'star' shapes. See Fig. 4.8 for a detailed view (setpoint: 400 mV, 40 pA).
(f) $T_{\text{sample}} = 20\,°\text{C}$, $T_{\text{evap}} = 80\,°\text{C}$, $t = 5\,\text{min}$, $T_{\text{sample}}^{\text{max}} = 30\,°\text{C}$: Similar adsorption properties to (c), only the clusters follow the herringbone reconstruction in a more pronounced way (setpoint: 1 V, 120 pA).

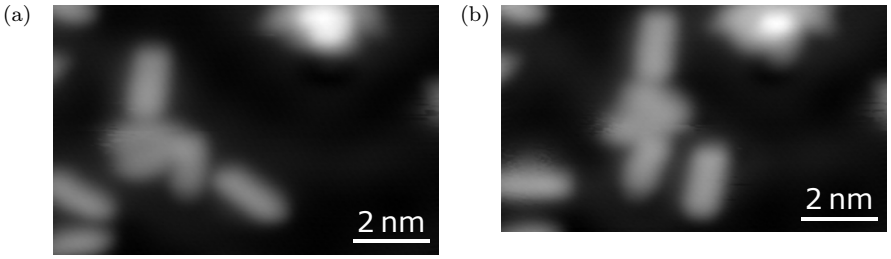

Figure 4.6: STM topography of a detailed view of the preparation shown in Fig. 4.5a. The individual CF_3-3P-SH molecules loosely cluster together. The bias voltage was sweeped from −0.6 V to 1 V between the two images. The molecules moved laterally towards/away from the STM tip during the sweep (setpoint: 100 mV, 20 pA).

preferably adsorbing on the wider fcc phases. Large clusters (> 30 molecules, marked in yellow in Fig. 4.5b), cross soliton lines and show a peculiar increase in apparent height in the middle, as visible in Fig. 4.7 in more detail. The height profiles in Fig. 4.7c, taken along the green dotted lines in Fig. 4.7a and 4.7b, show that the centre of the island appears with roughly double the height than the surrounding island. This suggests the formation of a second molecular layer on top of the first one. So far, these 'double-decker' structures have only been observed at a high evaporation rate and therefore high concentration of incidental molecules. Interestingly, sweeping the bias voltage while on top of the raised island from 1 V to −1 V induces a peculiar change in topography, as visible going from Fig. 4.7a to 4.7b: Some areas of the island that previously appeared with a lower apparent height now appear with the doubled height, with simultaneous change in the surface area covered. This can also be seen clearly in the two height profiles in Fig. 4.7c that are taken along the same green-dotted trace before (green line) and after the voltage sweep (grey line). Since the 'double-decker' structures are most likely a second layer of molecules adsorbing on top of the lower islands, it is possible that the voltage sweep provides enough energy for a molecule on the surface to move onto the island. Interestingly, this suggests that the molecules prefer to form these close-packed structures when their local concentration is high. But since the islands show little modulation in STM topography, it is difficult to ascertain which of the shapes is a single molecule and, consequently, how the structure looks like at the molecular level. To complicate matters further, the possibility of 'dirt' (i. e. broken molecules, contaminants, etc.) adsorbing and accumulating on the surface cannot be fully excluded as well. To determine the cause behind the increased apparent height would require more detailed measurements such as with an atomic force microscope (AFM), to resolve the molecular structure of these islands.

Increasing the sample temperature during molecular evaporation of CF_3-3P-SH or in a post-annealing step even further does not have significant influence on the adsorption properties. As visible in Fig. 4.5c, at an evaporation temperature of −130 °C, post-annealed to 20 °C, the molecules still form clusters that follow the herringbone reconstruction. Going up to room temperature for the sample during deposition leads to nearly identical coverage and adsorption properties, as visible in Fig. 4.5f. Only the 'double-decker' islands are gone, which is most likely an influence of the reduced molecular

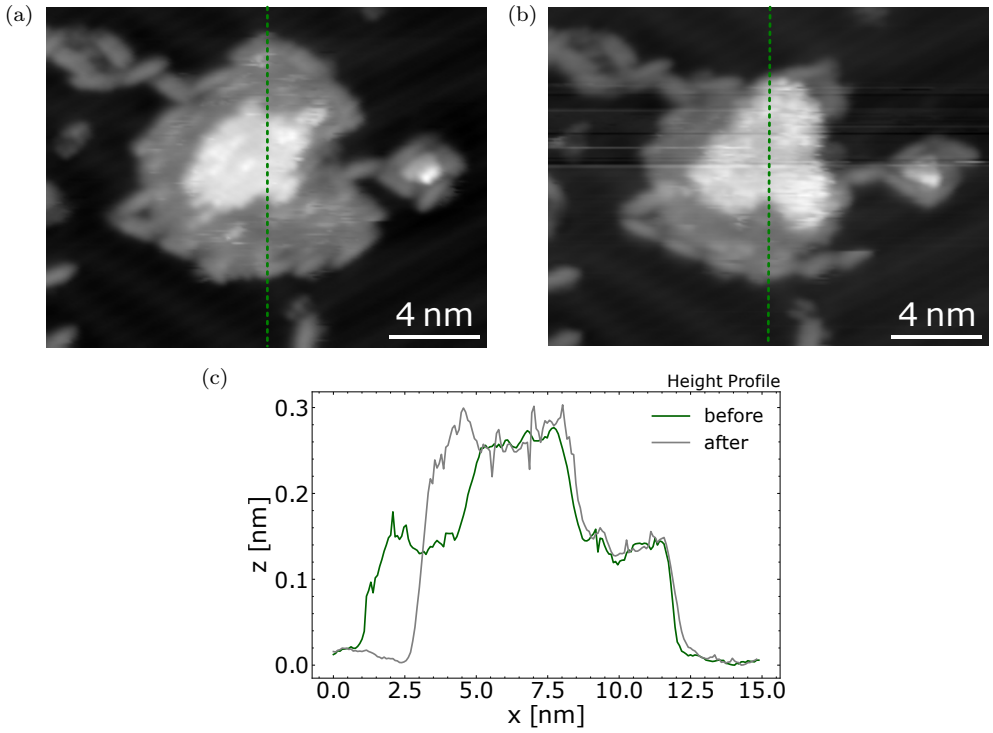

Figure 4.7: (a) and (b) STM topography of a 'double-decker' molecular island, from the preparation shown in Fig. 4.5b. The individual molecules are difficult to distinguish in the STM topography. The voltage is sweeped between 1 V and −1 V on top of the higher part of the island between (a) and (b), which results in a change in topography. (c) Height profile taken along the green dotted lines in (a) (green) and (b) (grey). (Setpoints: (a) 300 mV, 20 pA, (b) 200 mV, 30 pA.)

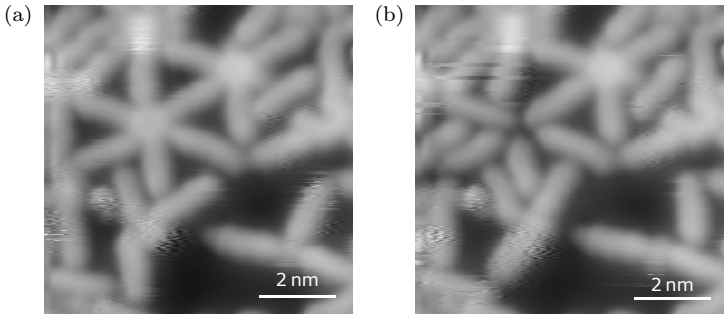

Figure 4.8: STM topography of a 'star' consisting of six CF_3-3P-SH molecules. Between (a) and (b) the bias voltage was ramped from 2 V to −1 V while in the vicinity of the connecting point. As a result, the molecules are pushed apart (setpoint: 400 mV, 40 pA).

coverage. But another interesting observation can be made at the step-edges of the Au(111) surface (green box in Fig. 4.5c): There, CF_3-3P-SH molecules align themselves perpendicular to the edge and parallel to each other. The point of contact between molecule and edge has a higher apparent height, visible as circular protrusions along the step edge in Fig. 4.5d. This suggests an interaction between molecule and edge, potentially the formation of a S-Au bond at the exposed Au atoms.

Apart from evaporation temperature, the molecular coverage also has an influence on the adsorption properties. If we now increase the molecular coverage at low temperatures, different shapes begin to form. At longer evaporation times (14 min) at slightly higher deposition temperatures of −110 °C and a post-annealing step to −70 °C, the molecular coverage on Au(111) becomes very high: The herringbone reconstruction is barely visible anymore, and the molecules begin to form ordered structures on the surface. There are areas of molecules lying parallel to each other, and others where 'star'-shapes are beginning to form a regular grid with three-fold symmetry (see Fig. 4.5e). These 'stars', consisting of six molecules, show a brighter circular feature at their common centre. The molecules are, however, not strongly bound together, as ramping the bias voltage between 2 V and −1 V while in the vicinity of the connection point can push them apart easily, as shown in Fig. 4.8a to 4.8b.

The stars most likely follow the three-fold symmetry of the underlying Au(111) surface. The orientation of the molecule is a crucial piece of information to understand this structure. In the case of the same endgroups pointing towards each other, it is possible that this structure stabilises around a Au adatom, especially on the SH side [147, 148]. Looking closely at the structure in Fig. 4.8, it can be seen that while the connecting point of the six molecules has been easily perturbed, for the molecules linking to the next star-shape(-fragment), that link has remained intact. While this could be a result of the distance to the STM tip during the sweep, it could also be an indication for the different endgroups, so that for example the centre pushed apart was the CF_3-groups pointing to one another, which only interact weakly with one another and the surface [149]. The other side could then be a stronger, possibly Au-mediated, S-bond between the molecules.

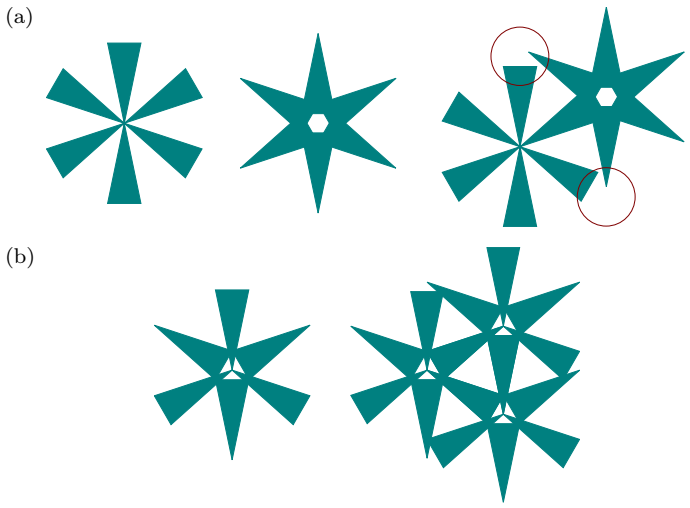

Figure 4.9: Schematic representation of possible molecular geometries of the 'star'-shapes consisting of six CF_3-3P-SH molecules. One triangle represents one CF_3-3P-SH molecule, with the short and wide ends indicating the different endgroups. (a) Three-fold symmetric stars consisting of the same endgroups joined together. Putting both structures together reveals that it is geometrically impossible to create a large-scale lattice out of only these two components, as the joints marked with a red circle already prove problematic. (b) Six molecules arranged with alternating endgroups arranged to form a star. This structure can form extended lattices.

Since the star-structure has only partially begun to form in our investigated system, it is difficult to create a large-scale model. A simple sketch reveals quickly that due to the geometry of a two-fold system (the molecule) meeting a three-fold system (the Au(111) lattice), a simple upscaling of six molecules pointing the same endgroups together is geometrically impossible, as illustrated in Fig. 4.9a. It is therefore either a more complex structure with alternating endgroups at one connection point, as schematically depicted in Fig. 4.9b, which would lead to the same type of connection everywhere, or these star-shapes simply cannot form a regular extended structure with a small unit cell, without symmetry breaking elements or a more complex superstructure to stabilise the pattern.

To shed light on the intermolecular interaction, possibly mediated by the surface, one would need to first grow these star-structures over a more extended surface area, with fine-tuned evaporation parameters. AFM measurements could again ascertain which end of the molecule is which. All in all, these star-structures could prove interesting if they self-assemble into stable extended regular structures with a stronger bond between the individual CF_3-3P-SH molecules.

Electronically, single CF_3-3P-SH molecules adsorbed on Au(111) show one main feature in $\mathrm{d}I/\mathrm{d}V$ spectroscopy: a broad state at $\sim 2.7\,\mathrm{V}$, as clearly visible in Fig. 4.10. This is most likely the LUMO of the molecule, since no further state can be resolved for $\sim 3.5\,\mathrm{V}$ below it in the recorded bias range, and only the theoretically calculated HOMO-LUMO gap of $\sim 4.2\,\mathrm{eV}$ is larger than this energetical separation. While the energy levels of the molecule are indeed changed on a surface when compared to the

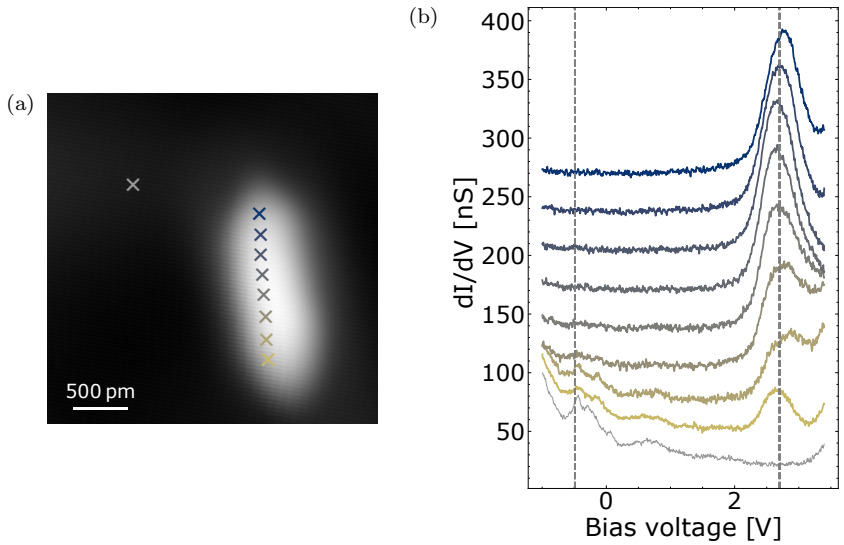

Figure 4.10: (a) STM topography of a single CF_3-3P-SH molecule on Au(111) (setpoint: 1 V, 100 pA). (b) dI/dV spectra taken across a CF_3-3P-SH molecule adsorbed as a single molecule on Au(111). The spectra are taken at the positions marked with a cross in the topography, with the colour of the cross corresponding to the colour of the spectrum. The Au(111) reference spectrum is plotted in grey at the very bottom of the graph. The spectra are offset vertically from each other for better visibility. The grey dashed lines are drawn at −0.49 V (the energy of the Au(111) surface state) and at 2.7 V as guides to the eye (feedback opened at 3.4 V, 100 pA, 20 mV modulation amplitude).

gas-phase molecule, a strong deviation caused by e. g. charge transfer is unlikely because of the weak interaction of these single molecules with the Au(111) substrate. Any other MO is therefore unlikely.

The exact lineshape and energetical position of this molecular resonance varies slightly across the molecule, as shown in Fig. 4.10. Most likely, the underlying molecular state has vibrational components that cannot be resolved individually on the Au(111) substrate because of their short lifetime. They therefore appear as one broad resonance. As shown by Pavliček et. al. in Ref. [102], the relative contributions to the tunnelling current of these components change spatially, which leads to an apparent shift in energy and changes in the lineshape of the envelope peak. This is likely the case for our system as well. Another factor could also be vibration-assisted tunnelling (VAT) (see Ch. 2.6). This effect causes an apparent shift in energy caused by the change in overlap of the MOs with the tip wavefunction because of the vibrational modes of the molecule.

This shift of the LUMO resonance is seen even more strongly for small molecular clusters of CF_3-3P-SH, evaporated at a sample kept at room temperature during deposition. They also show the broad molecular resonance of the LUMO at positive biases, but its energetical position as shown in Fig. 4.11b, varies more than for the single molecule. This could point towards an influence of the neighboring molecules in the cluster that can change the spatial distribution of the vibrational components, leading to this perceived energy shift, or another form of intermolecular interaction.

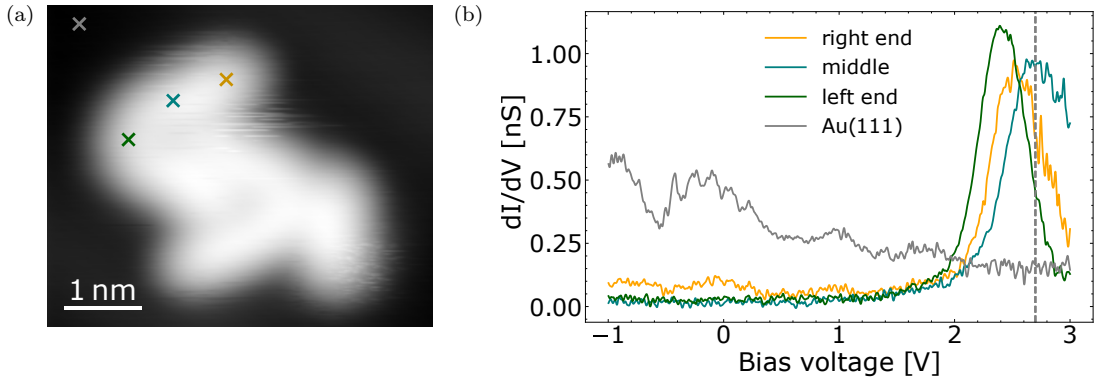

Figure 4.11: (a) STM topography of a small cluster consisting of five CF_3-3P-SH molecules (setpoint: 1 V, 700 pA). (b) dI/dV spectra recorded on one molecule of the cluster at the position marked with colours corresponding to the spectra in (a) and Au(111) reference spectrum in grey. A broad state can clearly be seen, with its centre at 2.7 V (blue spectrum, recorded on the middle of the molecule), at 2.5 V (yellow spectrum, recorded on the right end of the molecule) and at 2.4 V (green spectrum, recorded on the left end of the molecule). The grey dashed line is drawn at 2.7 V as a guide to the eye (feedback opened at 3 V, 700 pA).

No other molecular resonances could be observed because of the lack of stability of the CF_3-3P-SH molecules on the Au(111) surface at higher bias voltages. Especially higher negative biases could not be probed without inducing changes in the molecule, mostly because the molecule moves under the STM tip during the bias sweep.

All in all, different sample temperatures during molecular deposition and the different molecular coverages change – unsurprisingly – the structures forming on the surface. After overcoming the diffusion barrier with thermal energy somewhere between −150 °C and −120 °C, the CF_3-3P-SH molecules begin to form ordered structures that range from unordered clusters to local regular structures. At the investigated evaporation parameters, the molecules do not form a strong chemical bond with the surface, as lateral movement of the molecules can still be induced relatively easily by the STM tip. The formation of large-scale order of the physisorbed molecules suggests that the interaction between the molecules reduces the total energy of the system, and bonding together is therefore energetically favourable. This could be utilised as a building block for self-assembled regular molecular structures that still lie flat on the surface.

To explore the molecular electronic properties further, we now move to MoS_2/Au(111), where the substrate's decoupling properties will lead to better insights into the electronic structure.

4.3 Physisorption of CF_3-3P-SH on MoS_2/Au(111)

At very low sample temperatures ($< -150\,°C$) during deposition, the CF_3-3P-SH molecules on MoS_2/Au(111) also appear as oval-shaped protrusions as on the Au(111) as described in the previous section, but are more prone to clustering together in small clusters of < 10 molecules, so that no entirely separated single CF_3-3P-SH molecules can be found in these conditions on the MoS_2, as shown in the overview topography in Fig. 4.12a and in the detail view in Fig. 4.12b.

Fig. 4.13 shows a dimer with molecular model on top. The molecules still do not show any internal modulation in the STM topography, only the thickness of the two ends could be ever so slightly different, possibly pointing to the fact that the interaction of both endgroups with the MoS_2 might be more different than on the Au(111). The molecules lie flat on the surface but are very mobile on the MoS_2 and move laterally after minimal tip interaction, either during scanning or through a voltage sweep above 1 V or below -1 V, as visible when comparing Figs. 4.13a and 4.13b.

At higher sample temperatures of $-120\,°C$ during molecular evaporation and if the molecular coverage on MoS_2 is high enough, it is possible to create large clusters of > 100 CF_3-3P-SH molecules on MoS_2, as shown in Figs. 4.12c and 4.12d. These large clusters are unordered and still relatively mobile when probed by the STM tip. They also show a greater variation of apparent heights, which could point towards some CF_3-3P-SH molecules not lying flat anymore in this high molecular density. As in the previous section, AFM measurements could disentangle the molecular structure on the MoS_2.

After post-annealing to $\sim -50\,°C$, the majority of molecules – if not all – desorb from the MoS_2 and diffuse to the surrounding Au(111).

Electronically, the molecular dimer shows a slight suppression of the MoS_2 Γ_1 peak at the band gap edge at 0.9 V (see Ch. 2.3.2) in $\mathrm{d}I/\mathrm{d}V$ spectra as shown in Fig. 4.14, but no other features in the 1 V to -1 V bias range. It is likely that this is directly in the HOMO-LUMO gap of the molecule (see Fig. 4.2). Higher energies could not be probed because of the aforementioned mobility of the molecules on the MoS_2 surface.

To combat this mobility and probe CF_3-3P-SH molecules on MoS_2 in a more stable manner, we will investigate a preparation with additional S-vacancies in the next section.

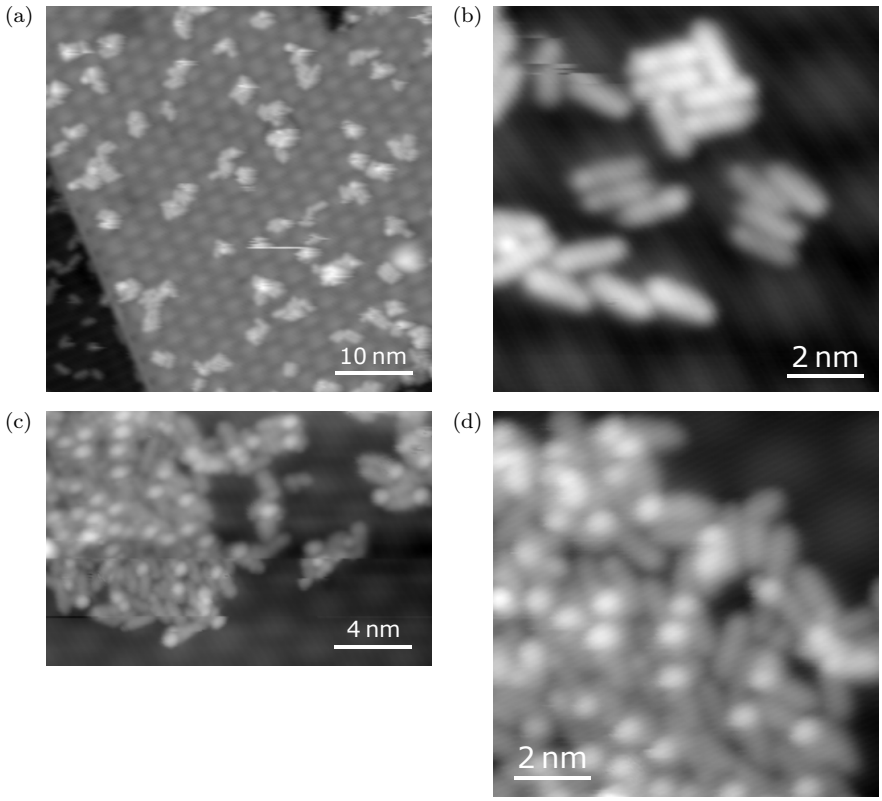

Figure 4.12: STM topographies of CF_3-3P-SH molecules on MoS_2/Au(111) after different evaporation conditions: (a) $T_{\text{sample}} < -150\,^{\circ}\text{C}$, $T_{\text{evap}} = 80\,^{\circ}\text{C}$, $t = 5\,\text{min}$: The CF_3-3P-SH molecules are mostly evenly distributed on the MoS_2 in small clusters, which are mobile when probed with the STM tip as visible by the dragging lines in the image (setpoint: 1 V, 12 pA).
(b) Same preparation as in (a), detailed view. Molecules form small clusters with some ordering visible (setpoints: 1 V, 30 pA).
(c) $T_{\text{sample}} = -120\,^{\circ}\text{C}$, $T_{\text{evap}} = 80\,^{\circ}\text{C}$, $t = 10\,\text{min}$: Big unordered molecular cluster of CF_3-3P-SH on MoS_2/Au(111) (setpoint: 1 V, 20 pA).
(d) Same preparation as (c), detailed view. Individual molecules are difficult to distinguish, but appear with bright protrusions on one end (setpoints: 1 V, 20 pA).

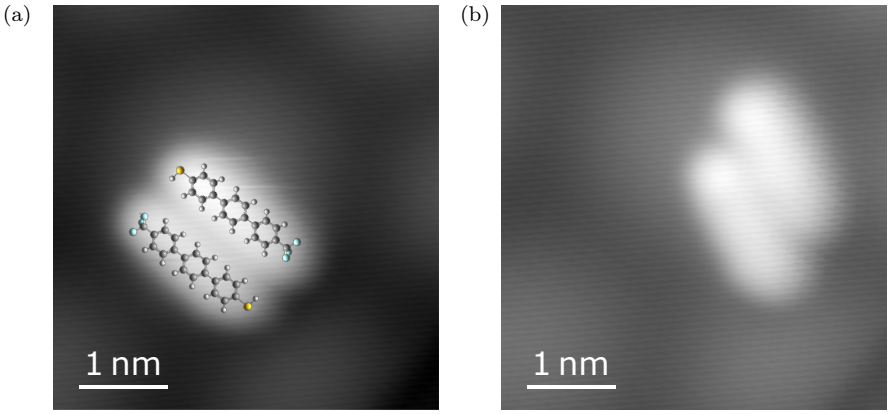

Figure 4.13: STM topographies of a CF_3-3P-SH dimer on MoS_2/Au(111), (a) before and (b) after sweeping the bias from −1 V to 2 V. The dimer moves laterally on the MoS_2, and while the molecules stay together, their relative alignment changes slightly. The molecular model in (a) is placed with an arbitrary orientation of the endgroups. Other relative orientations are equally likely (setpoints: 1 V, 20 pA).

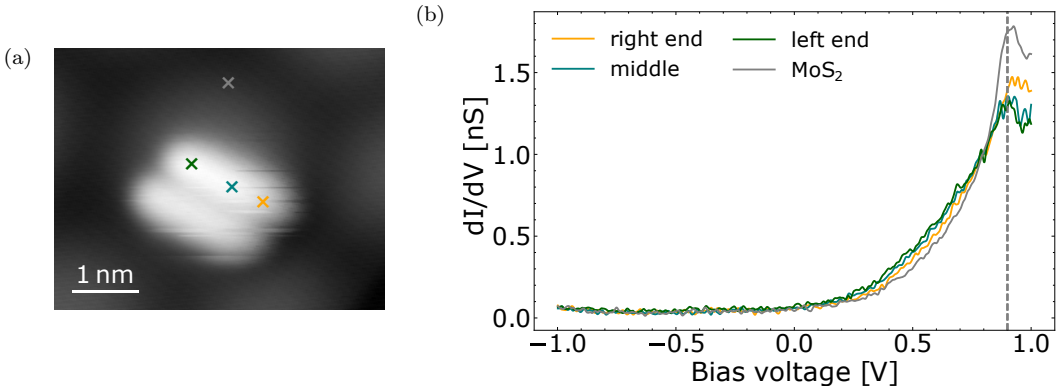

Figure 4.14: (a) STM topography of a CF_3-3P-SH-dimer on MoS_2/Au(111) (setpoint: 1 V, 20 pA). (b) dI/dV spectrum recorded on one of the molecules, positions marked by coloured crosses in (a). No molecular feature is visible in this energy range, only a slight suppression of the Γ_1 peak of the MoS_2 substrate at 0.9 V (grey dashed line) (feedback opened at 1 V, 540 pA).

4.4 Chemisorption of CF_3-3P-S(H) on MoS_2/Au(111)

If additional S-vacancies have been created in MoS_2 prior to molecular deposition, a few single molecules remain on the MoS_2 after post-annealing. Their appearance is at first glance not different than before, but these molecules show a peculiar behaviour upon closer inspection. One such molecule is shown in Fig. 4.15: it is not mobile as observed before on MoS_2/Au(111), but can instead rotate around one of its terminations upon interaction with the STM tip. The green dot in Fig. 4.15 indicates the centre of rotation. In none of the cases did these rotating molecules move laterally and would break rather than move away from the anchoring point, leaving a round residue behind (see Fig. 4.16). We thus conclude that these molecules are anchored to a defect site, with the S vacancy in the top sulphur layer of MoS_2 being the most likely, as this behaviour of anchoring was not observed prior to the deliberate creation of these defects. The robustness of the molecules' anchoring suggests that some CF_3-3P-SH molecules are supplied with enough energy during our preparation procedure to form a strong covalent bond to the S vacancies.

To understand this chemisorption scenario on an atomistic level, D. Maksimov and M. Rossi conducted an exhaustive *ab initio* random structure search, with multiple optimised structures of CF_3-3P-SH, dehydrogenated CF_3-3P-S and 3P-SH that were put into contact with neutral and negatively charged S-vacancies in freestanding MoS_2. The neutral vacancy has to be considered as well, because even though at our measurement temperature of 4 K all of the defects are negatively charged, the temperature during molecular deposition is much higher at 220 K. Since the neutral state and charged state are only 43 meV apart in energy [57], the Boltzmann factor gives us a probability of 10 % for a defect to be in a neutral state at our reaction temperature. It is therefore possible for a CF_3-3P-S(H) molecule to come into contact with a neutral defect. While for negative vacancies, only CF_3-3P-S anchors, both CF_3-3P-SH and CF_3-3P-S can anchor at a neutral vacancy. In all cases, the thiol-group interacts with the defect, not the CF_3-group.

This is corroborated by comparative measurements performed with the molecule 3P-SH which is CF_3-3P-SH with the trifluoromethyl-endgroup replaced by a single hydrogen atom. These molecules show the same behaviour of anchoring on one termination under similar preparation conditions. It is therefore likely that these 3P-SH molecules undergo a similar anchoring process.

Analysing the results from the structure searches, M. Rossi and D. Maksimov find that the CF_3-3P-S(H) molecules anchored such display multiple possible bonding angles with respect to the surface and also different internal torsional angles. While these simulations energetically favour upright-standing configurations for CF_3-3P-S and tilt angles of 15° for CF_3-3P-SH conformers, other conformers are close in energy. Additionally, entropy considerations make flat-lying molecules more likely, as confirmed by exploratory molecular-dynamics simulations.

At this point we also have to consider the general stability of the hybrid state formed by anchoring a molecule to a defect: The interaction with the electronic reservoir of the Au(111) is the determining factor for the local charge state which in turn is independent of the initial charge state of the vacancy before anchoring the molecule. Calculating the

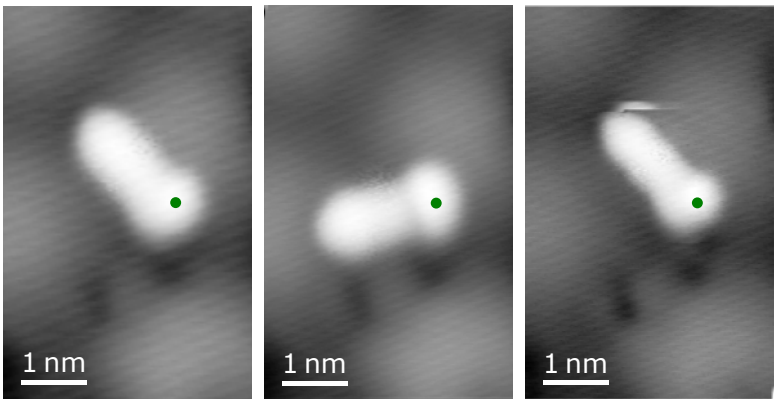

Figure 4.15: STM topographies of subsequent rotation steps of a CF_3-3P-S molecule on MoS_2/Au(111) around its anchoring point (marked by green dot) after interaction with the STM tip (setpoints: a) & c) 1 V, 40 pA, b) 1 V, 50 pA).

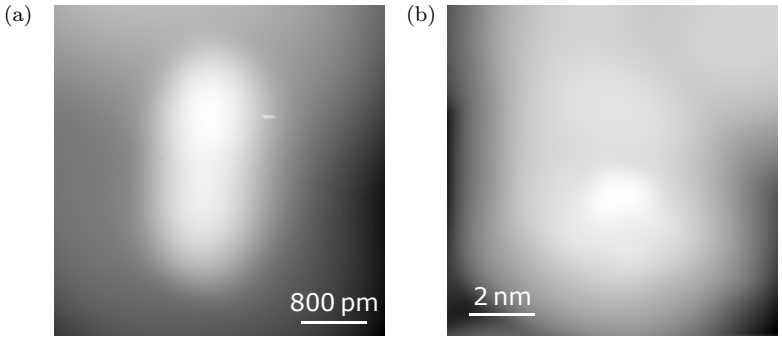

Figure 4.16: STM topography of (a) a CF_3-3P-S molecule anchored on MoS_2/Au(111) and (b) of the round residue left by the molecule from (a) (setpoints: 2 V, 30 pA).

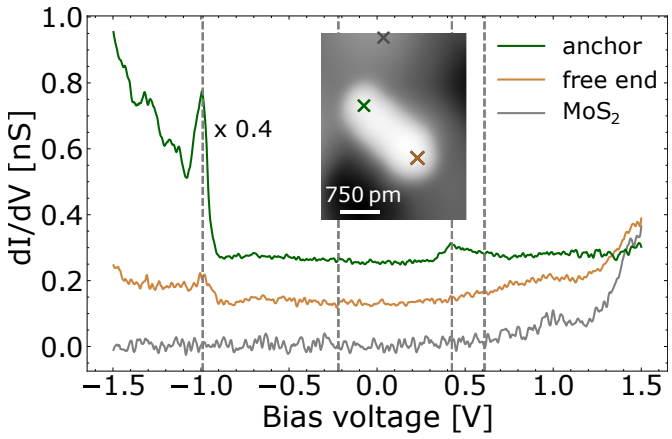

Figure 4.17: dI/dV spectra on an anchored CF_3-3P-SH molecule on MoS_2/Au(111), on the anchor point (green), the free end (orange) and the reference taken on bare MoS_2 (grey). The spectra are vertically offset by 0.125 nS from each other. The spectrum on the anchored site has been rescaled by a factor of 0.4 for better comparison with the other spectra. The grey dashed lines denote the bias values of the dI/dV maps taken in Fig. 4.18 (feedback opened at 1.5 V, 100 pA, lock-in parameters: 2 mV (MoS_2 and anchor) and 5 mV (free end) modulation amplitude). Inset: STM topography of the measured molecule, with colored crosses marking the positions where the spectra are recorded (setpoint: 2 V, 30 pA).

binding energies shows that even the most favourable negatively charged hybrid system is on the verge of stability which means that a neutral system is the most likely result of the anchoring process.

To investigate the electronic properties of the hybrid CF_3-3P-S(H)/MoS_2 system in more detail, we record dI/dV spectra on the anchored molecules. Here, we discover that there are two different types of molecules that are identical in their topographical appearance and rotational behaviour, but differ in their electronic structure. We will explore both in detail in the following two sections.

4.4.1 CF_3-3P-SH anchored to a neutral S vacancy

The majority of anchored CF_3-3P-S(H) molecules ($\approx 80\,\%$) shows a dI/dV spectrum as shown in Fig. 4.17, with the spectrum on the pristine MoS_2 in grey. The conductance of MoS_2 is as expected and already explained in Chapter 2.3.2: essentially flat over a large bias voltage range that indicates the semiconducting bandgap, with the onset of the conduction band smeared out while exhibiting a small peak at ~ 0.9 eV, followed by a stronger one at ~ 1.4 V.

The anchored CF_3-3P-SH molecules, on the other hand, show two main features inside the bandgap of MoS_2: A positive ion resonance (PIR) of high intensity at ~ -1 V with satellite peaks following behind, and a broader negative ion resonance (NIR) with its onset at ~ 420 mV. Both states show a high intensity at the anchored end (green spectrum), and nearly no intensity on the free end of the molecule (orange spectrum).

To investigate these in-gap states further, we record dI/dV maps on the energies of the resonances as marked in Fig. 4.17 by the gray dashed lines. The resulting dI/dV maps

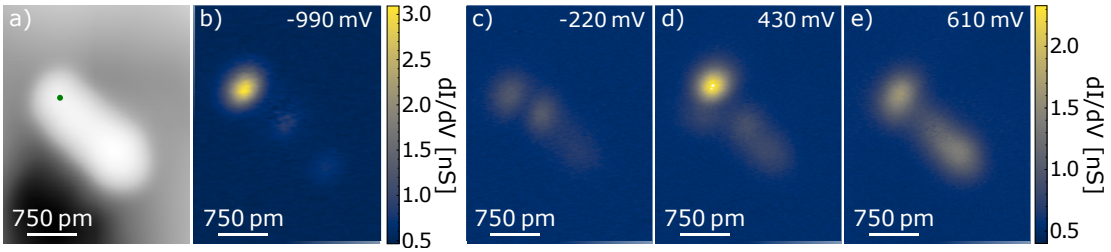

Figure 4.18: a) STM topography (setpoint: 2 V, 30 pA) and constant height dI/dV maps of an anchored CF_3-3P-SH molecule (anchor point marked by green dot) taken at energies marked by grey lines in Fig. 4.17: b) −990 mV, c) −220 mV, d) 430 mV, e) 610 mV (feedback opened at b) −990 mV, 30 pA over anchored end, c)-e) 610 mV, 30 pA above free end, lock-in parameters for all: 5 mV modulation amplitude).

are presented in Fig. 4.18 with the corresponding STM topography. At −990 mV – the energy of the PIR – the map in Fig. 4.18b shows a strong localisation at the anchoring point, with some faint intensity that is spread over the molecular backbone and shows two nodal planes. The NIR at ∼ 430 mV shows the largest contribution close to the anchoring site as well, but slightly offset from the molecular axis in almost a 'walking cane' or 'question mark' shape (Fig. 4.18d). The maps recorded at low (-220 meV, Fig. 4.18c) and higher energy (610 meV, Fig. 4.18e) show a faint structure along the molecule with some intramolecular modulation.

As mentioned in the previous section, many different possible rotational conformations with different tilt angles are possible according to the molecular dynamics calculations which in turn lead to a plethora of states close in energy. This can be observed in experiment as well: The peak positions of both the PIR and NIR shift slightly in energy for different molecules, independently from each other. The energy range the peaks can encompass is illustrated by the gray shaded areas in Fig. 4.19. Additionally to the multitude of different conformations, the energetical modulation caused by the moiré pattern [45] (e. g. position of the anchor point and position of the remaining molecule on the moiré) is also likely to influence the electronic structure of the molecules.

To understand the origin of the observed states, the electronic signature of a subset of the anchored molecular configurations that were found by the aforementioned structure search was calculated using DFT. Fig. 4.20a shows the projected density of states (PDoS) of the CF_3-3P-SH molecule anchored to a neutral S-vacancy. It has to be kept in mind that this calculation does not include the Au(111) surface underneath the MoS_2, so that no quantitative agreement in the energy-level alignment should be expected. The PDoS is separated into the contributions of the MoS_2 (red) and of the CF_3-3P-S molecule (cyan). The semiconducting bandgap can clearly be seen, as well as a sharp, localised in-gap state, which is fully (doubly) occupied and localised at the anchoring point of the molecule as visible in Figs. 4.20b. Another molecular state is visible at the CBM edge, which is also mainly localised around the anchoring point (see Fig. 4.20c). Both states are 1.3 eV apart from each other, which matches the energy difference between the experimentally observed PIR and NIR.

The full occupancy of the defect state also explains the disappearance of the Kondo resonance visible on the bare defects (see Ch. 2.3.2) upon molecular anchoring. This

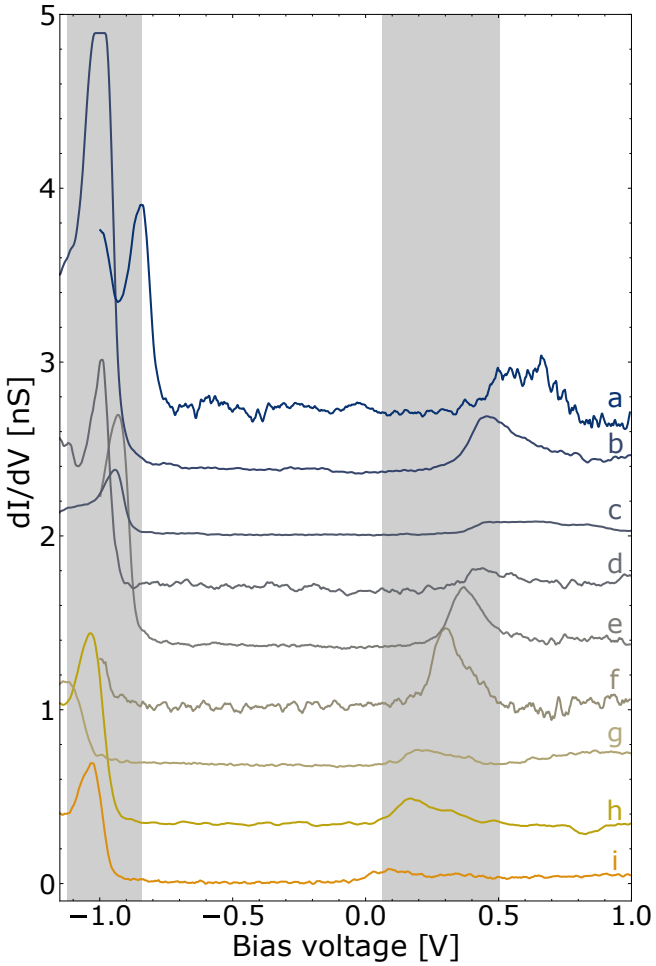

Figure 4.19: dI/dV spectra of nine different anchored CF_3-3P-SH molecules taken on the anchoring point, vertically offset by 0.3 nS from each other for better visibility and sorted by energy of the onset of the NIR. The two main spectroscopic features (PIR and NIR) shift in energy, independently from each other. The grey shaded areas denote the range of this shift: For the PIR on the left the energetical position of the peak maximum is taken as the reference point, and for the NIR on the right the onset of the peaks. (Setpoints from top to bottom: Feedback opened at a) 1 V, 100 pA, b) 2 V, 400 pA, c) 2 V, 100 pA, d) 1.5 V, 100 pA, e) 1 V, 100 pA, f) 1 V, 100 pA, g) 1.5 V, 100 pA, h) 2V 100 pA, i) 1.5 V, 100 pA, and 2 mV modulation amplitude for a, d and f, 5 mV for b, e, g, h, i, and 10 mV for c.)

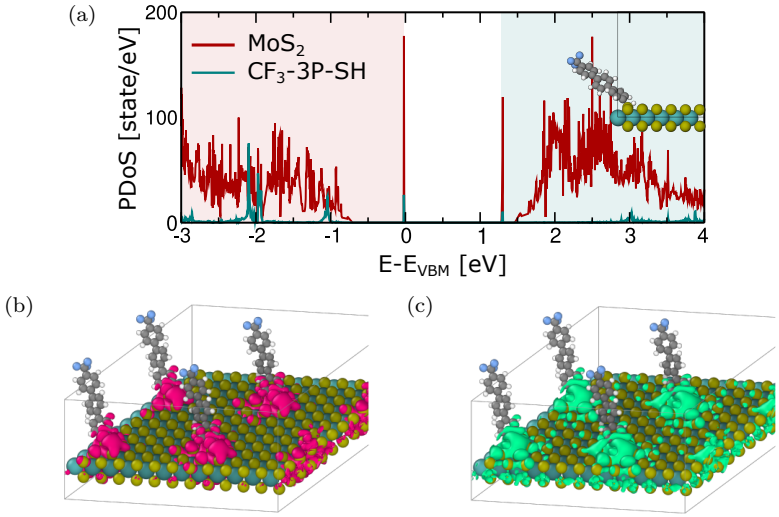

Figure 4.20: (a) Projected electronic density of states (PDoS) of the CF_3-3P-SH structure anchored to a neutral S-vacancy on the MoS_2, shown in the inset, obtained with DFT. Red and cyan lines represent the PDoS on MoS_2 and on the molecule, respectively. The red shaded area marks occupied states and the blue shaded areas marks unoccupied states. (b) Spatial distribution of the highest doubly-occupied state visualised in pink and (c) the lowest unoccupied state in green.

can also be understood by considering that the negative charge of the S-vacancy is responsible for localising the spin that causes the Kondo resonance. For a CF_3-3P-SH molecule to anchor, on the other hand, the vacancy needs to be transiently neutral, i. e. without a localised charge. The resulting system is therefore neutral as well, with new defect states inside the semiconducting gap.

We now turn our attention to the small percentage of anchored CF_3-3P-S(H) molecules that deviate in their $\mathrm{d}I/\mathrm{d}V$ spectra from the ones discussed in this section.

4.4.2 CF_3-3P-S anchored to an initially negatively charged S vacancy

A small percentage ($\approx 20\,\%$) of anchored CF_3-3P-S(H) molecules show a different electronic signature in their $\mathrm{d}I/\mathrm{d}V$ spectra as the ones shown in the previous section, while retaining the topographical characteristics. Fig. 4.21 shows the rotation of such a molecule, with its electronic signature in Fig. 4.22. In contrast to the molecules described before, these molecules exhibit an additional narrow resonance at zero bias, with satellite peaks to both sides, not unlike the Kondo resonance found at the bare S-vacancies as shown in Ch. 2.3.2. The satellite peaks are most likely the result of a vibronic coupling [150]. While we tentatively identify this zero-bias peak (ZBP) as a Kondo resonance, more measurements such as a $\boldsymbol{B}$-field or temperature dependence need to be performed to show that the observed ZBP is indeed a Kondo resonance.

The spatial distribution of these features is recorded via constant-height $\mathrm{d}I/\mathrm{d}V$ maps in Fig. 4.23 at the energies marked by the gray dashed lines in Fig. 4.22. The maps recorded at the energies inside the semiconducting gap ($-110\,\mathrm{mV}$ in Fig. 4.23b, $3\,\mathrm{mV}$ in

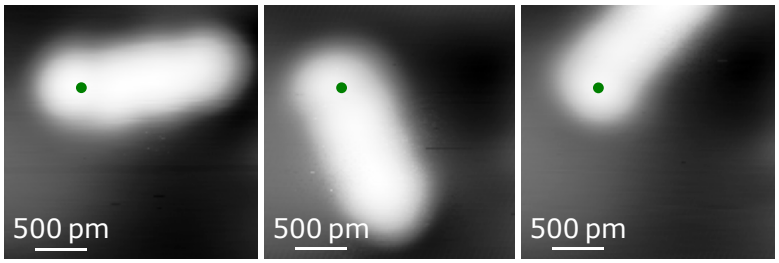

Figure 4.21: STM topographies of subsequent rotation steps of a CF_3-3P-S molecule on MoS_2/Au(111) around its anchoring point (marked by green dot) after interaction with the STM tip (setpoint: 1.3 V, 30 pA).

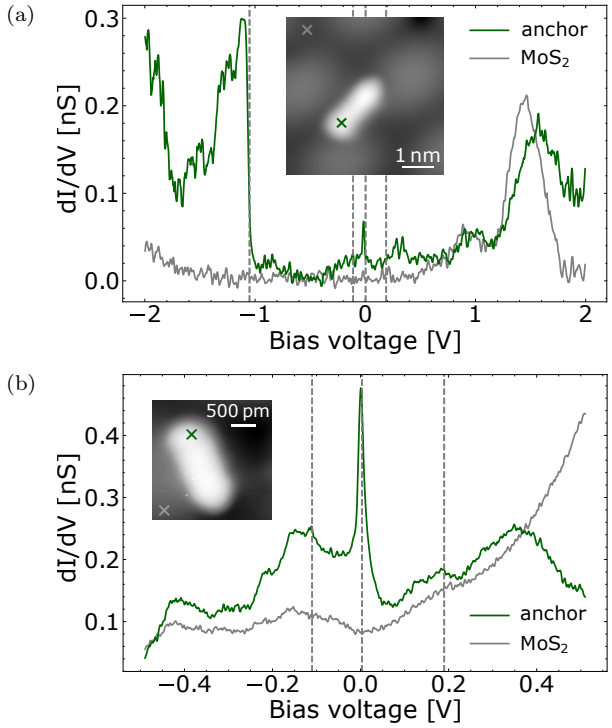

Figure 4.22: dI/dV spectra on an anchored CF_3-3P-S molecule on MoS_2/Au(111), on the anchor point (green) and the reference taken on bare MoS_2 (grey). The grey dashed lines denote the bias values of the dI/dV maps taken in Fig. 4.23 (feedback opened at (a) 2 V, 100 pA, lock-in parameters: 2.5 mV modulation amplitude, (b) 500 mV, 100 pA, lock-in parameters: 5 mV modulation amplitude). Insets: STM topography of the measured molecule, with colored crosses marking the positions where the spectra are taken (setpoint: (a) 1.1 V, 30 pA, (b) 1.3 V, 30 pA).

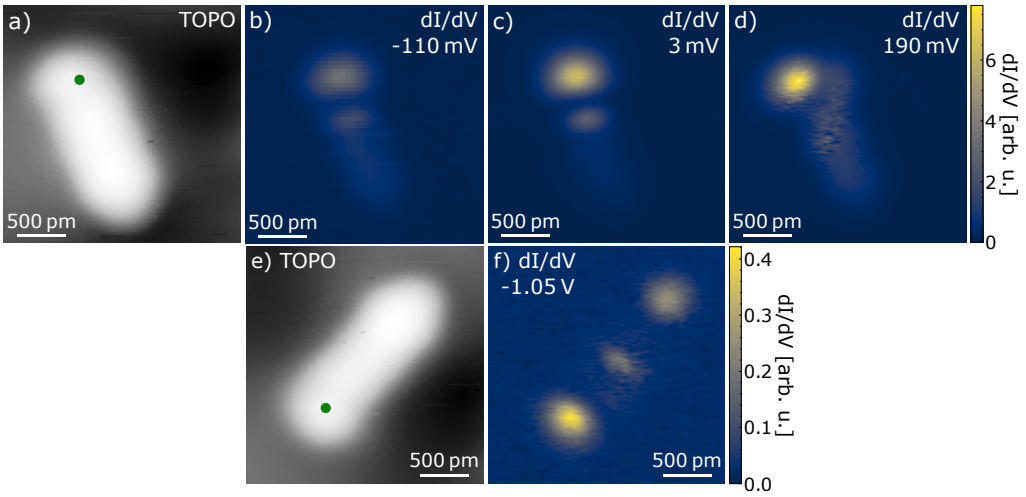

Figure 4.23: (a) STM topography (setpoint: 1.3 V, 30 pA) and constant height dI/dV maps of an anchored CF_3-3P-S molecule (anchorpoint marked by green dot) taken at energies marked by grey lines in Fig. 4.22: (b) -110 mV, (c) 3 mV, (d) 190 mV. (e) STM topography of the same molecule after rotation (setpoint: 1.3 V, 30 pA) and constant height dI/dV map taken at (f) -1.05 V (feedback opened at (b)-(d) 500 mV, 100 pA and 100 pm tip approach, (f) 1.3 V, 30 pA and 50 pm tip approach, lock-in parameters for all: 5 mV modulation amplitude).

Fig. 4.23c and 190 mV in Fig. 4.23d) show a strong intensity at the anchoring point and some modulated intensity over the molecular backbone. Here, b and c share the same symmetry, while d displays the 'walking cane' shape similar to the one in Fig. 4.18d in the last section. The map taken at the energy of the PIR (−1.05 V, Fig. 4.23f) is very similar to the one seen in the previous section as well, with the main intensity at the anchoring point and two nodal planes in the intensity spread over the remainder of the molecule.

What is now the difference to the anchored CF_3-3P-SH molecule in the previous section? As the only difference that is accessible to us from an experimental point of view is the electronic signature, we can only speculate as to the origin. The Kondo resonance indicates the existence of an unpaired spin that does not exist in the case of CF_3-3P-SH anchored to a neutral S vacancy. The two immediate possibilities for the creation of an unpaired spin are therefore that either the molecule is dehydrogenated, or that the defect is not neutral. But we also have to keep in mind the stability analysis detailed at the beginning of this section that tells us that the final charge state of the system must be neutral, which is independent of the initial charge state of the vacancy. At the same time, for a dehydrogenated S radical to anchor to a defect, a reaction barrier for the dehydrogenation to happen in the first place has to be overcome [151]. This barrier is proposed to be lower for a negatively charged defect, making this the more likely mechanism.

To explore these possibilities, more molecular dynamics simulations were performed by M. Rossi and D. Maksimov. As already mentioned in the beginning of this chapter, no stable anchoring for CF_3-3P-SH molecules to a negatively charged S vacancy was observed, thereby excluding this mechanism. We therefore consider the CF_3-3P-S radical and a negatively charged vacancy.

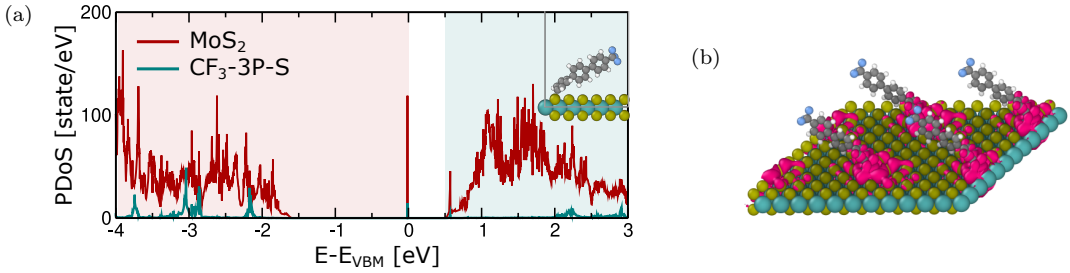

Figure 4.24: (a) Projected electronic density of states (PDoS) of the CF_3-3P-S structure anchored to a neutral S-vacancy on the MoS_2, shown in the inset, obtained with DFT. Red and cyan lines represent the PDoS on MoS_2 and on the molecule, respectively. The red shaded area marks occupied states and the blue shaded areas marks unoccupied states. (b) Spatial distribution of the singly occupied in-gap state visualised in pink.

The anchoring mechanism is proposed to be the following: when the CF_3-3P-SH molecule is in the vicinity of the negatively charged vacancy, the H is catalytically dissociated from the SH-group. The CF_3-3P-S radical binds with its dangling bond to the defect and the remaining H diffuses away. The interaction with the Au's charge reservoir drains the additional charge away, resulting in a neutral system with a single localised electron. Since this process is energetically not favourable compared to the one described in the previous section, its occurrence is less likely. This is in accordance with our experimental observations.

The calculated PDoS of the CF_3-3P-S molecule anchored to the neutral MoS_2 is shown in Fig. 4.24a. Similar to the PDoS of the CF_3-3P-SH molecule, we see an in-gap state, but in contrast to the previous one, this one is singly-occupied and can thus give rise to a Kondo resonance. Combined with its localisation at the anchoring point, as visible in Fig. 4.24b, this is in good agreement with experiment.

To further strengthen the case of the suggested mechanism, one could exclude other factors that could influence the defects and therefore the resulting hybrid system, such as occupation by rest-gas molecules [152] that could change their charge and spin state. To disentangle these effects experimentally, one possibility would be the deliberate dosing with possible contaminants, to observe how the bare S-defects change their behaviour, and whether a statistically significant number of anchored CF_3-3P-S molecules with a Kondo resonance can be reproduced. Another avenue to pursue could be the exploration of different sulphur-based substrates, where top-layer defects are intrinsically neutral. This could be achieved through either a different S-based TMDC (e. g. WS_2), or by choosing another substrate as a base below the TMDC layer, or both.

4.5 Conclusion

To conclude, in this chapter we have investigated different adsorption scenarios of CF_3-3P-S(H) molecules on Au(111), MoS_2/Au(111) and anchored to S-defects on MoS_2/Au(111).

On Au(111) and MoS_2/Au(111), the CF_3-3P-SH molecules physisorbed to the surfaces, forming different structures depending on the energy provided by the temperature during deposition. The molecules attract each other, forming molecular structures on the surface, with a closer packing with increasing temperature. Extended structures have begun to form at the upper end of the temperature range examined that lead to the assumption that extended regular structures can form under the right conditions.

While there was no strong interaction with the surface observable on MoS_2, CF_3-3P-SH on Au(111) showed some indications of direct bonds to the surface forming at step-edges and molecule-molecule interaction that is also possibly mediated by an Au adatom. But the shift in energy of the observed MO, assigned to the LUMO, and the formation of the double-decker structures indicate that the molecule-molecule interaction dominates.

A chemisorption scenario was observed when additional S-defects were purposefully created in MoS_2/Au(111): the anchoring of CF_3-3P-S(H) molecules to the S defects. In STM/STS, we found two different species that are identical in topographical appearance, but differ in their electronic structure. Using *ab-initio* structure searches and DFT calculations, we found that these two species are intact CF_3-3P-SH and dehydrogenated CF_3-3P-S that are anchored to the S-vacancies, with the hybrid systems showing states in the bandgap of MoS_2. For the anchored, dehydrogenated molecule, this state is singly occupied, resulting in what we have tentatively assigned as a Kondo resonance.

The combination of our experimental methods with the capabilities of *ab-initio* molecular dynamics structure searches allowed us to unravel the mechanism behind the anchoring on an atomic level. While the system investigated is only a 'model' system, it could act as a blueprint for future systems that are more complex in their molecular and electronic structure. For example, the attachment of further molecular groups could enable the selective tuning of energy level alignment to create robust hybrid states with specifically tailored properties. This in turn could be utilised in novel applications in e. g. opto-electronic devices.

5 Effects of the Tip-Perturbation Potential and Vibration-Assisted Tunnelling on VONc on MoS_2/Au(111)

In this chapter we present the measurements conducted on single vanadyl-naphthalocyanine (VONc) molecules on MoS_2/Au(111). The structural model of a VONc molecule in gas-phase is shown in Fig. 5.1: The VONc molecule consists of a naphthalocyanine group which is the 'bigger cousin' of the more well-known phthalocyanine molecule in that on each ligand, four additional CH-groups are attached. In the centre of the naphthalocyanine-complex sits a vanadium atom, stabilised by the four surrounding N-atoms. An O-atom is attached on top of the central V-atom. As shown by K. Kaiser et. al in Ref. [153], the closely related VOPc molecule can adsorb with either the O-atom pointing towards the surface, or away from it. L. Malavolti et. al showed in Ref. [154] the possibility of controllable and variable tilting of the VO bond of VOPc with the STM tip, inducing interaction with the (superconducting) surface in the form of Yu-Shiba-Rusinov (YSR) states. This is likely this case for VONc as well.

The family of (na)phthalocyanines is generally well-known for their stability on surfaces and their variability through different possible molecular centres [155–157], for example allowing for selective spin-tuning [154, 156–159] and energy-level tuning [160, 161] via their metal centres. This molecular family has been intensively studied, showing the

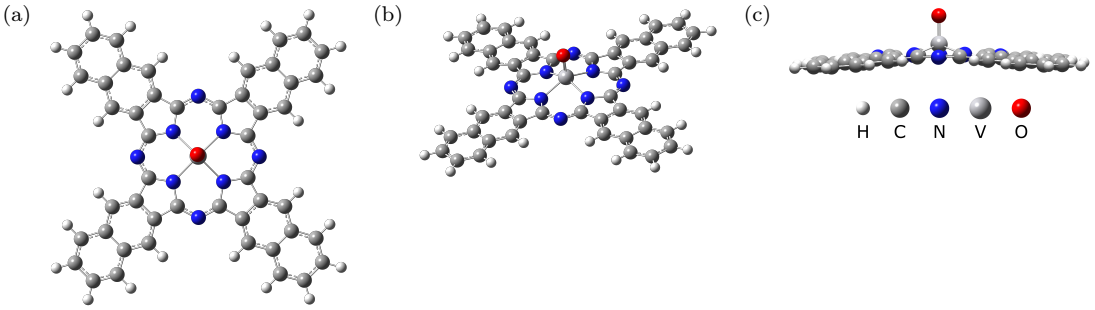

Figure 5.1: Structural model of neutral vanadyl-naphthalocyanine (VONc), (a) top-view, (b) 45°-view and (c) sideview, as calculated in gas-phase using Gaussian16 with the functional B3LYP and the basis set 6-31++g(d,p). The central atom of the molecular complex is a vanadium atom, with an oxygen atom attached on top.

strength of these molecules as model systems to study charge processes [162], utilising them as molecular switches [163, 164], to disentangle the various different effects that can act on the energetical structure of a molecule [98, 165] as well as using them as benchmark systems for new measurement techniques [98, 166]. Because of the high mobility of molecular adsorbates on MoS_2, their stability is instrumental in allowing us to probe single molecules successfully.

Electronically, VONc is predicted to have a small HOMO-LUMO bandgap of 1.8 eV [167], which makes it an interesting candidate for e. g. optical excitation and exploring the opto-electrical properties via light-emission STM. It additionally carries a single unpaired spin in its neutral ground state ($S = \frac{1}{2}$), adding the possibility of spin-based effects such as spin-excitations and making this molecule a possible building block for e. g. spintronic devices.

The additional use of MoS_2/Au(111) as a substrate for these molecules allows for a higher energy resolution of molecular states that are inside the semiconducting bandgap which in turn makes it possible to explore different effects that act on the electronic structure of a molecule, as we will show in this chapter.

5.1 Sample Preparation & Adsorption Properties

The base sample of MoS_2/Au(111) was prepared as described in Ch. 3.2.1 and 3.2.2, resulting in large MoS_2 islands (> 50 nm) as shown in Chapter 3.2.2, Fig. 3.3b. After confirming the successful creation of MoS_2 islands in the STM, the VONc molecules are evaporated onto the sample from a Knudsen cell at 440 °C for 7 min under high vacuum. The sample was cooled down to between -130 °C to -140 °C prior to evaporation and held at that temperature to minimise diffusion away from the MoS_2 of the otherwise mobile molecules. After evaporation, the sample is directly transferred into the STM.

VONc on Au(111) and MoS_2/Au(111) appears in STM topography as a four-leaf clover-like shape; four ligands linked together like a cross around a roundish centre as shown with a molecular model in Fig. 5.2a. From STM topography alone it cannot be determined whether the O-atom points towards or away from the surface.

The majority of VONc molecules are adsorbed on the Au(111), where they are statistically distributed, with the slight tendency to follow the herringbone surface reconstruction, as visible in Fig. 5.2c. There seems to be no preference for neither the hcp nor the fcc regions. Additionally, the evaporation procedure deposits unidentified dirt on the Au(111) surface that could stem from contaminants in the molecular powder. On MoS_2/Au(111), the VONc molecules adsorb as single molecules, with the rare exception of dimer formation as shown in Fig. 5.2b. Also frequently observed on the surface is the presence of circular adsorbates with a diametre of ~ 400 pm. These adsorbates are highly mobile and tend to cluster around the VONc molecules, often moving around the molecule after interaction with the STM tip as visible in Fig. 5.3.

Curiously, the molecular centre of VONc on MoS_2/Au(111) can appear as either more protruding ('bright', Fig. 5.4a), or more depressed ('dark', Fig. 5.4c) than the ligands. At first glance, this seems to correspond to the observation by K. Kaiser et al. that VOPc molecules on NaCl can adsorb with either the O-atom towards or away from the

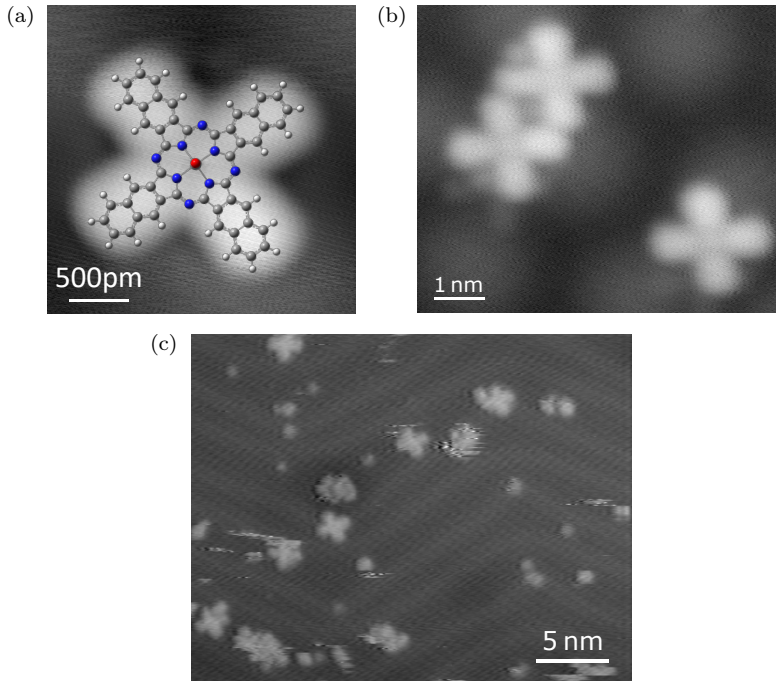

Figure 5.2: STM topographies of VONc molecules. (a) Single VONc molecule adsorbed on MoS_2/Au(111) with molecular model. The molecule appears as a four-leaf clover-like protrusion (setpoint: 10 pA, 500 mV). (b) Single VONc molecule and molecular dimer on MoS_2/Au(111) (setpoint: 20 pA, 500 mV). (c) Overview topography of VONc molecules adsorbed on Au(111). Not only the VONc molecules, but also unidentified contaminants are visible on the surface (setpoint: 50 pA, 1 V).

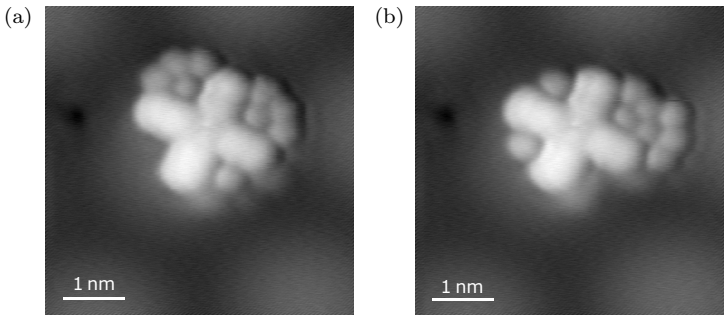

Figure 5.3: STM topography of a single VONc molecule on MoS_2/Au(111) with circular contaminants around it. The contaminants move around the molecule after sweeping the bias voltage over the molecule from 2 V to −2.2 V between (a) and (b) (setpoints: 10 pA, 500 mV).

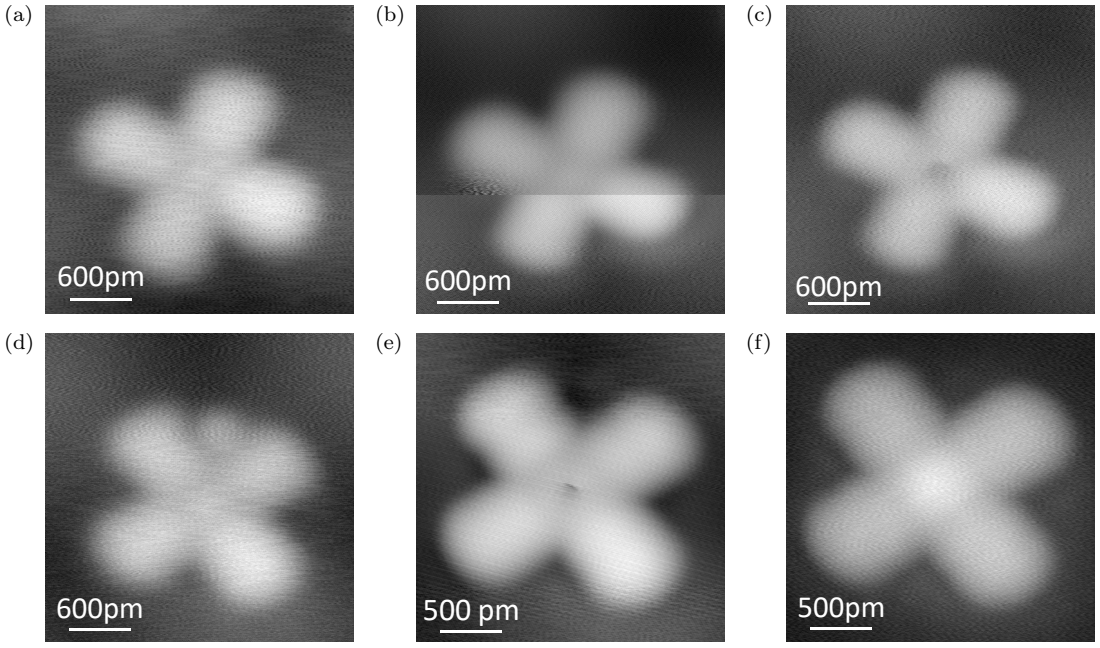

Figure 5.4: A series of subsequent STM topographies of two different VONc molecules on MoS_2/Au(111) with changing apparent height of the molecular centre. (a) The centre appears bright or semi-bright, (b) a tip-change occurs during the topography scan and (c) the centre appears dark. (d) Another VONc molecule has a semi-bright centre, (e) which turns dark after a bias sweep over the molecule from 2 V to −2 V (note that the circular adsorbate also disappears), and (f) turns bright again (with a centre that appears higher than in (d)) after approaching with the tip and sweeping the bias from −2 V to −0.5 V, which causes the molecule to move laterally as well (setpoints: 10 pA, 500 mV).

surface [153]. A closer examination shows however that the appearance of these centres can change during a topography scan, as shown in Fig. 5.4. Since this flip is reversible, it is highly unlikely that the O atom is involved in the change of appearance. While it is entirely possible that the STM tip induces changes in the VO-bond (as shown for VOPc in [154]), it is unlikely that such a change remains stable. The most likely explanation is therefore that an additional adsorbate is placed and removed by the STM tip, possibly the abundant adsorbates visible in Fig. 5.3. To ascertain the cause of these differently appearing centres and the orientation of the VO-bond with respect to the surface, further investigation with e. g. AFM is needed.

5.2 Electronic Structure and Effect of Tip-Perturbation Potential

Electronically, the VONc molecules on MoS_2/Au(111) show a broader state just outside the bandgap of MoS_2 at ~ 1.7 V, and multiple states at negative bias voltages inside the bandgap as visible in the $\mathrm{d}I/\mathrm{d}V$ spectra shown in Fig. 5.5. The conduction band states of MoS_2 at 0.9 V and 1.4 V [91] (grey spectrum in Fig. 5.5) are not visible when over the molecule.

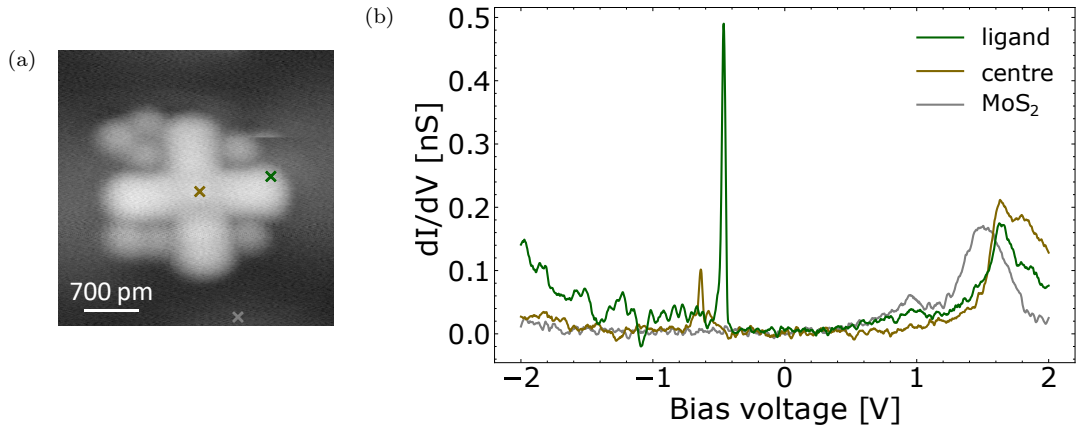

Figure 5.5: (a) STM topography of a VONc molecule on MoS_2/Au(111) (setpoint: 10 pA, 500 mV). (b) dI/dV spectra recorded on the ligand (green), the centre (yellow) and on MoS_2 (grey) at the positions marked with coloured crosses in (a). The ligand shows a very pronounced PIR at ~ -450 mV inside the MoS_2 gap and satellite peaks following behind, while the centre shows a group of peaks with lower intensity at ~ -650 mV. Both spectra show a broad peak outside the MoS_2 gap at ~ 1.7 V (feedback opened at 2 V, 100 pA, 5 mV modulation amplitude).

Depending on the position above the molecule, the in-gap states change in energy and intensity. The ligand shows a sharp peak at around -450 mV with satellite peaks following behind that extend past the onset of the valence band of MoS_2 at -2 V and appear to continue beyond the recorded bias range (green spectrum in Fig. 5.5). The centre, on the other hand, shows a close cluster of peaks at around -650 mV, and only a slight modulation in the signal behind, but no clear satellite peaks, and a smeared out step at around -1.8 V (orange spectrum in Fig. 5.5).

While the peaks inside the MoS_2 gap of ligand and centre seem unrelated at first glance, looking at their spatial evolution across a molecule sheds light on the relation between them. Recording dI/dV spectra along a line running from one ligand to the one opposite across the centre of the molecule (see green arrow in Fig. 5.6a) and plotting them in a stacked colour plot as in Fig. 5.6d and the zoom in Fig. 5.6e reveals that there is an apparent shift in energy of the most pronounced peak: On the ligand, the peak starts at -450 mV, then gradually moves further away from E_F when we move closer to the molecule's centre. On the centre, there appears to be a jump in energy to ~ -650 mV. Looking closely, however, shows that the onset of the peak shifts consistently, only the relative intensity of the cluster of peaks changes. This evolution of lineshapes can be seen even more clearly in the 'waterfall' plots of the same dataset as shown in Figs. 5.6b and 5.6c.

Note that these spectra have been recorded on the same molecule as in in Fig. 5.5 but with the line of spectra taken at a slightly different angle relative to the symmetry axes of the VONc molecule. This leads to a reduced intensity of the elastic peak at the ligands in this data set than in Fig. 5.5 and therefore in turn to a reduced intensity of the satellite peaks.

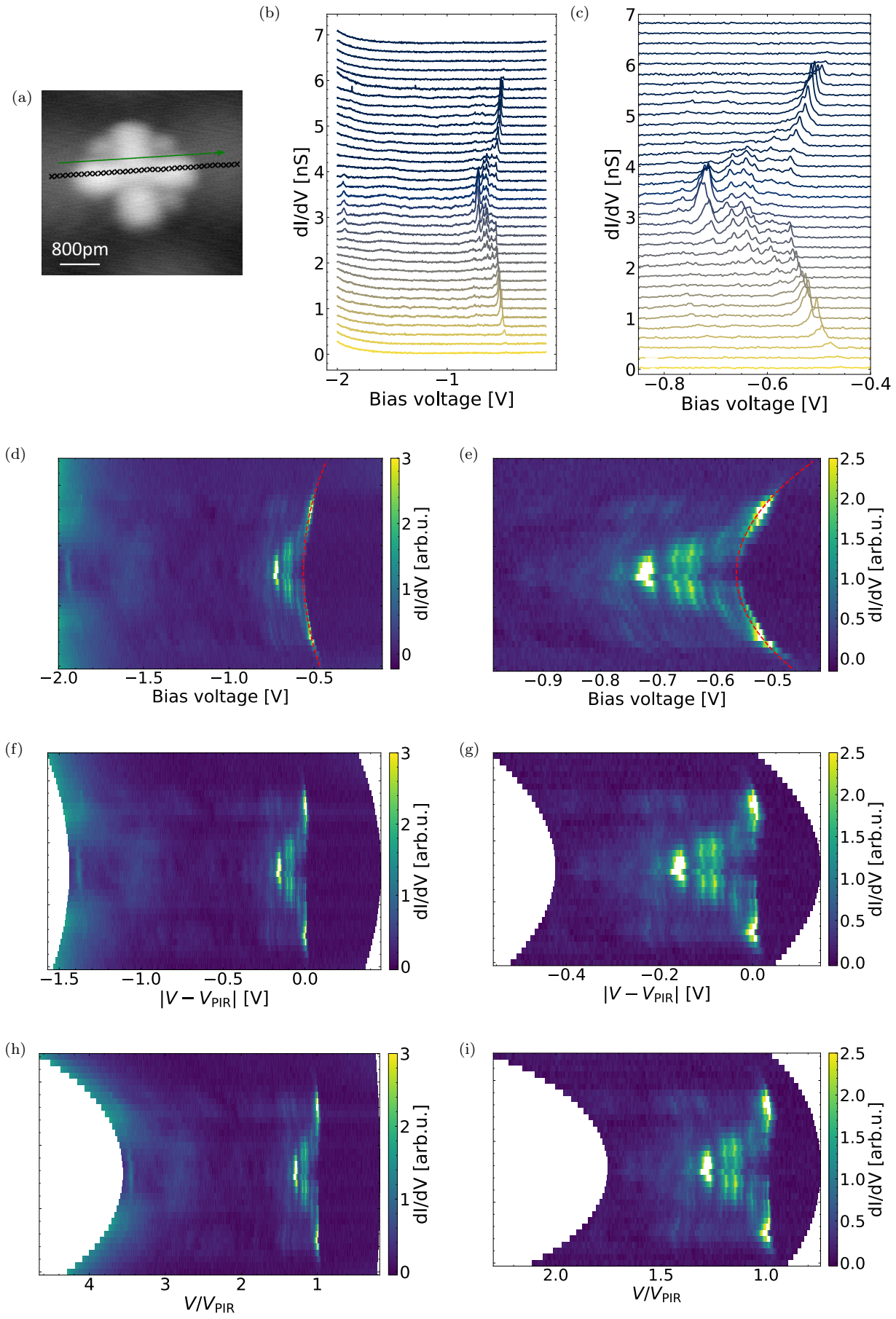

Figure 5.6: dI/dV spectra taken along a line across a single VONc molecule on MoS_2/Au(111). (a) STM topography of the investigated VONc molecule with black crosses indicating the position of the individual spectra (setpoint: 10 pA, 500 mV). (b) Waterfall plot of the recorded dI/dV spectra, vertically offset for better visibility. The bottommost spectrum is the first spectrum along the green arrow in (a). (c) Zoom into the energy range around the PIR, showing the evolution of the lineshape across the molecule. (d), (e) Stacked colour plot of the same dataset. The red dashed line indicates the performed parabolic fit (see Fig. 5.7). The dI/dV spectra are then (f), (g) offset according to the fitted parabola and (h), (i) normalised to the energy of the PIR (feedback opened at −2 V, 100 pA, modulation amplitude of 1.5 mV).

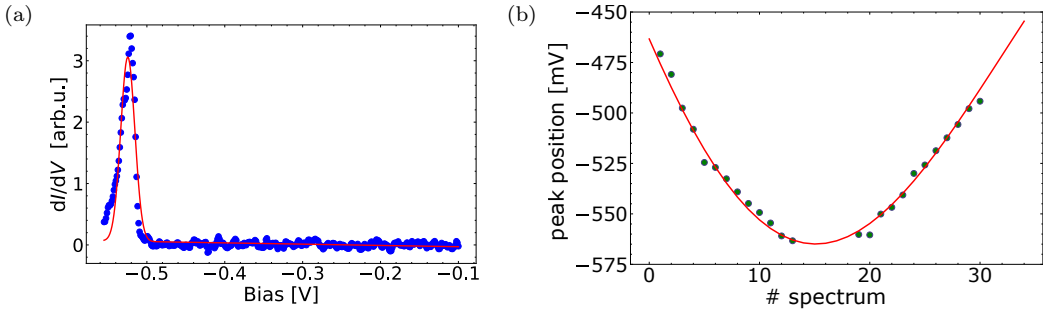

Figure 5.7: (a) Exemplary fit of the PIR of one dI/dV spectrum of Fig. 5.6 with a Gaussian and a linear slope. (b) Peak position of the fitted PIRs extracted from the Gaussians fitted to them (green dots). The distribution is fitted with a parabola and a linear background slope (red line). Note that the dI/dV spectra taken over the middle of the VONc molecule are not included in the fit, as the very low intensity of the PIRs makes them unidentifiable. The number of the spectrum corresponds to the position over the molecule as shown by the black crosses in Fig. 5.6a.

To quantify this shift, we fit a Gaussian lineshape with a linear background to the positive ion resonance (PIR) which is the strongest resonance on the ligand, and almost the faintest close to the centre. One of these fits is shown as way of example in Fig. 5.7a. We then plot the resulting energy of the fitted Gaussian's centre with respect to the position on the molecule which results in a distribution as shown in Fig. 5.7b (green dots) that shows a total shift of about $\sim 80\,\mathrm{mV}$.

What is now the origin of this shift? As described in Chapter 2.5, a molecular state appears to shift in energy when moving across the molecule because of the interaction with the tip perturbation potential. To quantify this interaction, we fit a parabola with a linear background to the obtained distribution. We choose a parabolic shape as a second-order approximation for the shift caused by the electrostatic potential of a tip approximated by a point-charge (see Eq. (2.31) in Ch. 2.5). This parabola leads to passable results (red line in Fig. 5.7b). Note that the centre has been excluded from the fit as the PIR becomes nearly unidentifiable.

The parabolic shift obtained thus is now applied to the colourplots of Fig. 5.6 (red dashed line in Figs. 5.6d and 5.6e): First, we shift each spectrum to the peak energy of the PIR V_{PIR} in Figs. 5.6f and 5.6g. It can be seen that the elastic peak is – as expected – now almost a straight line. We see a slight shift on the lower part, which could be a small tip change, and still a slight curvature in the upper part of the PIR, which could point to a higher order effect. It can also be seen, especially in the zoom of Fig. 5.6g, that the peaks following close after the PIR now also appear to be straight lines, while further away a slight curvature remains, although the very low intensity of the centre makes a conclusive identification difficult. The peaks gaining in intensity on the centre of the molecule now appear straight as well.

To gain insight into the character of the tip, which also influences the nature of the shift, we additionally explore normalising to the PIR energy in Figs. 5.6h and 5.6i. At first glance, there are barely any differences to the shifting. Upon closer inspection, however, it can be seen that the curvature becomes stronger when moving further from the PIR.

This suggests that there is a slight dipolar component to our tip, as a tip without dipole should show only straight lines across the whole energy range when normalising, since the tip-perturbation potential cancels itself out and only the dipole component remains (see Ref. [91] for details). While a dipole is quite common for metal tips [168–171] due to the Smoluchowksi effect [172] 'smearing out' the electric configuration, it is also very dependent on the tip geometry and atomic configuration of the tip apex. Additionally, it is possible that in our system a contaminant with a dipole might have been transferred to the tip unintentionally.

While we have now explored the effects of the tip-perturbation potential on our VONc molecule and therefore understood the shift in energy of the PIR when moving across the molecule, the apparent 'jump' in energy when over the centre of the molecule and the severe changes in lineshape cannot be explained by the tip-perturbation potential. This can be seen even more clearly when plotting the same dataset as in Fig. 5.6 in a waterfall plot as shown in Fig. 5.6b and 5.6c. Especially in the zoom of Fig. 5.6c, the changing lineshapes when moving across the molecule can very clearly be seen.

To understand the changing intensities and lineshapes and what the underlying cause is, we first have to investigate the molecular orbitals (MOs) that give rise to the resonances we see in the $\mathrm{d}I/\mathrm{d}V$ spectra.

5.3 Molecular Orbitals

To identify the molecular orbitals (MOs) visible as resonances in our $\mathrm{d}I/\mathrm{d}V$ spectra, we have to investigate their spatial distribution. This can be achieved by both looking at the appearance of the molecules in STM topography at different bias voltages and by recording $\mathrm{d}I/\mathrm{d}V$ maps, as introduced in Chapter 2.2.

Fig. 5.8 shows some bias-dependent STM topographies. It can clearly be seen that the appearance of the molecular lobes changes with the applied bias voltage: In the negative bias range (Figs. 5.8a to 5.8c), the lobes appear as four protrusions separated by nodal planes with two perpendicular mirror planes (see green dashed lines in Fig. 5.8c). Around the molecular centre is a ring with four-fold symmetry, while the centre itself appears dark at $-670\,\mathrm{mV}$ (Fig. 5.8c) and bright at $-720\,\mathrm{mV}$ (Fig. 5.8b). At even higher negative biases of $-1.85\,\mathrm{V}$ a supermodulation begins to distort the mirror symmetry, most pronounced on the top and bottom lobes (Fig. 5.8a).

At positive biases of 500 mV (Fig. 5.8d), the molecule appears as a mostly homogeneous protrusion, without the internal modulation visible at the negative biases. At higher positive biases of 1.55 V (Fig. 5.8e), the molecular centre appears with a higher apparent height than the ligands.

Fig. 5.9 shows the constant height $\mathrm{d}I/\mathrm{d}V$ maps recorded over another VONc molecule. At first glance, there are not many similarities to the bias-dependent topographies: From $-610\,\mathrm{mV}$ to $-470\,\mathrm{mV}$, the spatial distribution of the $\mathrm{d}I/\mathrm{d}V$ signal undergoes a curious evolution: At $-610\,\mathrm{mV}$, we see a 'squished' ring at the molecular centre with two very faint nodal planes. When moving closer to E_F, this ring seems to expand outwards and develop an internal structure that starts to stretch into the ligands. The centre is surrounded by a four-fold symmetric ring. This ring 'smears' out slightly at $-520\,\mathrm{mV}$,

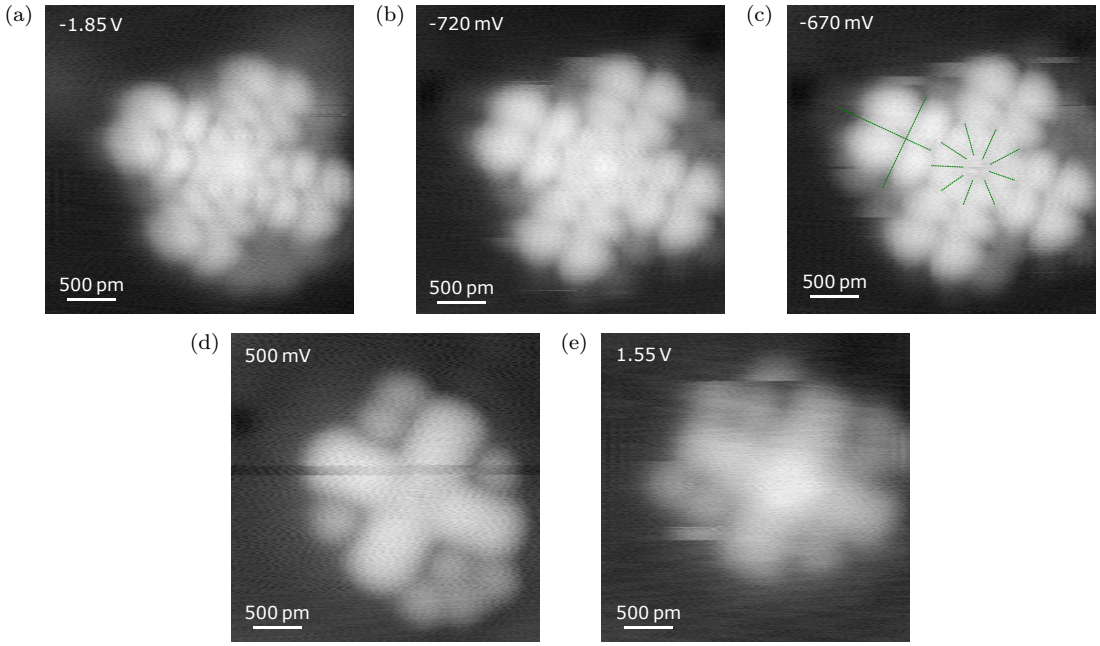

Figure 5.8: STM topographies of a single VONc molecule on MoS_2/Au(111) taken at different bias voltages: (a) −1.85 V, (b) −720 mV, (c) −670 mV, (d) 500 mV and (e) 1.55 V (current setpoints: 10 pA). The green dashed lines indicate the nodal planes described in the main text.

before the $\mathrm{d}I/\mathrm{d}V$ signal moves from the centre to the ligands entirely at −490 mV. Here, we also see a circular arrangement of features retaining their four-fold symmetry. This continues to move outward at −470 mV, before the signal disappears at −450 mV.

To identify the molecular states, we simulate the molecular orbitals (MOs) of the VONc molecule in gas-phase in its doublet ground state ($S = \frac{1}{2}$) using Gaussian16 [145] and the basis set B3LYP and functional 6-31++g(d,p). The resulting MOs are then used to simulate the STM $\mathrm{d}I/\mathrm{d}V$ maps.

The resulting MOs are shown in Fig. 5.10 with their corresponding energies. This calculation yields a HOMO-LUMO gap of 1.8 V, which is in accordance with values reported in literature [167]. Around E_F, both spin channels are nearly identical in both energy and appearance, and the MOs are therefore doubly occupied. The single spin of VONc sits further away from E_F, in HOMO-4 of the α-channel.

To compare to experiment, we simulate $\mathrm{d}I/\mathrm{d}V$ maps from these MOs using the Tersoff-Hamann model of STM (see Ch. 2.1) in Fig. 5.11. It is immediately apparent that the simulated $\mathrm{d}I/\mathrm{d}V$ map of the HOMO (Fig. 5.11b) matches the symmetries seen in the STM topography recorded at −670 mV, −720 mV and, to an extend, at −1.85 V: Four almost exactly mirror-symmetric protrusions on the ligands with a four-fold symmetric ring around the molecular centre. The topography recorded at 1.55 V matches the because of their degeneracy combined LUMO and LUMO+1 maps, with the main intensity in the centre.

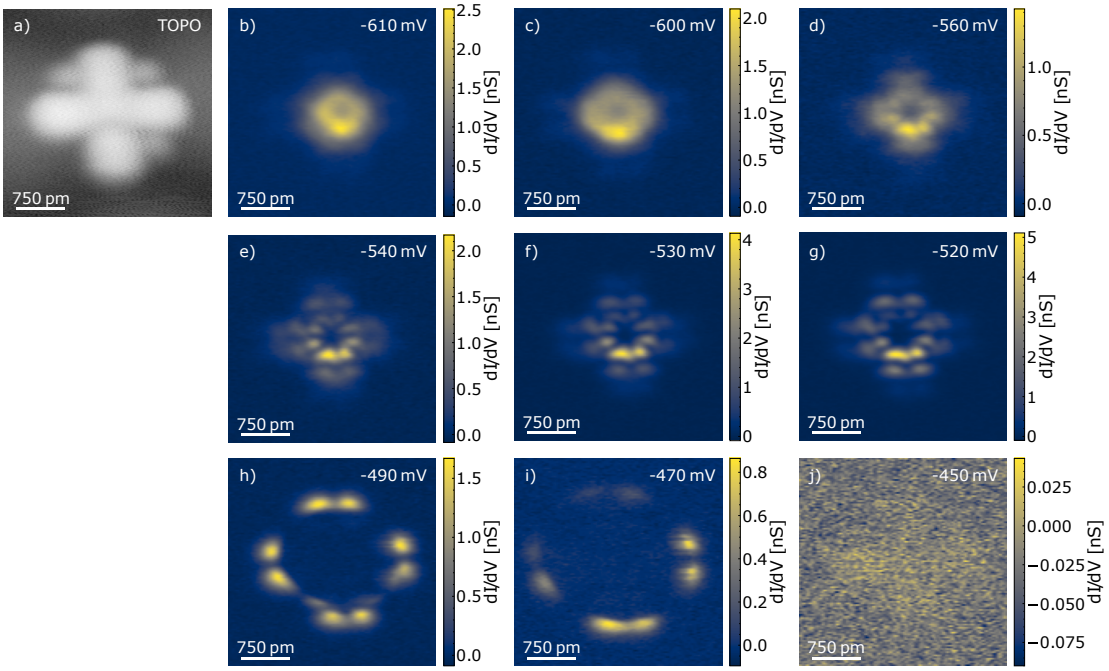

Figure 5.9: (a) STM topography and (b)–(j) $\mathrm{d}I/\mathrm{d}V$ maps taken on a single VONc molecule on MoS_2/Au(111) at different energies (setpoints: 10 pA for all, (a) 500 mV, (b) – (j) −610 mV and 5 mV modulation amplitude).

Peculiarly, this identification is not immediately possible in the recorded $\mathrm{d}I/\mathrm{d}V$ maps. While maps with their intensity around the centre (especially those at −540 mV, −530 mV and −520 mV) exhibit the four-fold ring, they have no intensity at the ligands. Conversely, the maps taken at −490 mV and −470 mV show partially the symmetry of the HOMO in the ligands, but no intensity in the middle.

While puzzling at first, the first clue of this riddle can be found by recalling the findings of the last section: the tip-perturbation potential affects an apparent shift of $\sim$ 80 mV in energy of the molecular states when moving across the VONc molecule. While some open questions remain and will be addressed in the next section, we can already conclude from this that a map at a single energy with a modulation amplitude of 5 mV can therefore not capture the full spatial extend of this moving state and we need to consider the $\mathrm{d}I/\mathrm{d}V$ maps from −610 mV to −470 mV not individually, but together. The bias-dependent topography, on the other hand, is the result of all states below the chosen setpoint and therefore shows a 'summation' over the states.

However, the shift caused by the tip-perturbation potential alone is not sufficient to reconcile experiment and simulation fully: The range needed to compile a full image exceeds the shift of 80 mV. But we can quickly recall that the peaks did not only shift in energy, but also changed in regard to their lineshape and intensity. While only a single peak was visible on the ligands, a whole cluster of peaks appeared on the centre. Since there are no molecular states this close in energy, we have to consider another origin: vibration-assisted tunnelling (VAT). As explained in Ch. 2.6, VAT takes the influence the vibrational modes have on the spatial geometry of the MOs and thereby on the

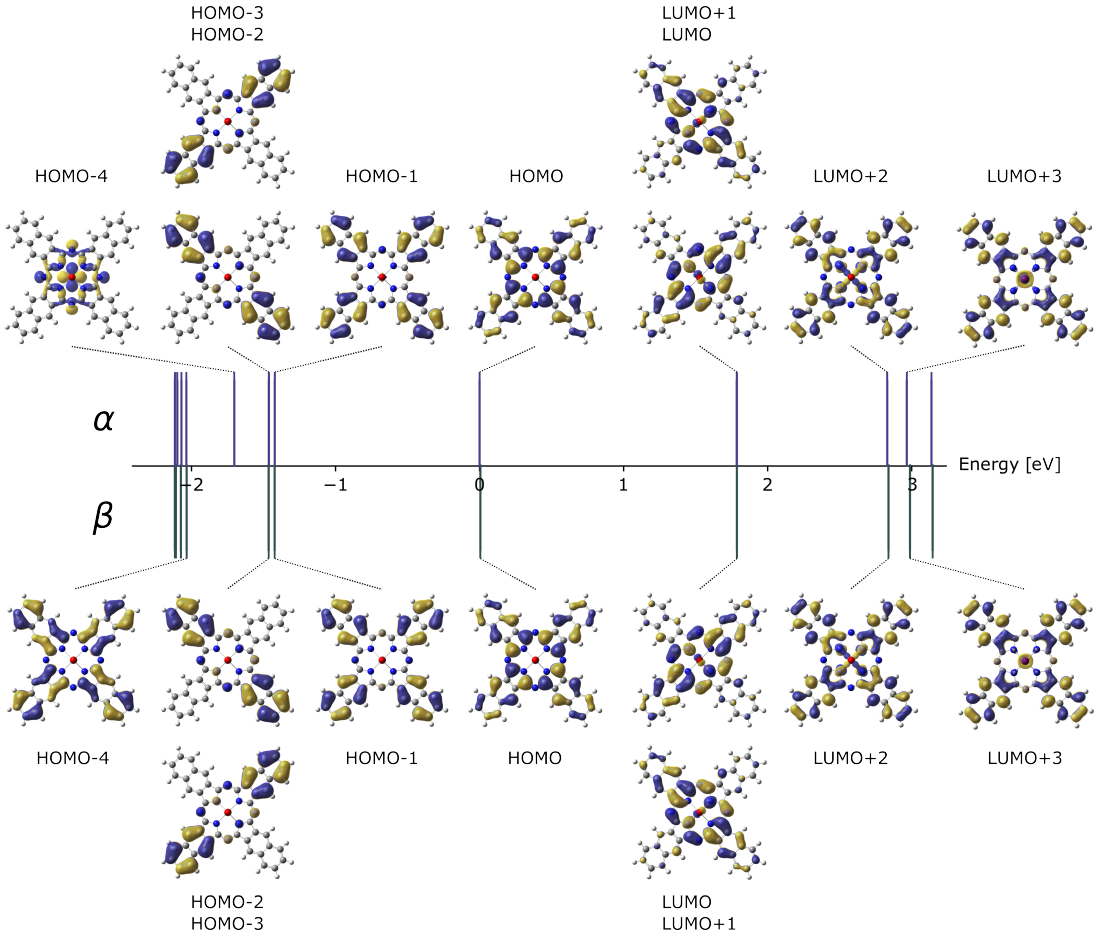

Figure 5.10: Molecular orbitals in both spin-channels for the neutral gas-phase VONc molecule calculated with Gaussian16 and the basis set B3LYP and the functional 6-31++g(d,p), sorted by energy. The single spin sits in HOMO-4 in the α-channel.

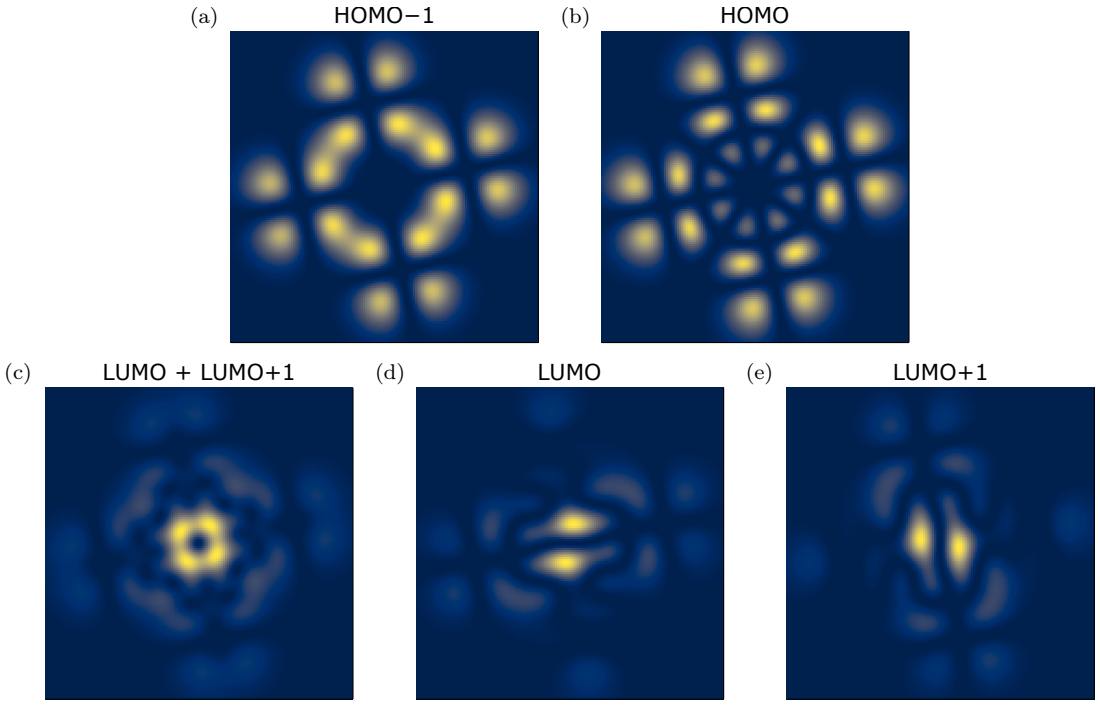

Figure 5.11: Simulated $\mathrm{d}I/\mathrm{d}V$ maps from the neutral gas-phase VONc molecule. Since the LUMO and LUMO+1 are degenerate in energy, the map in (c) is the summation of the individual maps in (d) and (e).

tunnelling current into account. We therefore have to determine the nature of the excited states involved first.

5.4 Excited States and Vibronics

Since the resonances in question are in the negative bias range and our bias voltage is applied on the sample side, we have to consider an electron being removed from the VONc molecule and thereby a transiently positively charged molecule. Since we consider our neutral VONc molecule to be in a doublet state ($S = \frac{1}{2}$), removing one electron can naturally either give us a singlet state ($S = 0$) or a triplet state ($S = 1$). To determine the energetical order of these excited states, we again perform DFT calculations with Gaussian16 for the gas-phase excited molecules in both cases, and find that the triplet state is lower in energy than the singlet state by $\sim 0.9\,\mathrm{eV}$. This has also been reported in literature for the closely related VOPc molecule [173]. We therefore assume the triplet state to be relevant for our vibronic transition.

Using the optimised geometry and resulting orbitals as the starting point, we simulate the vibrational modes for the gas-phase VONc molecule using Gaussian16 with the functional B3LYP and the basis set 6-31++g(d,p), and calculate the relevant Huang-Rhys (HR) factors and the resulting simulated $\mathrm{d}I/\mathrm{d}V$ spectrum using Igor code written by N. Krane which implements the Franck-Condon model and also takes the combination of

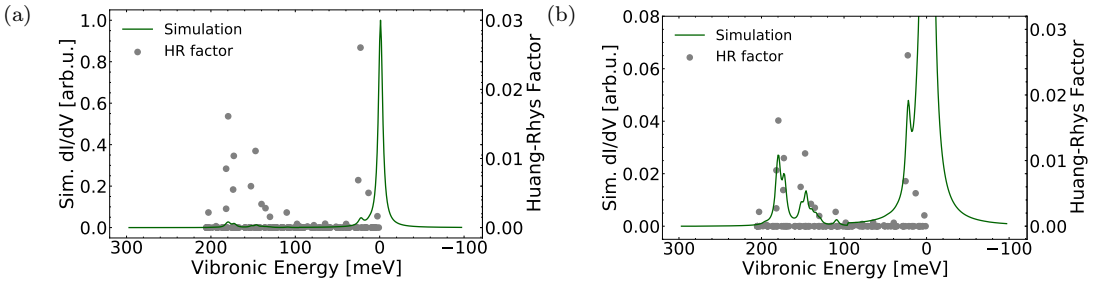

Figure 5.12: (a) Calculated vibronic dI/dV spectrum (green) and the Huang-Rhys factors associated to each vibronic energy (grey dots). (b) A zoom into the simulated spectrum for better visibility of the vibronic modes low in intensity. Most Huang-Rhys factors are very low, indicating a weak electron-phonon coupling.

modes into account (for more information, see Ch. 2.6 and Ref. [85] and its supplementary information, as well as Ref. [174]). Both are plotted in Fig. 5.12. It can be seen that the HR-factors for most modes are very low (< 0.01) and the resulting vibronic spectrum is therefore low in intensity. For better visibility, a zoom is shown in Fig. 5.12b, cutting off the elastic peak. We see a small peak near the elastic peak at about 20 meV and two broad features with very low intensity at ~ 150 meV and ~ 180 meV. This does not match our experimental observations on the ligands, where we see a multitude of peaks following after the PIR for ~ 1.5 V, and only partially matches the group of peaks observable on the centre. While this could be an effect of the surface, which is not accounted for in these gas-phase simulations, we also have to move beyond the static Franck-Condon picture and consider the local implications of the vibrational modes by now finally accounting for vibration-assisted tunnelling (VAT).

5.5 Vibration-Assisted Tunnelling (VAT)

To simulate the effect of VAT on both dI/dV spectra and dI/dV maps, we follow a computation procedure implemented by N. Krane (see Ch. 2.6 and Refs. [103, 174] for more information). This gives us the evolution of peaks and lineshapes when moving across the VONc molecule and the simulated dI/dV map of each state. Here, we show a few of these simulated data sets to illustrate (see Fig. 5.13).

Off-centre on the ligands (Fig. 5.13a), the dI/dV spectrum is nearly identical to the one shown in the previous section in Fig. 5.12. This is as expected, since the effects of VAT are usually most pronounced in a region with many nodal planes [102], in our case the centre of the molecule. The PIR is – of course – the HOMO and keeps its spatial distribution.

If we now move along the ligand towards the centre (Fig. 5.13b), it can be seen immediately that on a nodal plane, the spectrum changes: The intensity of the PIR is expectedly reduced, and we see the emergence of grouped satellite peaks. Directly at the crossing point of both nodal planes of the HOMO on the ligand (Fig. 5.13c), we see that a strong peak appears about ~ 30 meV away from the energy of the PIR. Mapping out its spatial extent reveals that it is indeed centered at the nodal planes but also shows

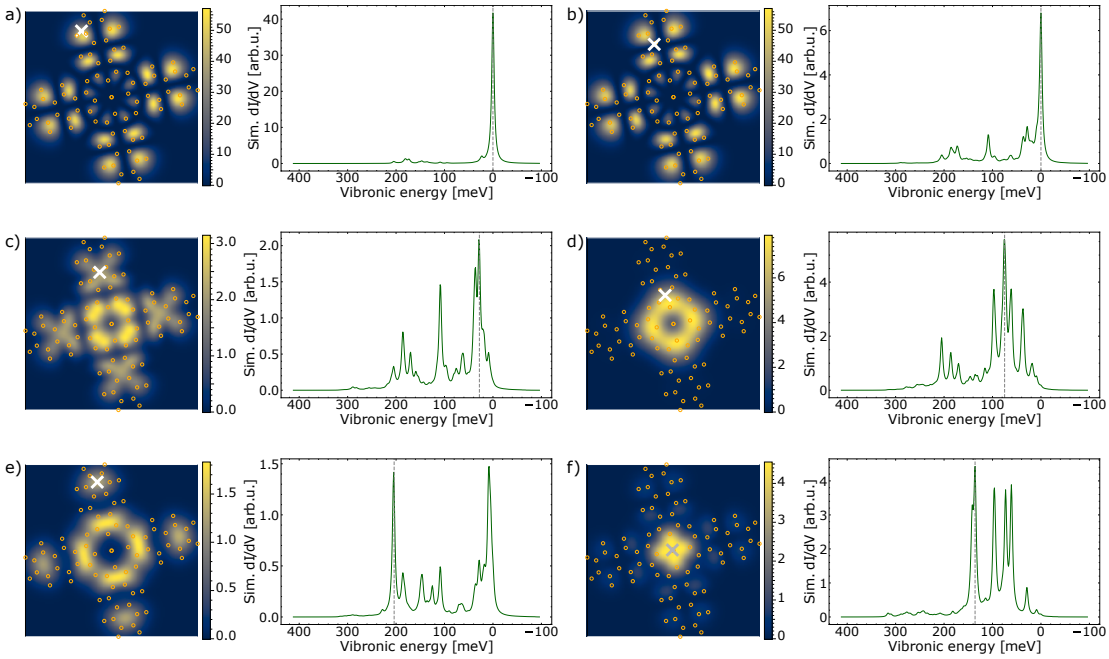

Figure 5.13: Simulated vibronic $\mathrm{d}I/\mathrm{d}V$ spectrum with VAT taken into account at the position marked with a cross and the simulated $\mathrm{d}I/\mathrm{d}V$ map at the energies marked with the grey line in the spectrum next to it. Note that the colour scale range is different for each map. The position of the VONc molecule's atoms is indicated by the faint circles.

some intensity around the centre.

In the centre of the VONc molecule (Fig. 5.13d), the intensity of the group of peaks around $\sim 80\,\mathrm{meV}$ continues to increase while the PIR is almost completely suppressed. The peak at 80 meV shows a ring-like spatial distribution around the centre with two faint perpendicular nodal planes. We also see the emergence of a peak group around $\sim 200\,\mathrm{meV}$ from the elastic peak. Interestingly, this peak is also very pronounced when in the centre of the outer carbon ring, almost the same intensity as the PIR (Fig. 5.13e).

At the very centre (Fig. 5.13f), we see a more spread out series of peaks at $\sim 60\,\mathrm{meV}$, 100 meV and 140 meV, all of similar intensity. The very last (double) peak is essentially only present at this position on the molecule.

If we now compare these simulations to our experimental data as in Fig. 5.6, we can see a tentative qualitative agreement in the overall trend: Strong PIR at the ligands with slight satellite peaks when moving towards the centre, with the PIR becoming suppressed and a series of peaks appearing at higher negative biases.

To compare in a more qualitative way, we plot in Fig. 5.14 simulated line spectra along different lines along the molecule and compare to our experimental data, while accounting for a voltage drop of $\sim 10\,\%$ over the MoS_2 monolayer [103] and after correcting for the tip perturbation potential as shown above in Sec. 5.2. When compared in this fashion, it becomes apparent that the energy scales do not match exactly. This is likely a result of the simulation stemming from the gas-phase molecule, as the interaction with the Au(111) underneath the MoS_2 changes the energy levels of a molecule slightly (see

Ch. 2.4).

Another difference lies in the spectra over the centre of the molecule. In the experimental data, we see a peak structure dominating the spectrum at $\sim 250\,\mathrm{mV}$ from the elastic peak, reaching almost the same intensity as the PIR on the ligands. In the simulated spectrum, a similar peak structure is visible at $\sim 150\,\mathrm{meV}$, but the spectrum is dominated by the triple peak structure at $\sim 80\,\mathrm{meV}$, which also does not reach the intensity of the elastic peak.

These differences are likely the result of a slight change in the electronic structure due to the effect of the surface, as already discussed in the previous section which could change the wavefunction overlap and thereby the intensity in the $\mathrm{d}I/\mathrm{d}V$ signal. Another crucial aspect is the orientation of the VONc molecule's VO-bond with respect to the surface. As we cannot ascertain this orientation from STM topography, and the tip could influence this bond during the measurement as well, the molecule's centre is especially prone to effects that do not enter this simulation.

All in all, it can still be seen that even 'only' a simulation based on the gas-phase molecule can lead to results that are quite good at approximating the experimental results and thereby enable us to identify the physical mechanisms that create this molecular fingerprint.

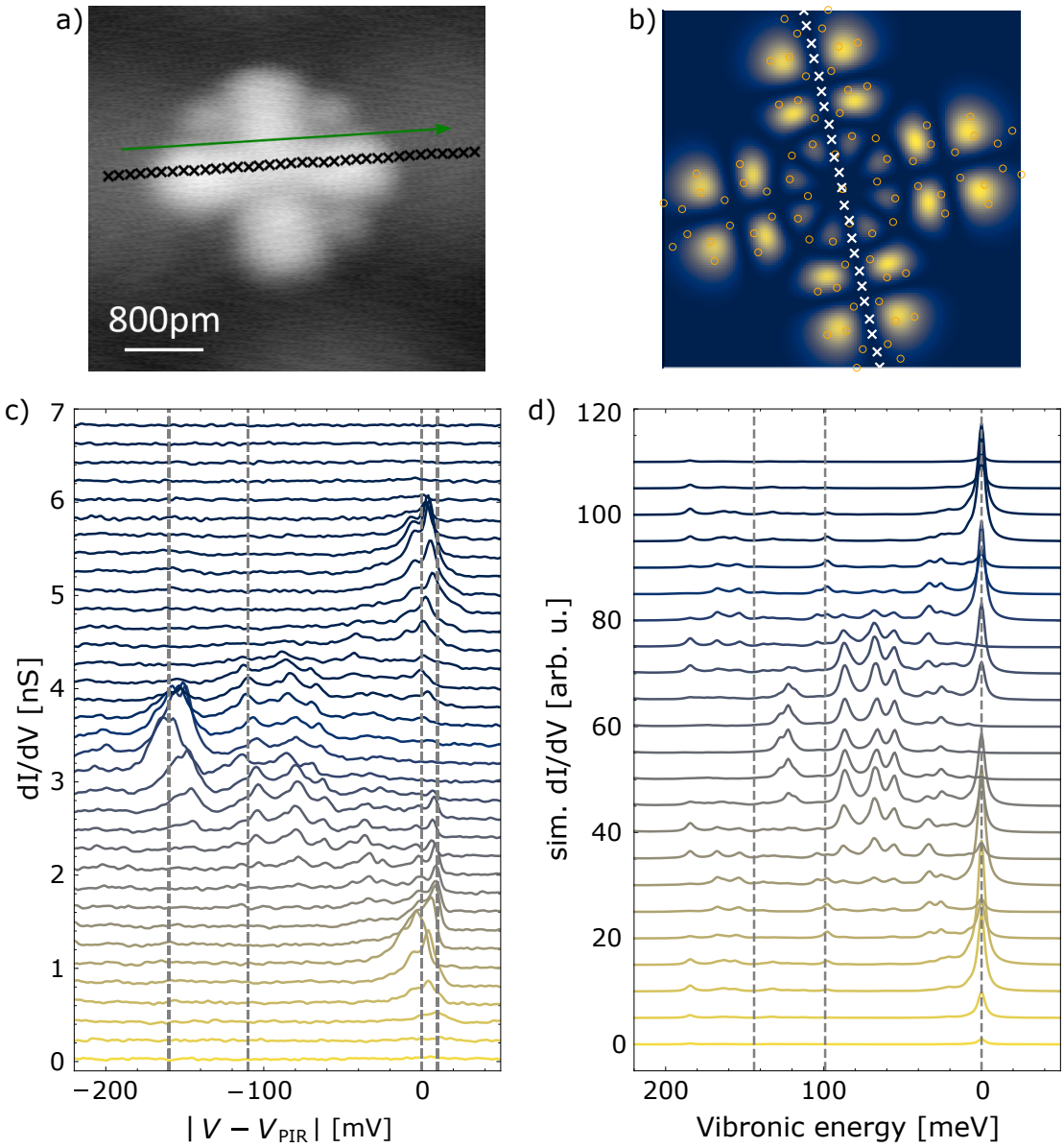

Figure 5.14: Comparison between experimental data (left) and simulation (right). The crosses in (a) the STM topography and (b) the simulated $\mathrm{d}I/\mathrm{d}V$ map of the HOMO with circular dots as indicators for the atoms' positions denote the position of the shown spectra. The individual $\mathrm{d}I/\mathrm{d}V$ spectra are vertically offset for better visibility. The experimental data is the same dataset as shown in Fig. 5.6c, now corrected for the tip-perturbation potential as detailed in the main text of Sec. 5.2. The grey dashed lines in (c) at 10 mV, 0 mV, −110 mV and 160 mV are guides to the eye. Note that the energy scale of the simulation in (d) takes a 10 % voltage drop over the MoS_2 monolayer into account, the grey dashed lines at 0 mV, 100 mV and ∼ 145 mV therefore correspond to the grey lines in (c).

5.6 Conclusion

All in all, we have explored the different aspects of VONc on MoS_2/Au(111) in this chapter. Successful evaporation of VONc molecules on MoS_2/Au(111) yielded single molecules appearing in a four-leaf clover-like shape in STM topography, along with some small circular protrusions that are likely contaminants. While we did observe some changes in apparent height of the molecular centres, the orientation of the VO-group with respect to the surface could not be determined by STM topography and requires further investigation with e. g. AFM.

Electronically, we observed a broad state just outside the CBM of the MoS_2 bandgap at $\sim 1.7\,\mathrm{V}$ and a strong resonance inside the bandgap at negative biases around $-500\,\mathrm{mV}$. This resonance is assigned to the HOMO from the spatial distribution visible in the bias-dependent topography. When moving across the molecule, we observed an energy shift of $\sim 80\,\mathrm{mV}$ away from E_F when in the centre compared to on the ligands. This was determined to be caused by the tip-perturbation potential, with additional changes in the peak intensity and lineshapes caused by vibration-assisted tunnelling (VAT). The effect of VAT was modelled theoretically and the resulting simulation qualitatively matches the experimental data. Quantitatively, the intensity distribution on the centre does not match the observed data, which could be a limitation of the simulation in that the MOs of the gas-phase molecule are likely slightly changed through the interaction with the surface. This in turn can have an effect on the relative intensities of the resonances. This could be modelled by e. g. adding a graphene sheet below the molecule during the structure optimisation, as done for example in Ref. [175] for the molecule ethyl-DADQ on MoS_2/Au(111), or using a more expansive theoretical framework that is outside the scope of this thesis.

All in all, the system of VONc on MoS_2/Au(111) has been shown to be a model system to explore the various effects of electronic processes in detail, showcasing the strengths of the molecular family of (na)phthalocyanines and MoS_2 as a substrate for enhancing the lifetime of vibrational states.

6 Possibilities of the 2D-Semiconductor 2H-$MoTe_2$ as a Substrate

In this chapter we investigate the bulk 2D-material of 2H-$MoTe_2$ as a possible candidate substrate for molecular adsorption. As described in Ch. 2.3.3 in detail, bulk $MoTe_2$ is a 2D-semiconductor with a relatively small indirect bandgap of 1.0 eV [71, 72]. In contrast to bulk MoS_2 with an indirect bandgap of 1.23 eV [41], it is therefore in an energy range where e. g. optical excitation with IR-radiation is possible. Combined with the deliberate adsorption of carefully chosen molecules, this substrate could therefore prove itself to become a new playground where different effects such as charge transfer can be explored. This chapter therefore acts as an introductory glimpse at the possibilities of $MoTe_2$ in STM and the challenges involved.

6.1 General Properties

The bulk shard of $MoTe_2$ is prepared as described in Ch. 3.2.4, where the first challenge when working with this type of material in STM lies in contacting the uppermost layer properly to ensure a good bias contact.

Upon transferring into the low-temperature STM, it quickly becomes apparent that this contact is temperature dependent as well. With the machine at its usual operating temperature of 1.4 K, no tunnelling current is observed, even at bias voltages of 10 V and macroscopically visible contact of the Au-STM tip and the $MoTe_2$ sample. Increasing the temperature to about 10 K leads to a measurable tunnelling current under the same circumstances and makes STM measurements possible.

This temperature dependence is most likely *not* a material property, but instead a property of the electrical contact of the metal of the sample holder, where the bias voltage is applied to, to the uppermost semiconducting layer. It is possible that a Schottky barrier [176, 177] forms at the interface, the precise nature of which depends on the specifics of the used material, the contact area size and shape, and consequently means that the temperature broadening becomes a critical threshold to allow or inhibit current flow across the interface. All measurements in this chapter are therefore conducted at 77 K.

The bare $MoTe_2$ surface appears in STM as shown in Fig. 6.1a: Atomically flat and mostly featureless over large areas, with step edges so rare that none were observed in the course of these measurements. The surface is speckled with bright protrusions with some faint 'halos', and some rarer dark depressions on the otherwise pristine surface. These

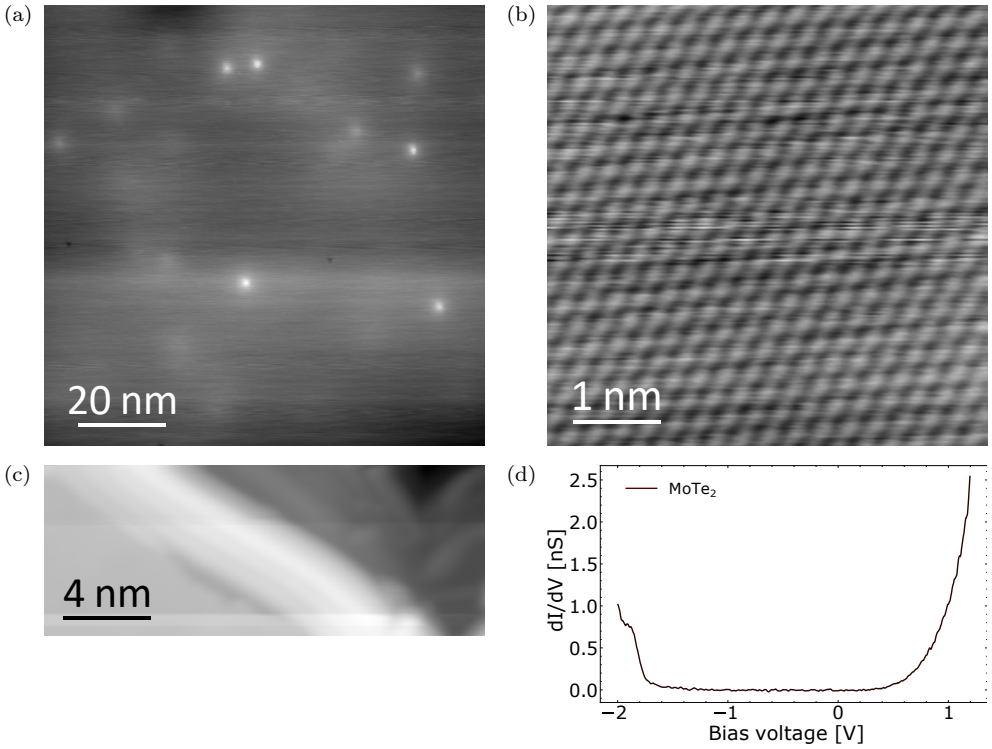

Figure 6.1: (a) Overview STM topography of $MoTe_2$: The surface appears atomically flat, speckled with bright defects and faint 'halos'. Slight streaking in the topography shows small instabilities in the STM junction (setpoint: 1 V, 200 pA). (b) Atomic resolution on $MoTe_2$, showing a regular hexagonal pattern of the Te atoms (setpoint: 500 mV, 2 nA). (c) 'Cracked' $MoTe_2$ surface after indentation with the STM tip (setpoint: −3.5 V, 300 pA). (d) $\mathrm{d}I/\mathrm{d}V$ spectrum recorded on $MoTe_2$ with a Au tip, showing a clear bandgap with zero conductance between about −1.6 V and 400 mV (feedback opened at 1.2 V, 500 pA, lock-in modulation amplitude 5 mV).

defects will be explored in more detail in the next section. Atomic resolution is also achievable as visible in Fig. 6.1b, and shows the upper Te-layer of the TMDC-sandwich, expectedly arranged in the familiar hexagonal patterns according to the 2H lattice structure. Indenting the STM tip forcefully into the surface can lead to 'cracking' and results in 'craters' as visible in Fig. 6.1c.

Electronically, we can see a very clear and sharp bandgap on the pristine $MoTe_2$: As visible in the $\mathrm{d}I/\mathrm{d}V$ spectrum in Fig. 6.1d, we have zero conductance between ~ -1.6 V and ~ 400 mV at a setpoint of 1.2 V and 500 pA. On the positive bias side, we see a steep increase in conductance, while on the negative bias side, a small shoulder is visible at ~ -1.9 V additionally. The bandgap visible in STM and therefore at the Γ point is consequently between 3 V and 2.5 V wide. This is in accordance with the theoretically calculated bandstructure of 2H-$MoTe_2$ which shows the widest bandgap of more than 2 eV at the Γ point [73], as shown in Fig. 2.11 in Ch. 2.3.3. Detailed determination of the conduction band minimum (CBM) and valence band maximum (VBM) edges would require further measurements with e. g. κ-probe STM, as described in Ch. 2.3.2.

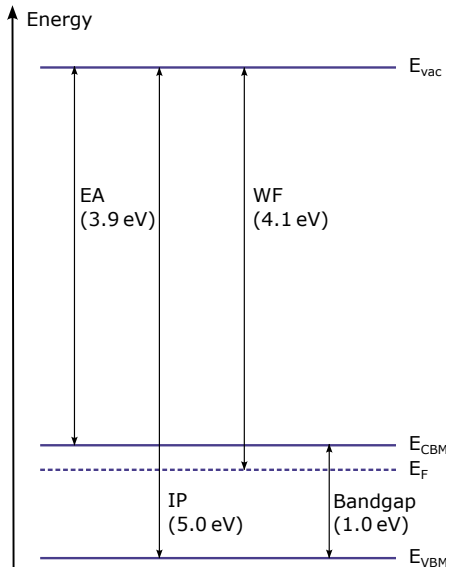

Figure 6.2: Energy level diagram of n-type $MoTe_2$ (to scale). The indicated values are taken from: electron affinity (EA): Ref. [179], ionisation potential (IP): Ref. [181], workfunction (WF): Ref. [180] and bandgap: Refs. [71, 72].

We see that the bandgap is not centered around zero bias and extends further into the negative bias range than into the positive side. This tells us that $MoTe_2$ has a Fermi level closer to the CBM [178], and is therefore an n-type semiconductor, as illustrated in Fig. 6.2. This will become relevant for molecular adsorption as shown later in this chapter. The observed n-type characteristics are consistent with reports in literature which give the electron affinity (EA) as $\sim 3.9\,\text{eV}$ [179], the workfunction (WF) as 4.1 eV [180], the ionisation potential (IP) as 5.0 eV [181] and the position of the VBM with respect to E_F at 0.8 eV [181]. The type of semiconductor seems to also depend on the growth method of the $MoTe_2$ crystal and can be influenced by post-processing [182–184]. The crystal used in Ref. [181] was also purchased from HQ Graphene, like ours, and therefore likely grown under similar conditions.

6.2 Defects with In-Gap States

As introduced above, we observe intrinsic defects in STM topography that can be categorised as either 'bright' (higher apparent height) or 'dark' (lower apparent height) as visible in Fig. 6.3, with the bright defects more frequently observed than the dark ones.

The dark defects appear as hexagonal stars with one central round depression as visible in Fig. 6.3b. These dark defects have been observed in Ref. [80] as well and are labelled there as Te-vacancies, but with no clear argument given behind this identification. As discussed in Ch. 2.3.3, this seems to contradict Ref. [81], where a differently appearing defect was identified as a Te-vacancy. Since in other TMDCs such as MoS_2 a defect in the chalcogen layer occurs most frequently during growth [56], it seems unlikely that the

rarer dark defects are indeed Te-vacancies. But since $MoTe_2$ behaves differently than MoS_2 in other aspects as well (see Ch. 2.3.3), further investigation with e. g. AFM is needed for a definite identification.

Of the bright defects, there are three different shapes visible: they can be hexagonal (Fig. 6.3c), triangular (Fig. 6.3d) or roundish (Fig. 6.3e) in appearance, which is mostly visible in their faint surrounding 'halos'. The bright defects also occur more frequently than their dark counterparts, and it cannot be fully excluded that they stem from external contaminants, such as single atoms or clusters lying on the surface, even though, as described in Ch. 2.3.3, interstitials are apparently energetically favoured on $MoTe_2$ [81]. Moving defects have been observed anecdotally as well, which would be in accordance with mobile Mo interstitials [81, 82], or, of course, adsorbants on the surface.

The bright defects have been observed in literature as well [80–83], and are either labelled as Te-vacancies, Mo defect sites or interstitials. The STM topographies shown in these references do not resemble the observed defects, likely because they were recorded at different bias setpoints. The respective authors chose setpoints in the negative bias range that could not be stabilised in our measurements, which makes comparison difficult. We can therefore not identify our observed defects by comparing to literature. The differently appearing defects are most likely different types of defects as well, such as different atoms as adsorbants or interstitials, and/or different atomic sites. A detailed investigation with e. g. AFM could shed light on this matter.

Electronically, all types of defects show in-gap states, albeit at slightly different energies, as shown in the $\mathrm{d}I/\mathrm{d}V$ spectra in Figs. 6.4b, 6.5b, 6.6b and 6.7b at our measurement temperature of 77 K. All bright defects show broad peaks at around -1 V, -650 mV to -600 mV and a shoulder at ~ 150 mV in the onset of the valance band (VB). The hexagonal defect shows additionally a strong negative differential resistance (NDR) after the resonance at -1 V, and the triangular defect exhibits instabilities at high negative biases. The shoulder in the VB onset is very sharp as well for this defect. The roundish defect shows a third broad peak at ~ -1.15 V.

Recording constant height $\mathrm{d}I/\mathrm{d}V$ maps at the energies marked with the grey dashed lines in the respective $\mathrm{d}I/\mathrm{d}V$ spectra reveals the spatial distribution of the states, and here the differences between the defects suddenly become apparent: The hexagonal defect shows peculiar asymmetric patterns in the $\mathrm{d}I/\mathrm{d}V$ maps, as the peak at -1.08 V shows a signal mostly on the lower right of the defect, and at -660 mV what could be called three touching rings. At 230 mV, the intensity is spread roughly hexagonally again.

The triangular defect, on the other hand, keeps its triangular symmetry in most maps: At -980 mV, the strongest resonance in the bandgap, we see a small, bright triangle in the centre, surrounded by a bigger, inverted triangle with dark spots in the corners. At -600 mV, the signal is very faint and spread out over the defect, while at 120 mV we can see a resemblance to the inner triangle again, this time with the outer triangle inverted in intensity.

The roundish defect shows the most surprising geometry in the $\mathrm{d}I/\mathrm{d}V$ maps: At -1.15 V and -960 mV, we can see three bright circles, arranged in a regular triangle with a faint 'halo' around them, that also follow the lattice geometry of the top Te-layer. At -650 mV we see a different shape that only has one symmetry axis and appears as a

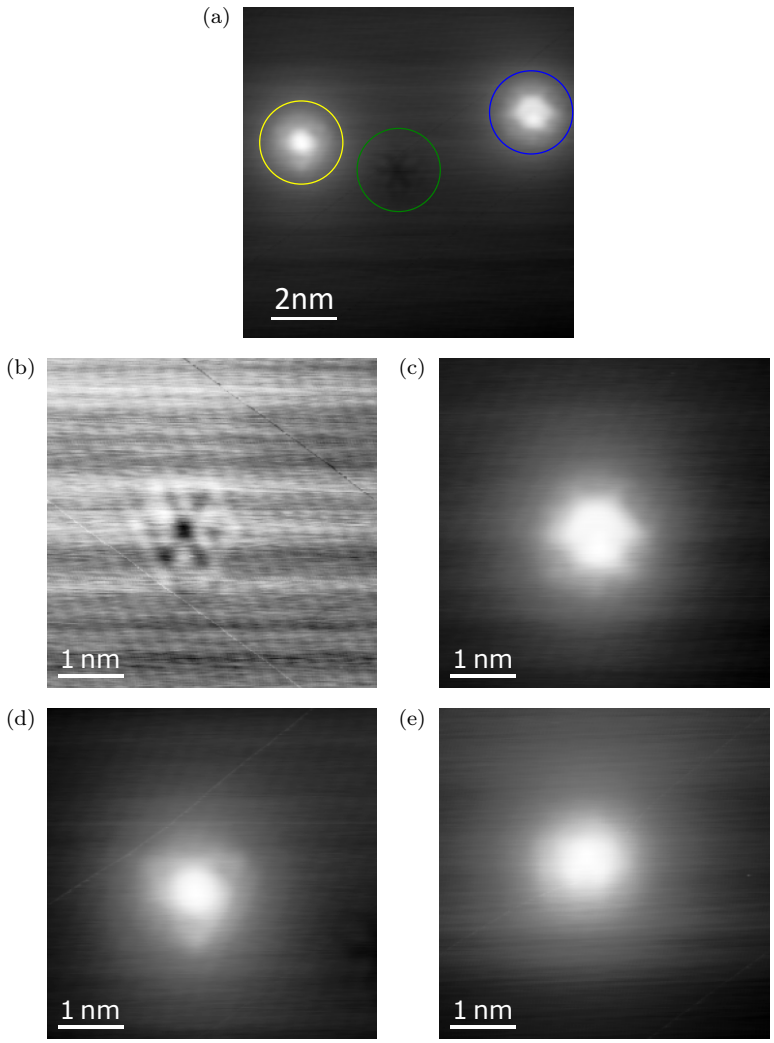

Figure 6.3: STM topographies of different defects on $MoTe_2$: (a) Three types of defects in close proximity to each other: Bright hexagonal (blue circle), bright triangular (yellow circle) and dark (green circle). Close-up views of the different defects: (b) Dark defect, (c) bright hexagonal defect, (d) bright triangular defect and (e) bright roundish defect (setpoints: 500 pA, 400 mV).

'W'-shape with a squashed 'Y'-shape on top. This state is most pronounced right on top of the defect. Lastly, the shoulder at 120 mV in the onset of the VB shows again the triangular circles, but more smeared out than the states inside the gap.

We can therefore see that even though the electronic structure of these defects looks very similar in the $\mathrm{d}I/\mathrm{d}V$ spectra, their spatial distribution varies significantly and must therefore stem from different origins.

The $\mathrm{d}I/\mathrm{d}V$ spectrum taken over the dark defect shows only a faint shoulder at ~ 1.1 V and a steeper and earlier onset of what we assume to be the CBM, as visible in Fig. 6.7b. Even though the tip and surface interaction is less stable at these energies over the defect, mapping out the spatial distribution of these states in constant height $\mathrm{d}I/\mathrm{d}V$ maps in Fig. 6.7 reveals what could be seen as a similar triangle as for the bright defects with some additional smeared out intensities. The junction at these energies is rather unstable and makes conclusive identification difficult.

These $\mathrm{d}I/\mathrm{d}V$ maps could be used to identify the different types of defects when used in conjunction with DFT simulations. The observed in-gap states show that the electronic structure of $MoTe_2$ is significantly altered by the presence of these defects. When introduced in a controlled manner, they could act as a building block of a more complex system, potentially allowing functionalisation and in turn defect engineering, which leads us to the next section of molecules on $MoTe_2$.

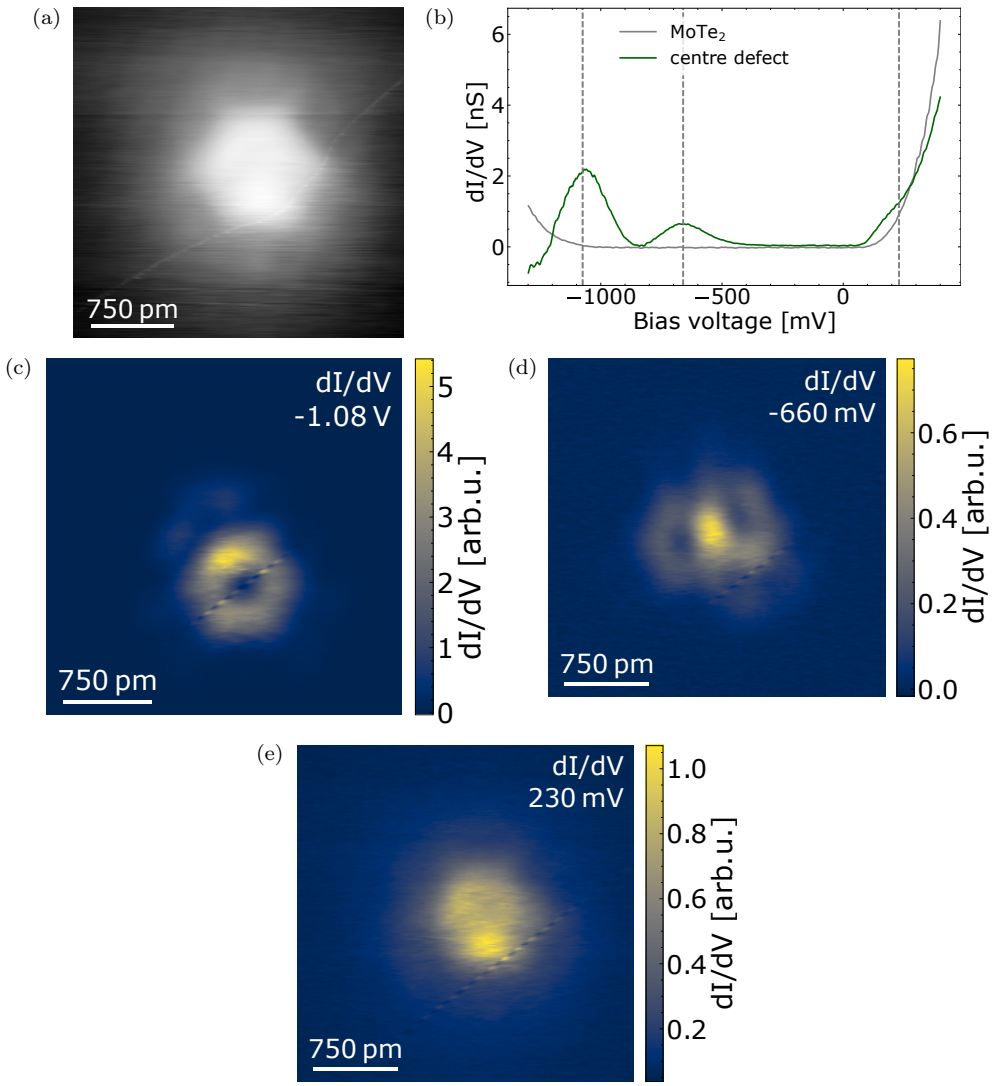

Figure 6.4: Bright defect on $MoTe_2$ with a hexagonal appearance. (a) STM topography (setpoint: 500 pA, 400 mV) and (b) $\mathrm{d}I/\mathrm{d}V$ spectrum recorded on the centre of the defect in green with reference taken on the pristine $MoTe_2$ in grey (feedback opened at 400 mV, 500 pA, lock-in modulation amplitude 5 mV). Constant height $\mathrm{d}I/\mathrm{d}V$ maps recorded over the defect shown in (a), at (c) −1.08 V, (d) −660 mV and (e) 230 mV (feedback opened over centre of the defect at 400 mV, 500 pA, lock-in modulation amplitude 5 mV).

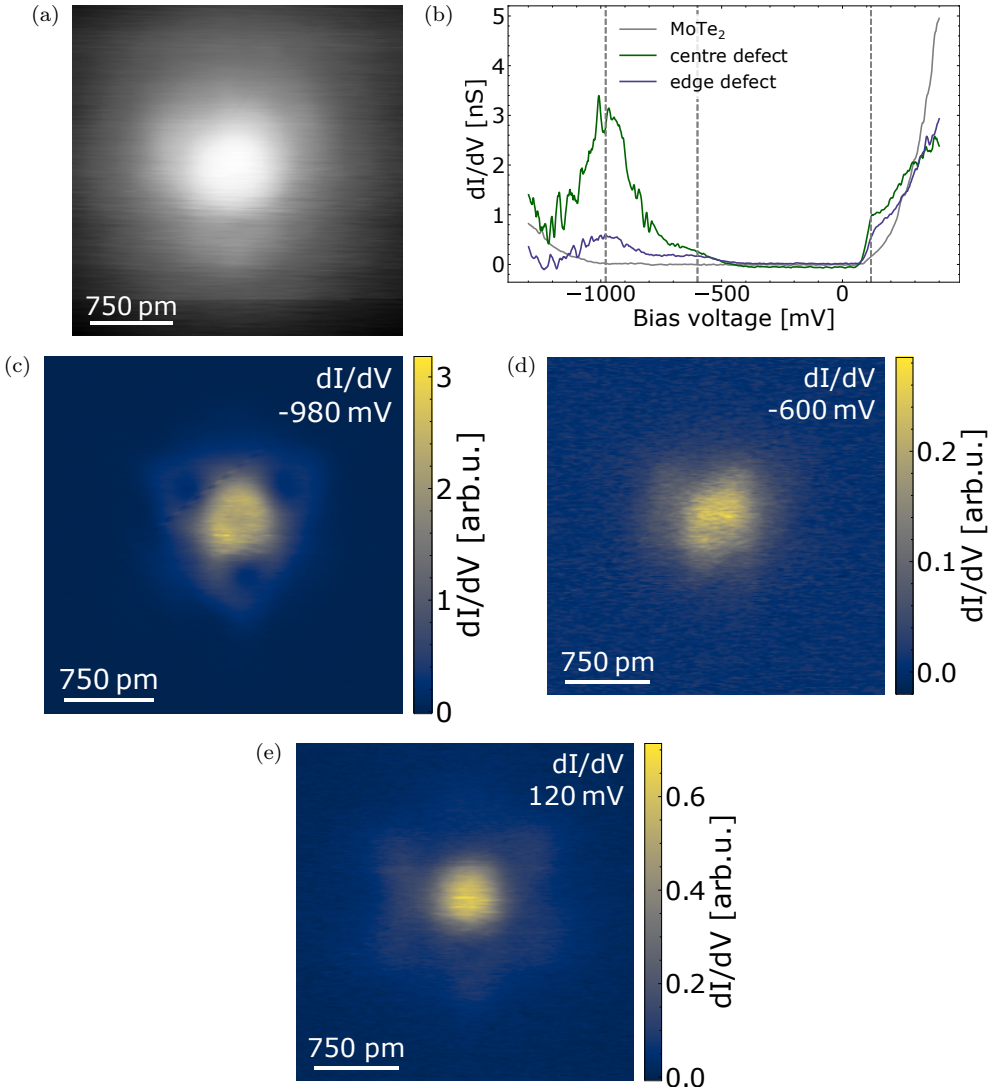

Figure 6.5: Bright defect on $MoTe_2$ with a triangular appearance. (a) STM topography (setpoint: 500 pA, 400 mV) and (b) dI/dV spectrum recorded on the centre of the defect in green, at the edge of the defect in blue, with reference taken on the pristine $MoTe_2$ in grey (feedback opened at 400 mV, 500 pA, lock-in modulation amplitude 5 mV). Constant height dI/dV maps recorded over the defect shown in (a), at (c) −980 mV, (d) −600 mV and (e) 120 mV (feedback opened over centre of the defect at 400 mV, 500 pA, lock-in modulation amplitude 5 mV).

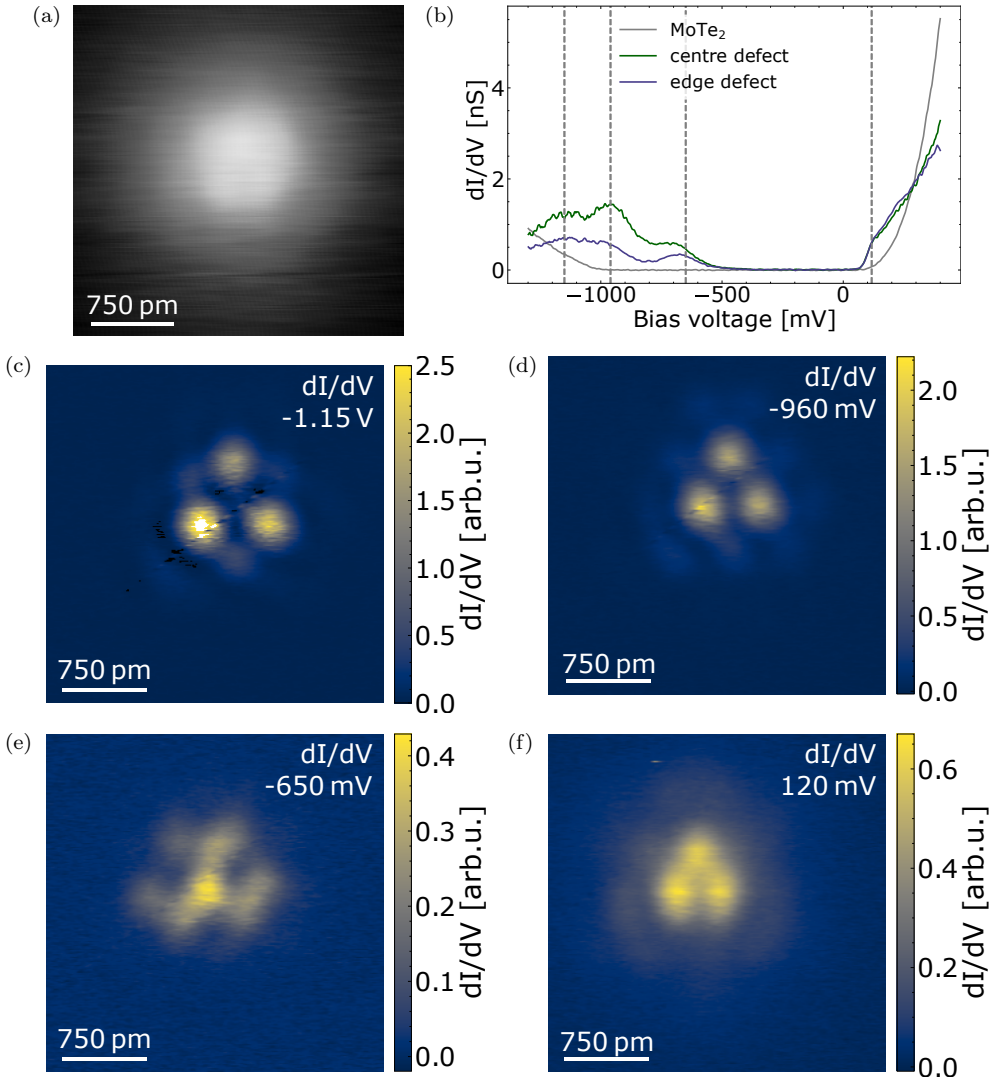

Figure 6.6: Bright defect on $MoTe_2$ with a roundish appearance. (a) STM topography (setpoint: 500 pA, 400 mV) and (b) dI/dV spectrum recorded on the centre of the defect in green, at the edge of the defect in blue, with reference taken on the pristine $MoTe_2$ in grey (feedback opened at 400 mV, 500 pA, lock-in modulation amplitude 5 mV). Constant height dI/dV maps recorded over the defect shown in (a), at (c) −1.15 V, (d) −960 mV, (e) −650 mV and (f) 120 mV (feedback opened over centre of the defect at 400 mV, 500 pA, lock-in modulation amplitude 5 mV).

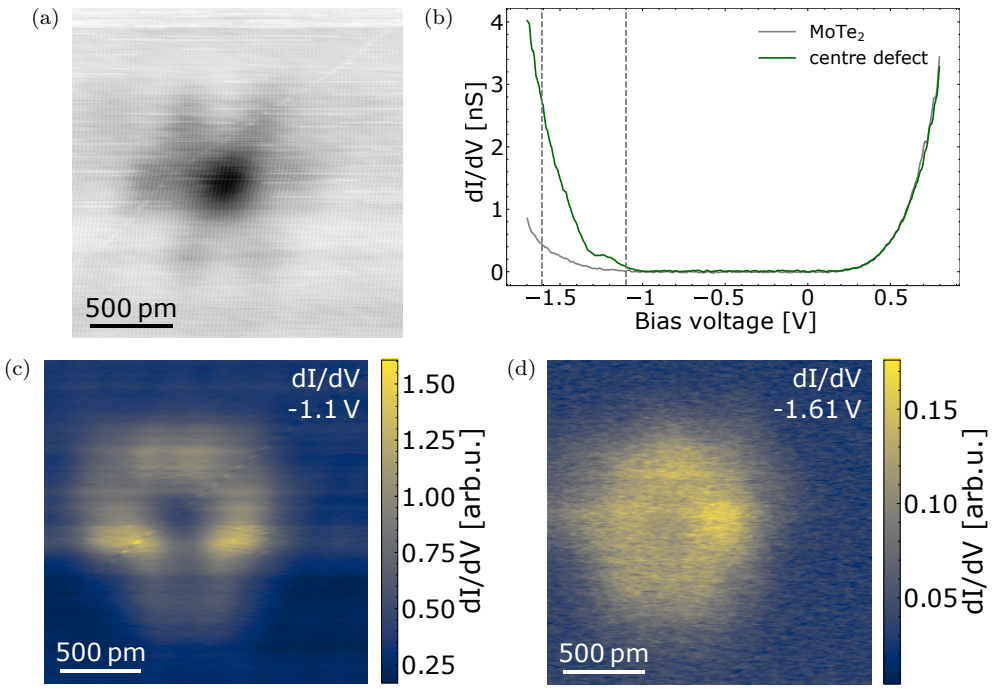

Figure 6.7: Dark defect on $MoTe_2$. (a) STM topography (setpoint: 500 pA, 400 mV) and (b) dI/dV spectrum recorded on the centre of the defect in green with reference taken on the pristine $MoTe_2$ in grey (feedback opened at 800 mV, 500 pA, lock-in modulation amplitude 5 mV). Constant height dI/dV maps recorded over the defect shown in (a), at (c) −1.1 V (feedback opened in lefthand bottom corner at 400 mV, 500 pA, lock-in modulation amplitude 5 mV) and (d) −1.61 V (feedback opened over centre of defect at 1.2 V, 500 pA, lock-in modulation amplitude 5 mV).

6.3 Initial Adsorption of F_4-TCNQ and TTF Molecules

To explore the capabilities of $MoTe_2$ as a platform further, we investigate its properties with respect to molecular adsorption. The two test molecules that are well-known and well-explored by themselves are 2,3,5,6-tetrafluoro-7,7,8,8-tetracyanoquinodimethane (F_4-TCNQ) and tetrathiofulvalene (TTF); their molecular structures are shown in Fig. 6.8. These molecules were chosen because of their opposite characteristics as electron acceptors (F_4-TCNQ) [185, 186] and electron donors (TTF) [187], as this plays a crucial role for molecular adsorption on semiconductors, which we will see shortly.

Both molecules were evaporated from a Knudsen cell under ultra-high vacuum on a fresh cleave of $MoTe_2$ and with the sample cooled down with lN_2. The samples were then investigated at 77 K in the STM.

F_4-TCNQ was evaporated from molecular powder at an evaporation temperature of 390 K for 2 min, with the manipulator on which the sample rests cooled down to 170 K during evaporation. TTF was evaporated from TTF-TCNQ salt at 350 K for 2 min with $T_{\text{manip}} = 150\,\text{K}$ and additional 3 min at a later stage under similar conditions of $T_{\text{manip}} = 160\,\text{K}$. The evaporation temperature was previously calibrated on Au(111) to ensure that mainly TTF evaporates from the salt.

As visible in Fig. 6.9, the evaporation of F_4-TCNQ was not successful. There are no F_4-TCNQ molecules clearly visible, only unidentifiable clusters of dirt. This is likely due to the electron accepting nature of F_4-TCNQ in combination with the *n*-type characteristics of $MoTe_2$which might prevent successful physisorption.

TTF, on the other hand, physisorbed on $MoTe_2$ in small islands as shown in Fig. 6.10, unlike on Au(111), where the TTF molecules spread out over the surface at low coverages, strongly repulsed from each other [87, 188]. The islands are mostly unordered, only some small areas show regular patterns as shown in the close-up view in Fig. 6.10d, where the TTF molecules form connected hexagonal 'flower' or 'bow tie' patterns with what could be called a domain boundary in the middle of the shown topography. The molecules are generally not very stable under the STM tip, visible as the dragging lines/instabilities in the STM topographies.

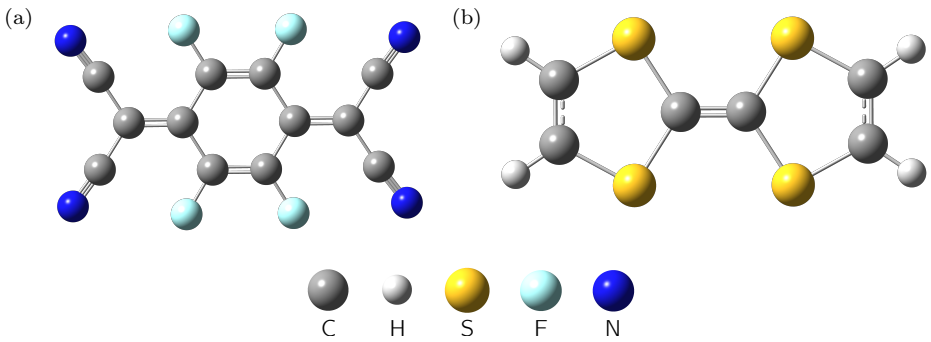

Figure 6.8: Molecular models in gas-phase of (a) the electron acceptor F_4-TCNQ and (b) the electron donor TTF.

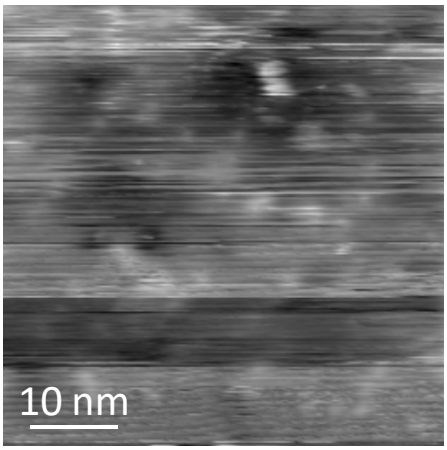

Figure 6.9: STM topography of $MoTe_2$ after evaporation of F_4-TCNQ molecules. While the surface is now littered with unidentifiable dirt, no clear molecular structures can be made out (setpoint: 1 V, 20 pA).

Depending on the tip, the individual TTF molecules appear as round protrusions (see Fig. 6.10d), as they do on e. g. Au(111) [87], or show a 'doughnut'-like shape (see Fig. 6.10a) that is indicative of the molecules' highest occupied molecular orbital (HOMO) in gas phase [189] which is shown in the inset in Fig. 6.10a. While this orbital contrast is likely enhanced by a functionalisation of the tip with a TTF molecule, imaging the shape of the gas-phase HOMO at positive biases points towards a charge transfer process between the TTF molecules and the $MoTe_2$ substrate, so that the HOMO has been depopulated. But since not all molecules appear with this 'doughnut'-shape in Fig. 6.10a, even when accounting for tip-changes during the recording of the topography, it is likely an influence of the environment on the energy level alignment of the system. As described in the first section of this chapter, we have identified our $MoTe_2$ substrate as an n-type semiconductor. TTF being an electron donor molecule therefore makes charge transfer likely, possibly facilitated by surface defects in the vicinity or underneath the molecules. To quantify this charge transfer, a more detailed study of the electronic properties is needed which would in turn require a stabilisation of the measured system.

An attempt at forming larger, ordered structures was made by post-annealing the substrate after molecular deposition to $T_{\mathrm{manip}} = 320\,\mathrm{K}$ for 7 min which partially led to the formation of larger molecular islands as visible in Fig. 6.11, where the TTF molecules form a rectangular lattice with some unidentified adsorbates on top of them. But also this structure did not yield the desired stability to allow for reproducible STS measurements.

While the high measurement temperature and instable system did not allow for the recording of conclusive $\mathrm{d}I/\mathrm{d}V$ spectra, a system under optimised evaporation conditions might lead to new insights about the interaction between molecules and $MoTe_2$, although similar (if not better) results are likely possible on MoS_2/Au(111) or other substrates.

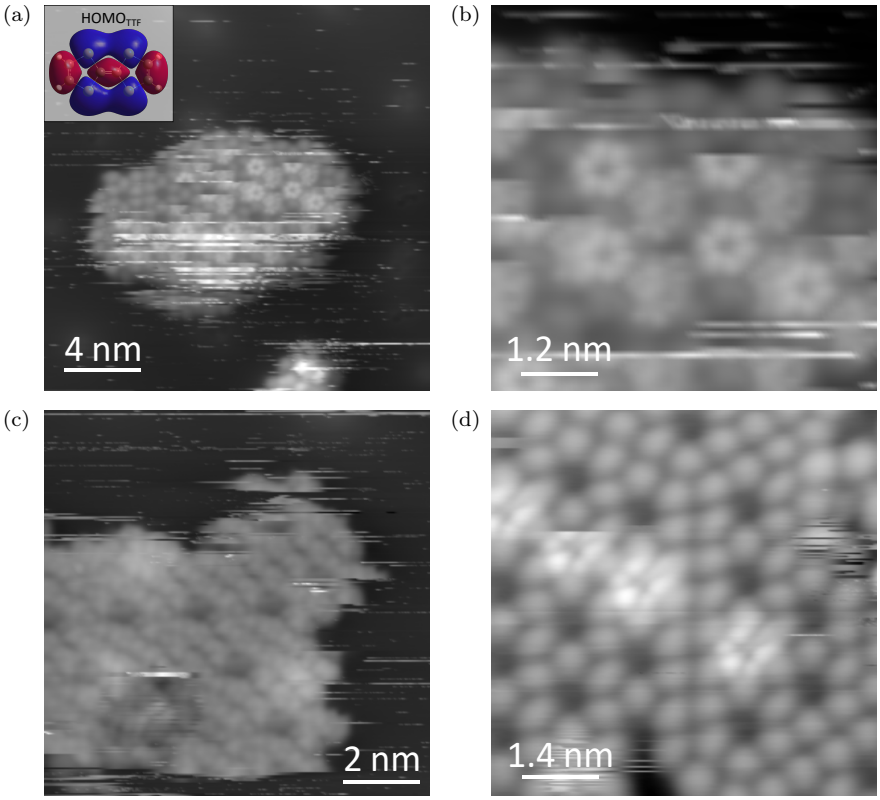

Figure 6.10: STM topographies of TTF molecules on $MoTe_2$. (a), (c) TTF forms mostly unordered molecular islands that are still mobile, especially at the island's edges. Inset: HOMO of TTF from gas-phase calculations, not to scale. (Inset taken and adapted from [190].) (b) Zoom into (a). In some areas of the island the TTF molecules appear with a 'doughnut'-like shape. (d) Some parts of the island show an ordered structure (setpoints: (a), (b) 1 V, 50 pA, (c), (d) 2 V, 10 pA).

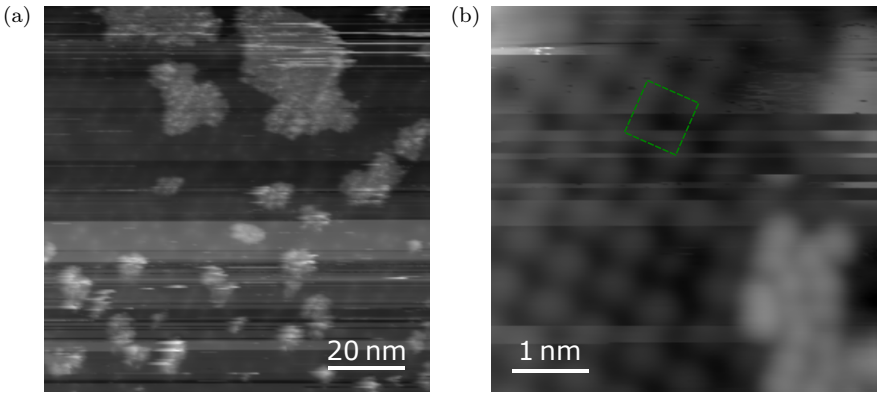

Figure 6.11: STM topographies of TTF molecules on $MoTe_2$ after post-annealing to 320 K for 7 min. (a) The TTF islands on the surface are mostly bigger, but not more stable than prior to post-annealing. (b) The larger islands show a rectangular order to the TTF molecules (indicated by the green dashed lines), with some unidentified dirt on top of them (setpoints: 2 V, 10 pA).

6.4 Conclusion

In this chapter we have taken an introductory look at the bulk 2D-semiconductor $MoTe_2$ with STM and STS. We successfully prepared the commercially purchased 2H-$MoTe_2$ crystal shard for STM measurements by contacting the first layer. Since this contact appears to be temperature-sensitive, we have conducted all measurements in this chapter at the liquid nitrogen temperature of 77 K.

After a successful cleave *in vacuo* we observed the pristine and atomically flat $MoTe_2$ surface and observed two main types of naturally occurring defects. While these defects cannot be conclusively identified by using STM only, we have recorded $\mathrm{d}I/\mathrm{d}V$ spectra that show in-gap states of these defects. These defects were mapped out spatially using constant-height $\mathrm{d}I/\mathrm{d}V$ maps as well. Electronically, $MoTe_2$ exhibits a bandgap of about 2.5 V to 3 V in STS which is asymmetric around E_F. This asymmetry led us to identify $MoTe_2$ as an n-type semiconductor which is in agreement with results in literature.

Finally, we evaporated the molecules F_4-TCNQ and TTF onto $MoTe_2$ and observed that the electron affinity/ionisation potential of the molecules seems to play a significant role when physisorbing on $MoTe_2$: Only the electron donor TTF could physisorb on the $MoTe_2$ surface, forming islands which show evidence of charge transfer, while the electron acceptor F_4-TCNQ could not be evaporated successfully. While the external parameters for evaporation such as sample temperature can influence the outcome of an evaporation like this quite severely, the difference in behaviour is already quite telling. It is therefore recommended to choose molecules with a low ionisation potential when evaporating on $MoTe_2$ to increase the chances of a successful physisorption. The strong n-type characteristics could make $MoTe_2$ an interesting candidate to explore the modification of energy levels and charge transfer processes in hybrid systems in combination with carefully chosen evaporants.

All in all, $MoTe_2$ is a challenging material to work with in STM. The flakiness of the surface poses a high risk to the tip which can only be recovered after tedious tip preparation procedures on a metal of choice or mechanically outside the vacuum. Coupled with the challenges of creating a good electrical contact, achieving a good cleave *in vacuo* and finding a flat area for initial approach, there are not many advantages 2H-$MoTe_2$ offers for STM over other, already well-established materials such as MoS_2, NaCl or MgO. While there are fascinating properties of $MoTe_2$ in its various forms as introduced in Ch. 2.3.3 that are still not fully explored and where STM/STS could offer a valuable spatially-resolved perspective, 2H-$MoTe_2$ might only become a viable substrate for STM if the outlined difficulties can be overcome reliably.

7 Conclusions

As stated in the very beginning of this thesis, gaining a fundamental understanding of the interaction between molecules and 2D-semiconductors in hybrid systems is a necessary prerequisite for possible innovation. Unravelling the details in small systems is the groundwork for creating larger systems based on the smaller systems which in turn can find purpose in even larger applications. In this thesis we have therefore explored the fundamental aspects of three different combined molecular/semiconducting systems using STM and STS.

First, we investigated the system of CF_3-3P-S(H) on Au(111), on MoS_2/Au(111) and anchored to S-vacancies in MoS_2/Au(111) and the different adsorption scenarios involved. On Au(111), the CF_3-3P-SH molecules physisorb, forming molecular structures that point towards an attractive intermolecular interaction, possibly mediated by the Au(111) surface through Au adatoms. Spectroscopy revealed a broad molecular state at $\sim 2.7\,\mathrm{V}$ which we assign to the lowest unoccupied molecular orbital (LUMO) of the molecule. In small molecular clusters, this state was observed to shift up to 300 mV in energy, indicating further intermolecular interaction.

On MoS_2/Au(111), the CF_3-3P-SH molecules physisorb and form different structures depending on the sample temperature during deposition. All structures remain quite mobile and therefore only weakly interact with the MoS_2. Spectroscopy was only possible in the limited energy range of $1\,\mathrm{V}$ to $-1\,\mathrm{V}$ where no molecular features were visible. Higher bias voltages could not be probed because of the aforementioned mobility of the molecules that impacted the stability of the system under higher bias voltages.

Most interestingly, we succeeded in anchoring single CF_3-3P-S(H) molecules to deliberately created single S-vacancies in the uppermost S-layer of MoS_2. These anchored molecules rotate around one end, forming a strong bond with the defect. We identified two different species of these anchored molecules that differ only in their electronic structure: one exhibits a resonance at zero bias, which we assume to be a Kondo resonance, and the other does not. Through a collaboration with M. Rossi and D. Maksimov we identified these two species using *ab-initio* molecular dynamics simulations, DFT calculations and stability analyses: the more abundant species without the Kondo resonance is the intact CF_3-3P-SH molecule, while the other is the dehydrogenated CF_3-3P-S. Both anchor and create an in-gap state inside the bandgap of MoS_2 that is mostly localised at the anchoring point, but only the latter is singly occupied through the interaction with the Au(111) surface's electron reservoir and can thus give rise to a Kondo resonance. By combining our experimental findings with theory, we could therefore disentangle the anchoring process at an atomic level.

In the next part, we have shown the strength of MoS_2/Au(111) as a decoupling layer that allows for detailed investigation of molecular states such as the successfully deposited

single VONc molecules. While STM topography did not allow for the identification of the direction of the molecule's VO-bond, we analysed the electronic structure of the physisorbed VONc molecule in detail: We identified the highest occupied molecular orbital (HOMO) of the molecule as a sharp peak inside the bandgap of MoS_2 at $\sim -500\,\mathrm{mV}$ which shifts in energy when moving across the molecule. This shift was determined to be caused by the tip-perturbation potential. Additionally, the distribution and lineshapes of the vibronic peaks change severely depending on the position on the molecule which was identified and modelled theoretically to be the effect of vibration-assisted tunnelling. All these findings rely on the enhanced lifetime of the molecular and vibronic states which gives us the energy resolution needed to observe the investigated effects.

In the last part of this thesis, we have explored the bulk 2D-semiconductor 2H-$MoTe_2$ as a possible substrate for STM. After successfully contacting the material to allow for STM measurements that require slightly elevated measurement temperatures, we have performed an initial characterisation of the material: Electronically, $MoTe_2$ shows a bandgap of about 2.5 V to 3 V at the *Gamma* point, where the precise identification of the conduction band maximum and valence band minimum still require other measurements such as κ-sensitive measurements. Additionally, we identified $MoTe_2$ as an intrinsic n-type semiconductor from the alignment of the bandgap with the Fermi energy in $\mathrm{d}I/\mathrm{d}V$ spectra.

Topographically, we have observed multiple differently appearing inherent defects that show states inside the bandgap of $MoTe_2$. The spatial distribution of these states have been imaged using $\mathrm{d}I/\mathrm{d}V$ maps, which would allow for future identification of these defects with the help of DFT calculations, combined with e. g. AFM.

Lastly, we attempted to deposit molecular evaporants with opposite characteristics in electron affinity/ionisation potential: the electron acceptor molecule F_4-TCNQ and the electron donor molecule TTF. We found that only the electron donor TTF could successfully physisorb on $MoTe_2$, possibly exhibiting charge transfer with the substrate.

To conclude, when trying to design new systems with combined materials, there is a staggering amount of possibilities. This requires quite some forethought when choosing materials, organic molecules and semiconducting substrates in this case, because the properties of both have to be specifically tailored to one another. Be it the choice of a thiol-based molecule to anchor to purposefully created S-defects as in Chapter 4, the choice of MoS_2 as a decoupling layer combined with the geometrically very stable VONc molecules in Chapter 5, or the combination of the n-type semiconductor $MoTe_2$ with the electron donor TTF in Chapter 6, having complementary properties is crucial for the successful creation of hybrid systems. But while careful selection of materials based upon theoretical results or different experimental contexts gives a much needed headstart, in the end, only the final experiment will show how the resulting interaction truly is.

References

[1] G. Binnig, H. Rohrer et al. 'Surface Studies by Scanning Tunneling Microscopy'. In: *Phys. Rev. Lett.* 49.1 (July 1982), pp. 57–61. DOI: 10.1103/PhysRevLett.49.57 (cit. on p. 5).

[2] G. Binnig, H. Rohrer et al. 'Tunneling Through a Controllable Vacuum Gap'. In: *Applied Physics Letters* 40.2 (1982), pp. 178–180. DOI: 10.1063/1.92999 (cit. on p. 5).

[3] P. K. Hansma and J. Tersoff. 'Scanning tunneling microscopy'. In: *Journal of Applied Physics* 61.2 (Jan. 1987), R1–R24. DOI: 10.1063/1.338189 (cit. on p. 5).

[4] Nobelprize.org. *The Nobel Prize in Physics 1986*. Nobel Media AB. 2018. URL: https://www.nobelprize.org/prizes/physics/1986/summary/ (visited on 26/10/2018) (cit. on p. 5).

[5] J. Tersoff and D. R. Hamann. 'Theory and Application for the Scanning Tunneling Microscope'. In: *Phys. Rev. Lett.* 50.25 (June 1983), pp. 1998–2001. DOI: 10.1103/PhysRevLett.50.1998 (cit. on pp. 5, 7–9).

[6] I. Giaever and K. Megerle. 'Study of Superconductors by Electron Tunneling'. In: *Phys. Rev.* 122.4 (May 1961), pp. 1101–1111. DOI: 10.1103/PhysRev.122.1101 (cit. on p. 7).

[7] J. Bardeen. 'Tunnelling from a Many-Particle Point of View'. In: *Phys. Rev. Lett.* 6.2 (Jan. 1961), pp. 57–59. DOI: 10.1103/PhysRevLett.6.57 (cit. on p. 8).

[8] C. J. Chen. 'Theory of scanning tunneling spectroscopy'. In: *Journal of Vacuum Science & Technology A* 6.2 (Mar. 1988), pp. 319–322. DOI: 10.1116/1.575444 (cit. on p. 8).

[9] C. J. Chen. 'Tunneling matrix elements in three-dimensional space: The derivative rule and the sum rule'. In: *Phys. Rev. B* 42.14 (Nov. 1990), pp. 8841–8857. DOI: 10.1103/PhysRevB.42.8841 (cit. on p. 8).

[10] L. Gross, N. Moll et al. 'High-Resolution Molecular Orbital Imaging Using a *p*-Wave STM Tip'. In: *Phys. Rev. Lett.* 107.8 (Aug. 2011), p. 086101. DOI: 10.1103/PhysRevLett.107.086101 (cit. on p. 8).

[11] H. J. Zandvliet and A. van Houselt. 'Scanning Tunneling Spectroscopy'. In: *Annual Review of Analytical Chemistry* 2.1 (2009). PMID: 20636053, pp. 37–55. DOI: 10.1146/annurev-anchem-060908-155213 (cit. on p. 9).

[12] M. Tinkham. *Introduction to Superconductivity*. McGraw-Hill Kogakusha, 1975 (cit. on p. 11).

[13] M. Ruby, F. Pientka et al. 'Tunneling Processes into Localized Subgap States in Superconductors'. In: *Phys. Rev. Lett.* 115.8 (Aug. 2015), p. 087001. DOI: 10.1103/PhysRevLett.115.087001 (cit. on p. 11).

[14] Stanford Research Systems. *About Lock-In Amplifiers*. Stanford Research Systems. 2004. URL: https://thinksrs.com/downloads/pdfs/applicationnotes/AboutLIAs.pdf (visited on 21/04/2023) (cit. on pp. 11, 12).

[15] W. G. Dawson and D. W. Bullett. 'Electronic structure and crystallography of $MoTe_2$ and WTe_2'. In: *Journal of Physics C: Solid State Physics* 20.36 (1987). PMID: 20636053, p. 6159. DOI: 10.1088/0022-3719/20/36/017 (cit. on p. 13).

[16] M. V. Berry and A. K. Geim. 'Of flying frogs and levitrons'. In: *European Journal of Physics* 18.4 (July 1997), p. 307. DOI: 10.1088/0143-0807/18/4/012 (cit. on p. 13).

[17] Nobelprize.org. *The Nobel Prize in Physics 2010 – Press release*. Nobel Media AB. 2023. URL: https://www.nobelprize.org/prizes/physics/2010/press-release/ (visited on 17/08/2023) (cit. on p. 13).

[18] K. S. Novoselov, A. K. Geim et al. 'Electric Field Effect in Atomically Thin Carbon Films'. In: *Science* 306.5696 (2004), pp. 666–669. DOI: 10.1126/science.1102896 (cit. on p. 13).

[19] K. F. Mak, C. Lee et al. 'Atomically Thin MoS_2: A New Direct-Gap Semiconductor'. In: *Phys. Rev. Lett.* 105.13 (2010), p. 136805. DOI: 10.1103/PhysRevLett.105.136805 (cit. on p. 13).

[20] S. Song, D. H. Keum et al. 'Room Temperature Semiconductor–Metal Transition of $MoTe_2$ Thin Films Engineered by Strain'. In: *Nano Letters* 16.1 (2016), pp. 188–193. DOI: 10.1021/acs.nanolett.5b03481 (cit. on pp. 13, 20).

[21] K. S. Novoselov, A. Mishchenko et al. '2D materials and van der Waals heterostructures'. In: *Science* 353.6298 (2016), aac9439. DOI: 10.1126/science.aac9439 (cit. on p. 13).

[22] N. Lu, H. Guo et al. 'Twisted MX_2/MoS_2 heterobilayers: effect of van der Waals interaction on the electronic structure'. In: *Nanoscale* 9.48 (2017), pp. 19131–19138. DOI: 10.1039/C7NR07746G (cit. on p. 13).

[23] A. De Sanctis, I. Amit et al. 'Strain-engineered inverse charge-funnelling in layered semiconductors'. In: *Nature Communications* 9.1 (2018), p. 1652. DOI: 10.1038/s41467-018-04099-7 (cit. on p. 13).

[24] Y. L. Huang, Y. J. Zheng et al. 'The organic-2D transition metal dichalcogenide heterointerface'. In: *Chem. Soc. Rev.* 47.9 (2018), pp. 3241–3264. DOI: 10.1039/C8CS00159F (cit. on pp. 13, 43).

[25] S. Bertolazzi, M. Gobbi et al. 'Molecular chemistry approaches for tuning the properties of two-dimensional transition metal dichalcogenides'. In: *Chem. Soc. Rev.* 47.17 (2018), pp. 6845–6888. DOI: 10.1039/C8CS00169C (cit. on pp. 13, 43).

[26] L. Daukiya, J. Seibel and S. D. Feyter. 'Chemical modification of 2D materials using molecules and assemblies of molecules'. In: *Advances in Physics: X* 4.1 (2019), p. 1625723. DOI: 10.1080/23746149.2019.1625723 (cit. on pp. 13, 43).

[27] M. Amani, D.-H. Lien et al. 'Near-unity photoluminescence quantum yield in MoS_2'. In: *Science* 350.6264 (2015), pp. 1065–1068. DOI: 10.1126/science.aad2114 (cit. on p. 13).

[28] A. Chaves, J. G. Azadani et al. 'Bandgap engineering of two-dimensional semiconductor materials'. In: *npj 2D Materials and Applications* 4.1 (2020), p. 29. DOI: 10.1038/s41699-020-00162-4 (cit. on pp. 13, 14, 16, 20).

[29] Q. H. Wang, K. Kalantar-zadeh et al. 'Electronics and Optoelectronics of Two-Dimensional Transition Metal Dichalcogenides'. In: *Nature Nanotech.* 7 (Nov. 2012), pp. 699–712. DOI: 10.1038/nnano.2012.193 (cit. on p. 13).

[30] K. Nassiri Nazif, A. Daus et al. 'High-specific-power flexible transition metal dichalcogenide solar cells'. In: *Nature Communications* 12.1 (2021), p. 7034. DOI: 10.1038/s41467-021-27195-7 (cit. on p. 13).

[31] K.-A. N. Duerloo, M. T. Ong and E. J. Reed. 'Intrinsic Piezoelectricity in Two-Dimensional Materials'. In: *The Journal of Physical Chemistry Letters* 3.19 (2012), pp. 2871–2876. DOI: 10.1021/jz3012436 (cit. on p. 13).

[32] H. Li, Z. Yin et al. 'Fabrication of Single- and Multilayer MoS_2 Film-Based Field-Effect Transistors for Sensing NO at Room Temperature'. In: *Small* 8.1 (2012), pp. 63–67. DOI: https://doi.org/10.1002/smll.201101016 (cit. on pp. 13, 43).

[33] P. Fathi-Hafshejani, N. Azam et al. 'Two-Dimensional-Material-Based Field-Effect Transistor Biosensor for Detecting COVID-19 Virus (SARS-CoV-2)'. In: *ACS Nano* 15.7 (2021), pp. 11461–11469. DOI: 10.1021/acsnano.1c01188 (cit. on pp. 13, 43).

[34] B. Radisavljevic, M. B. Whitwick and A. Kis. 'Integrated Circuits and Logic Operations Based on Single-Layer MoS2'. In: *ACS Nano* 5.12 (2011), pp. 9934–9938. DOI: 10.1021/nn203715c (cit. on p. 13).

[35] J. Wilson and A. Yoffe. 'The transition metal dichalcogenides discussion and interpretation of the observed optical, electrical and structural properties'. In: *Advances in Physics* 18.73 (1969), pp. 193–335. DOI: 10.1080/00018736900101307 (cit. on pp. 14, 16, 20).

[36] E. Salje. 'Polytypism in Crystals'. In: *Encyclopedia of Materials: Science and Technology*. Ed. by K. J. Buschow, R. W. Cahn et al. Oxford: Elsevier, 2001, pp. 7744–7746. DOI: 10.1016/B0-08-043152-6/01391-7 (cit. on p. 14).

[37] D. Voiry, A. Mohite and M. Chhowalla. 'Phase engineering of transition metal dichalcogenides'. In: *Chem. Soc. Rev.* 44.9 (2015), pp. 2702–2712. DOI: 10.1039/C5CS00151J (cit. on p. 14).

[38] Y. Deng, X. Zhao et al. '$MoTe_2$: Semiconductor or Semimetal?' In: *ACS Nano* 15.8 (2021), pp. 12465–12474. DOI: 10.1021/acsnano.1c01816 (cit. on p. 14).

[39] D. Yang, S. J. Sandoval et al. 'Structure of single-molecular-layer MoS_2'. In: *Phys. Rev. B* 43.14 (May 1991), pp. 12053–12056. DOI: 10.1103/PhysRevB.43.12053 (cit. on p. 16).

[40] S. M. Shinde, K. P. Dhakal et al. 'Stacking-controllable interlayer coupling and symmetric configuration of multilayered MoS_2'. In: *NPG Asia Materials* 10.2 (Feb. 2018), e468. DOI: 10.1038/am.2017.226 (cit. on p. 16).

[41] K. K. Kam and B. A. Parkinson. 'Detailed photocurrent spectroscopy of the semiconducting group VIB transition metal dichalcogenides'. In: *The Journal of Physical Chemistry* 86.4 (1982), pp. 463–467. DOI: 10.1021/j100393a010 (cit. on pp. 16, 85).

[42] T. Cheiwchanchamnangij and W. R. L. Lambrecht. 'Quasiparticle band structure calculation of monolayer, bilayer, and bulk MoS_2'. In: *Phys. Rev. B* 85.20 (May 2012), p. 205302. DOI: 10.1103/PhysRevB.85.205302 (cit. on p. 16).

[43] A. Splendiani, L. Sun et al. 'Emerging Photoluminescence in Monolayer MoS_2'. In: *Nano Letters* 10.4 (2010), pp. 1271–1275. DOI: 10.1021/nl903868w (cit. on pp. 16, 17).

[44] N. Krane, C. Lotze and K. J. Franke. 'Moiré structure of MoS_2 on Au(111): Local structural and electronic properties'. In: *Surface Science* 678 (2018). Surface Structure and Dynamics in Honor of Karl-Heinz Rieder, pp. 136–142. DOI: 10.1016/j.susc.2018.03.015 (cit. on pp. 16–19).

[45] S. Trishin, C. Lotze et al. 'Moiré Tuning of Spin Excitations: Individual Fe Atoms on MoS_2/Au(111)'. In: *Phys. Rev. Lett.* 127.23 (Nov. 2021), p. 236801. DOI: 10.1103/PhysRevLett.127.236801 (cit. on pp. 16, 17, 60).

[46] S. G. Sørensen, H. G. Füchtbauer et al. 'Structure and Electronic Properties of In Situ Synthesized Single-Layer MoS_2 on a Gold Surface'. In: *ACS Nano* 8.7 (2014). PMID: 24938884, pp. 6788–6796. DOI: 10.1021/nn502812n (cit. on p. 16).

[47] F. Tumino, C. S. Casari et al. 'Nature of Point Defects in Single-Layer MoS_2 Supported on Au(111)'. In: *The Journal of Physical Chemistry C* 124.23 (2020), pp. 12424–12431. DOI: 10.1021/acs.jpcc.0c01477 (cit. on pp. 17, 19).

[48] A. Bruix, J. A. Miwa et al. 'Single-layer MoS_2 on Au(111): Band gap renormalization and substrate interaction'. In: *Phys. Rev. B* 93.16 (Apr. 2016), p. 165422. DOI: 10.1103/PhysRevB.93.165422 (cit. on pp. 17, 19).

[49] C. Zhang, Y. Chen et al. 'Probing Critical Point Energies of Transition Metal Dichalcogenides: Surprising Indirect Gap of Single Layer WSe_2'. In: *Nano Letters* 15.10 (2015). PMID: 26389585, pp. 6494–6500. DOI: 10.1021/acs.nanolett.5b01968 (cit. on p. 18).

[50] C. Muratore, J. J. Hu et al. 'Continuous ultra-thin MoS_2 films grown by low-temperature physical vapor deposition'. In: *Applied Physics Letters* 104.26 (July 2014), p. 261604. DOI: 10.1063/1.4885391 (cit. on p. 20).

[51] E. Pollmann, J. M. Morbec et al. 'Molybdenum Disulfide Nanoflakes Grown by Chemical Vapor Deposition on Graphite: Nucleation, Orientation, and Charge Transfer'. In: *The Journal of Physical Chemistry C* 124.4 (2020), pp. 2689–2697. DOI: 10.1021/acs.jpcc.9b10120 (cit. on p. 20).

[52] H. Bergeron, V. K. Sangwan et al. 'Chemical vapor deposition of monolayer MoS_2 directly on ultrathin Al_2O_3 for low-power electronics'. In: *Applied Physics Letters* 110.5 (Jan. 2017), p. 053101. DOI: 10.1063/1.4975064 (cit. on p. 20).

[53] X. Xu, Z. Lou et al. 'Van der Waals organic/inorganic heterostructures in the two-dimensional limit'. In: *Chem* 7.11 (2021), pp. 2989–3026. DOI: 10.1016/j.chempr.2021.08.013 (cit. on p. 20).

[54] E. Pollmann, P. Ernst et al. 'Ion-mediated growth of ultra thin molybdenum disulfide layers on highly oriented pyrolytic graphite'. In: *Surface and Coatings Technology* 349 (2018), pp. 783–786. DOI: 10.1016/j.surfcoat.2018.05.031 (cit. on p. 20).

[55] N. Krane, C. Lotze et al. 'Electronic Structure and Luminescence of Quasi-Freestanding MoS_2 Nanopatches on Au(111)'. In: *Nano Letters* 16.8 (2016). PMID: 27459588, pp. 5163–5168. DOI: 10.1021/acs.nanolett.6b02101 (cit. on p. 20).

[56] S. Trishin, C. Lotze et al. 'Electronic and magnetic properties of single chalcogen vacancies in MoS_2/Au(111)'. In: *Phys. Rev. B* 108.16 (Oct. 2023), p. 165414. DOI: 10.1103/PhysRevB.108.165414 (cit. on pp. 20, 43, 87).

[57] A. Akkoush, Y. Litman and M. Rossi. 'A Hybrid-Density Functional Theory Study of Intrinsic Point Defects in MX_2 (M=Mo,W; X=S,Se) Monolayers'. In: *phys. stat. sol. (a)* (2023), p. 2300180. DOI: 10.1002/pssa.202300180 (cit. on pp. 20, 43, 57).

[58] D. Puotinen and R. E. Newnham. 'The crystal structure of $MoTe_2$'. In: *Acta Crystallographica* 14.6 (June 1961), pp. 691–692. DOI: 10.1107/S0365110X61002084 (cit. on p. 20).

[59] B. E. Brown. 'The crystal structures of WTe_2 and high-temperature $MoTe_2$'. In: *Acta Crystallographica* 20.2 (1966), pp. 268–274. DOI: 10.1107/S0365110X66000513 (cit. on p. 20).

[60] N. V. Podberezskaya, S. A. Magarill et al. 'Crystal Chemistry of Dichalcogenides MX_2'. In: *Journal of Structural Chemistry* 42.4 (2001), pp. 1573–8779. DOI: 10.1023/A:1013106329156 (cit. on p. 20).

[61] J. P. Fraser, L. Masaityte et al. 'Selective phase growth and precise-layer control in $MoTe_2$'. In: *Communications Materials* 1.1 (2020), pp. 2662–4443. DOI: 10.1038/s43246-020-00048-4 (cit. on p. 20).

[62] Y. Sun, Y. Wang et al. 'Low-Temperature Solution Synthesis of Few-Layer 1T'-$MoTe_2$ Nanostructures Exhibiting Lattice Compression'. In: *Angewandte Chemie International Edition* 55.8 (2016), pp. 2830–2834. DOI: https://doi.org/10.1002/anie.201510029 (cit. on p. 20).

[63] Y. Wang, J. Xiao et al. 'Structural phase transition in monolayer $MoTe_2$ driven by electrostatic doping'. In: *Nature* 550.7677 (2017), pp. 487–491. DOI: 10.1038/nature24043 (cit. on p. 20).

[64] R. Maiti, M. A. S. R. Saadi et al. 'Strain-Induced Spatially Resolved Charge Transport in 2H-$MoTe_2$'. In: *ACS Applied Electronic Materials* 3.9 (2021), pp. 3781–3788. DOI: 10.1021/acsaelm.1c00281 (cit. on p. 20).

[65] K. Deng, G. Wan et al. 'Experimental observation of topological Fermi arcs in type-II Weyl semimetal $MoTe_2$'. In: *Nature Physics* 12.12 (2016), pp. 1105–1110. DOI: 10.1038/nphys3871 (cit. on p. 20).

[66] J. Jiang, Z. Liu et al. 'Signature of type-II Weyl semimetal phase in $MoTe_2$'. In: *Nature Communications* 8.1 (2017), p. 13973. DOI: 10.1038/ncomms13973 (cit. on p. 20).

[67] Y. Qi, P. G. Naumov et al. 'Superconductivity in Weyl semimetal candidate $MoTe_2$'. In: *Nature Communications* 7.1 (2016), p. 11038. DOI: 10.1038/ncomms11038 (cit. on p. 20).

[68] A. Jindal, A. Saha et al. 'Coupled ferroelectricity and superconductivity in bilayer T_d-$MoTe_2$'. In: *Nature* 613.7942 (2023), pp. 48–52. DOI: 10.1038/s41586-022-05521-3 (cit. on p. 20).

[69] J. Seok, J.-H. Lee et al. 'Active hydrogen evolution through lattice distortion in metallic $MoTe_2$'. In: *2D Materials* 4.2 (June 2017), p. 025061. DOI: 10.1088/2053-1583/aa659d (cit. on p. 20).

[70] L. Dong, G.-Y. Wang et al. 'Charge Density Wave States in 2H-$MoTe_2$ Revealed by Scanning Tunneling Microscopy'. In: *Chinese Physics Letters* 35.6 (June 2018), p. 066801. DOI: 10.1088/0256-307X/35/6/066801 (cit. on p. 20).

[71] A. J. Grant, T. M. Griffiths et al. 'The electrical properties and the magnitude of the indirect gap in the semiconducting transition metal dichalcogenide layer crystals'. In: *Journal of Physics C: Solid State Physics* 8.1 (Jan. 1975), p. L17. DOI: 10.1088/0022-3719/8/1/004 (cit. on pp. 20, 85, 87).

[72] A. Conan, D. Delaunay et al. 'Temperature dependence of the electrical conductivity and thermoelectric power in $MoTe_2$ single crystals'. In: *physica status solidi (b)* 94.1 (1979), pp. 279–286. DOI: https://doi.org/10.1002/pssb.2220940132 (cit. on pp. 20, 85, 87).

[73] A. Arora, M. Drüppel et al. 'Interlayer excitons in a bulk van der Waals semiconductor'. In: *Nature Communications* 8.1 (2017), p. 639. DOI: 10.1038/s41467-017-00691-5 (cit. on pp. 20, 21, 86).

[74] R. Oliva, T. Woźniak et al. 'Hidden spin-polarized bands in semiconducting 2H-$MoTe_2$'. In: *Materials Research Letters* 8.2 (2020), pp. 75–81. DOI: 10.1080/21663831.2019.1702113 (cit. on p. 20).

[75] G. G. Macfarlane, T. P. McLean et al. 'Fine Structure in the Absorption-Edge Spectrum of Si'. In: *Phys. Rev.* 111 (5 Sept. 1958), pp. 1245–1254. DOI: 10.1103/PhysRev.111.1245 (cit. on p. 20).

[76] W. Bludau, A. Onton and W. Heinke. 'Temperature dependence of the band gap of silicon'. In: *Journal of Applied Physics* 45.4 (Apr. 1974), pp. 1846–1848. DOI: 10.1063/1.1663501 (cit. on p. 20).

[77] Y.-Q. Bie, G. Grosso et al. 'A $MoTe_2$-based light-emitting diode and photodetector for silicon photonic integrated circuits'. In: *Nature Nanotechnology* 12.12 (2017), pp. 1124–1129. DOI: 10.1038/nnano.2017.209 (cit. on p. 20).

[78] C. Ruppert, B. Aslan and T. F. Heinz. 'Optical Properties and Band Gap of Single- and Few-Layer $MoTe_2$ Crystals'. In: *Nano Letters* 14.11 (2014). PMID: 25302768, pp. 6231–6236. DOI: 10.1021/nl502557g (cit. on p. 21).

[79] I. G. Lezama, A. Arora et al. 'Indirect-to-Direct Band Gap Crossover in Few-Layer $MoTe_2$'. In: *Nano Letters* 15.4 (2015). PMID: 25803208, pp. 2336–2342. DOI: 10.1021/nl5045007 (cit. on p. 21).

[80] R. Sankar, G. Narsinga Rao et al. 'Polymorphic Layered $MoTe_2$ from Semiconductor, Topological Insulator, to Weyl Semimetal'. In: *Chemistry of Materials* 29.2 (2017), pp. 699–707. DOI: 10.1021/acs.chemmater.6b04363 (cit. on pp. 21, 87, 88).

[81] P. M. Coelho, H.-P. Komsa et al. 'Room-Temperature Ferromagnetism in $MoTe_2$ by Post-Growth Incorporation of Vanadium Impurities'. In: *Advanced Electronic Materials* 5.5 (2019), p. 1900044. DOI: 10.1002/aelm.201900044 (cit. on pp. 21, 87, 88).

[82] Z. Guguchia, A. Kerelsky et al. 'Magnetism in semiconducting molybdenum dichalcogenides'. In: *Science Advances* 4.12 (2018), eaat3672. DOI: 10.1126/sciadv.aat3672 (cit. on pp. 21, 88).

[83] P. M. Coelho, H.-P. Komsa et al. 'Post-Synthesis Modifications of Two-Dimensional $MoSe_2$ or $MoTe_2$ by Incorporation of Excess Metal Atoms into the Crystal Structure'. In: *ACS Nano* 12.4 (2018), pp. 3975–3984. DOI: 10.1021/acsnano.8b01580 (cit. on pp. 21, 88).

[84] F. Rosei, M. Schunack et al. 'Properties of large organic molecules on metal surfaces'. In: *Progress in Surface Science* 71.5 (2003). Proceedings of the IXth Symposium on Surface Physics, Trest Castle 2002, pp. 95–146. DOI: 10.1016/S0079-6816(03)00004-2 (cit. on p. 22).

[85] N. Krane, C. Lotze et al. 'High-Resolution Vibronic Spectra of Molecules on Molybdenum Disulfide Allow for Rotamer Identification'. In: *ACS Nano* 12.11 (2018), pp. 11698–11703. DOI: 10.1021/acsnano.8b07414 (cit. on pp. 22, 28, 29, 45, 79).

[86] S. Park, T. Schultz et al. 'Demonstration of the key substrate-dependent charge transfer mechanisms between monolayer MoS_2 and molecular dopants'. In: *Commun. Phys.* 92 (1 2019), p. 109. DOI: 10.1038/s42005-019-0212-y (cit. on pp. 23, 43).

[87] I. Fernandez-Torrente, S. Monturet et al. 'Long-Range Repulsive Interaction between Molecules on a Metal Surface Induced by Charge Transfer'. In: *Phys. Rev. Lett.* 99.17 (Oct. 2007), p. 176103. DOI: 10.1103/PhysRevLett.99.176103 (cit. on pp. 23, 95, 96).

[88] S. Braun, W. R. Salaneck and M. Fahlman. 'Energy-Level Alignment at Organic/Metal and Organic/Organic Interfaces'. In: *Advanced Materials* 21.14-15 (2009), pp. 1450–1472. DOI: 10.1002/adma.200802893 (cit. on p. 23).

[89] D. A. Kunkel, J. Hooper et al. 'Self-assembly of strongly dipolar molecules on metal surfaces'. In: *The Journal of Chemical Physics* 142.10 (Feb. 2015), p. 101921. DOI: 10.1063/1.4907943 (cit. on p. 23).

[90] L.-L. Wang and H.-P. Cheng. 'Density functional study of the adsorption of a C_{60} monolayer on Ag(111) and Au(111) surfaces'. In: *Phys. Rev. B* 69.16 (Apr. 2004), p. 165417. DOI: 10.1103/PhysRevB.69.165417 (cit. on p. 23).

[91] N. Krane, C. Lotze et al. 'Mapping the perturbation potential of metallic and dipolar tips in tunneling spectroscopy on MoS_2'. In: *Phys. Rev. B* 100.3 (July 2019), p. 035410. DOI: 10.1103/PhysRevB.100.035410 (cit. on pp. 25, 26, 70, 74).

[92] G. V. Nazin, S. W. Wu and W. Ho. 'Tunneling rates in electron transport through double-barrier molecular junctions in a scanning tunneling microscope'. In: *Proceedings of the National Academy of Sciences* 102.25 (2005), pp. 8832–8837. DOI: 10.1073/pnas.0501171102 (cit. on p. 26).

[93] J. Franck and E. G. Dymond. 'Elementary processes of photochemical reactions'. In: *Trans. Faraday Soc.* 21 (February 1926), pp. 536–542. DOI: 10.1039/TF9262100536 (cit. on p. 26).

[94] E. Condon. 'A Theory of Intensity Distribution in Band Systems'. In: *Phys. Rev.* 28.6 (Dec. 1926), pp. 1182–1201. DOI: 10.1103/PhysRev.28.1182 (cit. on p. 26).

[95] C. Hill. *The harmonic oscillator wavefunctions*. 2019. URL: https://scipython.com/blog/the-harmonic-oscillator-wavefunctions/ (visited on 15/02/2024) (cit. on p. 27).

[96] P. Atkins and R. Friedman. *Molecular Quantum Dynamics*. Fourth Edition. Oxford University Press, 2005. URL: https://web.stanford.edu/~oas/SI/QM/Atkins05.pdf (cit. on pp. 26–28).

[97] E. B. Wilson, J. C. Decius and P. C. Cross. *Molecular Vibrations: The Theory of Infrared and Raman Vibrational Spectra*. eng. London: McGraw-Hill, 1955 (cit. on pp. 27, 29).

[98] B. Doppagne, M. C. Chong et al. 'Electrofluorochromism at the single-molecule level'. In: *Science* 361.6399 (2018), pp. 251–255. DOI: 10.1126/science.aat1603 (cit. on pp. 28, 68).

[99] M. Sakurai, C. Thirstrup and M. Aono. 'New aspects of light emission from STM'. In: *Applied Physics A* 80.6 (2005), pp. 1153–1160. DOI: 10.1007/s00339-004-3180-2 (cit. on p. 28).

[100] J. W. Gadzuk. 'Inelastic resonance scattering, tunneling, and desorption'. In: *Phys. Rev. B* 44.24 (Dec. 1991), pp. 13466–13477. DOI: 10.1103/PhysRevB.44.13466 (cit. on p. 28).

[101] K. Huang, A. Rhys and N. F. Mott. 'Theory of light absorption and non-radiative transitions in *F*-centres'. In: *Proceedings of the Royal Society of London. Series A. Mathematical and Physical Sciences* 204.1078 (1950), pp. 406–423. DOI: 10.1098/rspa.1950.0184 (cit. on p. 29).

[102] N. Pavliček, I. Swart et al. 'Symmetry Dependence of Vibration-Assisted Tunneling'. In: *Phys. Rev. Lett.* 110.13 (Mar. 2013), p. 136101. DOI: 10.1103/PhysRevLett.110.136101 (cit. on pp. 29, 52, 79).

[103] G. Reecht, N. Krane et al. 'Vibrational Excitation Mechanism in Tunneling Spectroscopy beyond the Franck-Condon Model'. In: *Phys. Rev. Lett.* 124.11 (Mar. 2020), p. 116804. DOI: 10.1103/PhysRevLett.124.116804 (cit. on pp. 29, 30, 79, 80).

[104] A. C. Hewson. *The Kondo Problem to Heavy Fermions*. Cambridge Studies in Magnetism. Cambridge University Press, 1993. DOI: 10.1017/CBO9780511470752 (cit. on pp. 31–33).

[105] A. H. Nevidomskyy. 'The Kondo Model and Poor Man's Scaling'. In: *Many-Body Physics: From Kondo to Hubbard*. Ed. by E. Pavarini, E. Koch and P. Coleman. Schriften des Forschungszentrums Jülich, Reihe Modeling and Simulation 5. Forschungszentrum Jülich GmbH, Institute for Advanced Simulation, 2015. URL: https://www.cond-mat.de/events/correl15/manuscripts/nevidomskyy.pdf (cit. on p. 31).

[106] E. Pavarini, E. Koch and P. Coleman, eds. *Many-Body Physics: From Kondo to Hubbard*. Schriften des Forschungszentrums Jülich, Reihe Modeling and Simulation 5. Forschungszentrum Jülich GmbH, Institute for Advanced Simulation, 2015. URL: https://www.cond-mat.de/events/correl15/manuscripts/ (cit. on p. 31).

[107] J. Friedel. 'On Some Electrical and Magnetic Properties of Metallic Solid Solutions'. In: *Canadian Journal of Physics* 34.12A (1956), pp. 1190–1211. DOI: 10.1139/p56-134 (cit. on p. 31).

[108] W. De Haas, H. Casimir and G. Van Den Berg. 'The electrical resistance of gold below 1 °K'. In: *Physica* 5.4 (1938), pp. 225–229. DOI: https://doi.org/10.1016/S0031-8914(38)80079-3 (cit. on p. 31).

[109] P. W. Anderson. 'Localized Magnetic States in Metals'. In: *Phys. Rev.* 124.1 (Oct. 1961), pp. 41–53. DOI: 10.1103/PhysRev.124.41 (cit. on p. 31).

[110] J. Kondo. 'Resistance Minimum in Dilute Magnetic Alloys'. In: *Progress of Theoretical Physics* 32.1 (July 1964), pp. 37–49. DOI: 10.1143/PTP.32.37 (cit. on p. 31).

[111] J. R. Schrieffer and P. A. Wolff. 'Relation between the Anderson and Kondo Hamiltonians'. In: *Phys. Rev.* 149.2 (Sept. 1966), pp. 491–492. DOI: 10.1103/PhysRev.149.491 (cit. on p. 32).

[112] L. Farinacci. 'Tuning the Interactions of Magnetic Molecules on a Superconductor'. PhD thesis. Freie Universität Berlin, 2019. DOI: 10.17169/refubium-27604 (cit. on p. 32).

[113] L. Kouwenhoven and L. Glazman. 'Revival of the Kondo effect'. In: *Physics World* 14.1 (Jan. 2001), p. 33. DOI: 10.1088/2058-7058/14/1/28 (cit. on p. 32).

[114] P. W. Anderson. 'A poor man's derivation of scaling laws for the Kondo problem'. In: *Journal of Physics C: Solid State Physics* 3.12 (Dec. 1970), p. 2436. DOI: 10.1088/0022-3719/3/12/008 (cit. on p. 32).

[115] Nobelprize.org. *The Nobel Prize in Physics 1982 – Press release*. Nobel Media AB. 2023. URL: https://www.nobelprize.org/prizes/physics/1982/press-release/ (visited on 10/10/2023) (cit. on p. 32).

[116] N. Andrei. 'Diagonalization of the Kondo Hamiltonian'. In: *Phys. Rev. Lett.* 45.5 (Aug. 1980), pp. 379–382. DOI: 10.1103/PhysRevLett.45.379 (cit. on p. 33).

[117] P. B. Wiegmann. 'Exact solution of the s-d exchange model (Kondo problem)'. In: *Journal of Physics C: Solid State Physics* 14.10 (Apr. 1981), p. 1463. DOI: 10.1088/0022-3719/14/10/014 (cit. on p. 33).

[118] S. Doniach. 'The Kondo lattice and weak antiferromagnetism'. In: *Physica B+C* 91 (1977), pp. 231–234. DOI: 10.1016/0378-4363(77)90190-5 (cit. on p. 33).

[119] Y.-f. Yang, Z. Fisk et al. 'Scaling the Kondo lattice'. In: *Nature* 454.7204 (2008), pp. 611–613. DOI: 10.1038/nature07157 (cit. on p. 33).

[120] G. R. Stewart. 'Heavy-fermion systems'. In: *Rev. Mod. Phys.* 56.4 (Oct. 1984), pp. 755–787. DOI: 10.1103/RevModPhys.56.755 (cit. on p. 33).

[121] D. K. Morr. 'Theory of scanning tunneling spectroscopy: from Kondo impurities to heavy fermion materials'. In: *Reports on Progress in Physics* 80.1 (2016), p. 014502. DOI: 10.1088/0034-4885/80/1/014502 (cit. on p. 33).

[122] M. Ternes, A. J. Heinrich and W.-D. Schneider. 'Spectroscopic manifestations of the Kondo effect on single adatoms'. In: *Journal of Physics: Condensed Matter* 21.5 (Dec. 2008), p. 053001. DOI: 10.1088/0953-8984/21/5/053001 (cit. on p. 33).

[123] E. Wuilloud, H. R. Moser et al. 'Electronic structure of γ- and α-Ce'. In: *Phys. Rev. B* 28.12 (Dec. 1983), pp. 7354–7357. DOI: 10.1103/PhysRevB.28.7354 (cit. on p. 33).

[124] F. Patthey, B. Delley et al. 'Low-Energy Excitations in α- and γ-Ce Observed by Photoemission'. In: *Phys. Rev. Lett.* 55.14 (Sept. 1985), pp. 1518–1521. DOI: 10.1103/PhysRevLett.55.1518 (cit. on p. 33).

[125] F. Patthey, W.-D. Schneider et al. 'High-temperature collapse of the Kondo resonance in $CeSi_2$ observed by photoemission'. In: *Phys. Rev. Lett.* 58.26 (June 1987), pp. 2810–2813. DOI: 10.1103/PhysRevLett.58.2810 (cit. on p. 33).

[126] J. Li, W.-D. Schneider et al. 'Kondo Scattering Observed at a Single Magnetic Impurity'. In: *Phys. Rev. Lett.* 80.13 (Mar. 1998), pp. 2893–2896. DOI: 10.1103/PhysRevLett.80.2893 (cit. on p. 34).

[127] V. Madhavan, W. Chen et al. 'Tunneling into a Single Magnetic Atom: Spectroscopic Evidence of the Kondo Resonance'. In: *Science* 280.5363 (1998), pp. 567–569. DOI: 10.1126/science.280.5363.567 (cit. on p. 34).

[128] M. Ruby. 'SpectraFox: A free open-source data management and analysis tool for scanning probe microscopy and spectroscopy'. In: *SoftwareX* 5 (2016), pp. 31–36. DOI: 10.1016/j.softx.2016.04.001 (cit. on p. 37).

[129] I. Horcas, R. Fernández et al. 'WSXM: A software for scanning probe microscopy and a tool for nanotechnology'. In: *Review of Scientific Instruments* 78.1 (Jan. 2007), p. 013705. DOI: 10.1063/1.2432410 (cit. on p. 37).

[130] Y.-S. Tremblay-Johnston (underchemist). *nanonispy – A small library written in python 3 to parse Nanonis binary and ascii files.* 2019. URL: https://github.com/underchemist/nanonispy (visited on 07/11/2023) (cit. on p. 37).

[131] W. Chen, V. Madhavan et al. 'Scanning Tunneling Microscopy Observation of an Electronic Superlattice at the Surface of Clean Gold'. In: *Phys. Rev. Lett.* 80.7 (Feb. 1998), pp. 1469–1472. DOI: 10.1103/PhysRevLett.80.1469 (cit. on p. 38).

[132] P. Li and F. Ding. 'Origin of the herringbone reconstruction of Au(111) surface at the atomic scale'. In: *Science Advances* 8.40 (2022), eabq2900. DOI: 10.1126/sciadv.abq2900 (cit. on p. 38).

[133] W. Kaiser and R. Jaklevic. 'Scanning tunneling microscopy study of metals: Spectroscopy and topography'. In: *Surface Science* 181.1 (1987), pp. 55–68. DOI: 10.1016/0039-6028(87)90141-5 (cit. on p. 38).

[134] S. S. Grønborg, S. Ulstrup et al. 'Synthesis of Epitaxial Single-Layer MoS_2 on Au(111)'. In: *Langmuir* 31.35 (2015), pp. 9700–9706. DOI: 10.1021/acs.langmuir.5b02533 (cit. on p. 38).

[135] J. Kang, W. Liu et al. 'Computational Study of Metal Contacts to Monolayer Transition-Metal Dichalcogenide Semiconductors'. In: *Phys. Rev. X* 4 (3 July 2014), p. 031005. DOI: 10.1103/PhysRevX.4.031005 (cit. on p. 40).

[136] A. Allain, J. Kang et al. 'Electrical contacts to two-dimensional semiconductors'. In: *Nature Materials* 14.12 (2015), pp. 1195–1205. DOI: 10.1038/nmat4452 (cit. on p. 40).

[137] Y. Liu, J. Guo et al. 'Approaching the SchottkyMott limit in van der Waals metalsemiconductor junctions'. In: *Nature* 557.7707 (2018), pp. 696–700. DOI: 10.1038/s41586-018-0129-8 (cit. on p. 40).

[138] Y. Wang, J. C. Kim et al. 'Van der Waals contacts between three-dimensional metals and two-dimensional semiconductors'. In: *Nature* 568.7750 (2019), pp. 70–74. DOI: 10.1038/s41586-019-1052-3 (cit. on p. 40).

[139] H. Nan, Z. Wang et al. 'Strong Photoluminescence Enhancement of MoS_2 through Defect Engineering and Oxygen Bonding'. In: *ACS Nano* 8.6 (2014). PMID: 24836121, pp. 5738–5745. DOI: 10.1021/nn500532f (cit. on p. 43).

[140] Z. Lin, B. R. Carvalho et al. 'Defect engineering of two-dimensional transition metal dichalcogenides'. In: *2D Materials* 3.2 (Apr. 2016), p. 022002. DOI: 10.1088/2053-1583/3/2/022002 (cit. on p. 43).

[141] Q. Liang, Q. Zhang et al. 'Defect Engineering of Two-Dimensional Transition-Metal Dichalcogenides: Applications, Challenges, and Opportunities'. In: *ACS Nano* 15.2 (2021). PMID: 33449623, pp. 2165–2181. DOI: 10.1021/acsnano.0c09666 (cit. on p. 43).

[142] S. M. Gali and D. Beljonne. 'Combined healing and doping of transition metal dichalcogenides through molecular functionalization'. In: *J. Mater. Chem. C* 9.45 (2021), pp. 16247–16256. DOI: 10.1039/D1TC01329G (cit. on p. 43).

[143] M. Asadi, K. Kim et al. 'Nanostructured transition metal dichalcogenide electrocatalysts for CO_2 reduction in ionic liquid'. In: *Science* 353 (6298 2016), pp. 467–470. DOI: 10.1126/science.aaf4767 (cit. on p. 43).

[144] K. Cho, M. Min et al. 'Electrical and Optical Characterization of MoS_2 with Sulfur Vacancy Passivation by Treatment with Alkanethiol Molecules'. In: *ACS Nano* 9.8 (2015), pp. 8044–8053. DOI: 10.1021/acsnano.5b04400 (cit. on p. 43).

[145] M. J. Frisch, G. W. Trucks et al. *Gaussian16 Revision B.01*. Gaussian Inc. Wallingford CT. 2016 (cit. on pp. 43, 75).

[146] *Basis sets*. Gaussian, Inc. 2021. URL: https://gaussian.com/basissets/ (visited on 20/03/2024) (cit. on p. 43).

[147] C. Vericat, M. E. Vela et al. 'Self-assembled monolayers of thiols and dithiols on gold: new challenges for a well-known system'. In: *Chem. Soc. Rev.* 39 (5 2010), pp. 1805–1834. DOI: 10.1039/B907301A (cit. on p. 50).

[148] E. Pensa, E. Cortés et al. 'The Chemistry of the Sulfur-Gold Interface: In Search of a Unified Model'. In: *Accounts of Chemical Research* 45.8 (2012). PMID: 22444437, pp. 1183–1192. DOI: 10.1021/ar200260p (cit. on p. 50).

[149] F. Jaroschik. 'Picking One out of Three: Selective Single C-F Activation in Trifluoromethyl Groups'. In: *Chemistry: A European Journal* 24.55 (2018), pp. 14572–14582. DOI: 10.1002/chem.201801702 (cit. on p. 50).

[150] I. Fernández-Torrente, K. J. Franke and J. I. Pascual. 'Vibrational Kondo Effect in Pure Organic Charge-Transfer Assemblies'. In: *Phys. Rev. Lett.* 101.21 (Nov. 2008), p. 217203. DOI: 10.1103/PhysRevLett.101.217203 (cit. on p. 62).

[151] Q. Li, Y. Zhao et al. 'Towards a Comprehensive Understanding of the Reaction Mechanisms Between Defective MoS_2 and Thiol Molecules'. In: *Angewandte Chemie International Edition* 56.35 (2017), pp. 10501–10505. DOI: https://doi.org/10.1002/anie.201706038 (cit. on p. 64).

[152] B. Schuler, D. Y. Qiu et al. 'Large Spin-Orbit Splitting of Deep In-Gap Defect States of Engineered Sulfur Vacancies in Monolayer WS_2'. In: *Phys. Rev. Lett.* 123.7 (2019), p. 076801. DOI: 10.1103/PhysRevLett.123.076801 (cit. on p. 65).

[153] K. Kaiser, L. Gross and F. Schulz. 'A Single-Molecule Chemical Reaction Studied by High-Resolution Atomic Force Microscopy and Scanning Tunneling Microscopy Induced Light Emission'. In: *ACS Nano* 13.6 (2019). PMID: 31184117, pp. 6947–6954. DOI: 10.1021/acsnano.9b01852 (cit. on pp. 67, 70).

[154] L. Malavolti, M. Briganti et al. 'Tunable Spin-Superconductor Coupling of Spin 1/2 Vanadyl Phthalocyanine Molecules'. In: *Nano Letters* 18.12 (2018). PMID: 30452271, pp. 7955–7961. DOI: 10.1021/acs.nanolett.8b03921 (cit. on pp. 67, 70).

[155] C. G. Claessens, U. Hahn and T. Torres. 'Phthalocyanines: From outstanding electronic properties to emerging applications'. In: *The Chemical Record* 8.2 (2008), pp. 75–97. DOI: https://doi.org/10.1002/tcr.20139 (cit. on p. 67).

[156] A. Mugarza, C. Krull et al. 'Spin coupling and relaxation inside molecule-metal contacts'. In: *Nature Communications* 2.1 (2011), p. 490. DOI: 10.1038/ncomms1497 (cit. on p. 67).

[157] S. Stepanow, A. Lodi Rizzini et al. 'Spin Tuning of Electron-Doped Metal-Phthalocyanine Layers'. In: *Journal of the American Chemical Society* 136.14 (2014), pp. 5451–5459. DOI: 10.1021/ja501204q (cit. on p. 67).

[158] Y. Wang, S. Arabi et al. 'Symmetry mediated tunable molecular magnetism on a 2D material'. In: *Communications Physics* 4.1 (2021), p. 103. DOI: 10.1038/s42005-021-00601-8 (cit. on p. 67).

[159] M. Atzori, L. Tesi et al. 'Room-Temperature Quantum Coherence and Rabi Oscillations in Vanadyl Phthalocyanine: Toward Multifunctional Molecular Spin Qubits'. In: *Journal of the American Chemical Society* 138.7 (2016), pp. 2154–2157. DOI: 10.1021/jacs.5b13408 (cit. on p. 67).

[160] S. Cao, A. Rosławska et al. 'Energy funnelling within multichromophore architectures monitored with subnanometre resolution'. In: *Nature Chemistry* 13.8 (2021), pp. 766–770. DOI: 10.1038/s41557-021-00697-z (cit. on p. 67).

[161] H. Imada, K. Miwa et al. 'Real-space investigation of energy transfer in heterogeneous molecular dimers'. In: *Nature* 538.7625 (2016), pp. 364–367. DOI: 10.1038/nature19765 (cit. on p. 67).

[162] K. Kaiser, L.-A. Lieske et al. 'Charge-state lifetimes of single molecules on few monolayers of NaCl'. In: *Nature Communications* 14.1 (Aug. 2023), p. 4988. DOI: 10.1038/s41467-023-40692-1 (cit. on p. 68).

[163] P. Liljeroth, J. Repp and G. Meyer. 'Current-Induced Hydrogen Tautomerization and Conductance Switching of Naphthalocyanine Molecules'. In: *Science* 317.5842 (2007), pp. 1203–1206. DOI: 10.1126/science.1144366 (cit. on p. 68).

[164] J. Kügel, M. Leisegang et al. 'Remote Single-Molecule Switching: Identification and Nanoengineering of Hot Electron-Induced Tautomerization'. In: *Nano Letters* 17.8 (2017), pp. 5106–5112. DOI: 10.1021/acs.nanolett.7b02419 (cit. on p. 68).

[165] G. Reecht, N. Krane et al. 'π-Radical Formation by Pyrrolic H Abstraction of Phthalocyanine Molecules on Molybdenum Disulfide'. In: *ACS Nano* 13.6 (2019), pp. 7031–7035. DOI: 10.1021/acsnano.9b02117 (cit. on p. 68).

[166] F. Mohn, L. Gross et al. 'Imaging the charge distribution within a single molecule'. In: *Nature Nanotechnology* 7.4 (2012), pp. 227–231. DOI: 10.1038/nnano.2012.20 (cit. on p. 68).

[167] Z. Liu and X. Zhang. 'Density functional theoretical calculation of vanadium naphthalocyanine structure and vibrational spectrum'. In: *Materials Today Chemistry* 26 (2022), p. 101186. DOI: https://doi.org/10.1016/j.mtchem.2022.101186 (cit. on pp. 68, 75).

[168] G. Teobaldi, K. Lämmle et al. 'Chemical Resolution at Ionic Crystal Surfaces Using Dynamic Atomic Force Microscopy with Metallic Tips'. In: *Phys. Rev. Lett.* 106.21 (May 2011), p. 216102. DOI: 10.1103/PhysRevLett.106.216102 (cit. on p. 74).

[169] L. Gross, B. Schuler et al. 'Investigating atomic contrast in atomic force microscopy and Kelvin probe force microscopy on ionic systems using functionalized tips'. In: *Phys. Rev. B* 90.15 (Oct. 2014), p. 155455. DOI: 10.1103/PhysRevB.90.155455 (cit. on p. 74).

[170] D. Z. Gao, J. Grenz et al. 'Using Metallic Noncontact Atomic Force Microscope Tips for Imaging Insulators and Polar Molecules: Tip Characterization and Imaging Mechanisms'. In: *ACS Nano* 8.5 (2014). PMID: 24787716, pp. 5339–5351. DOI: 10.1021/nn501785q (cit. on p. 74).

[171] M. Ellner, N. Pavliček et al. 'The Electric Field of CO Tips and Its Relevance for Atomic Force Microscopy'. In: *Nano Letters* 16.3 (2016). PMID: 26840626, pp. 1974–1980. DOI: 10.1021/acs.nanolett.5b05251 (cit. on p. 74).

[172] R. Smoluchowski. 'Anisotropy of the Electronic Work Function of Metals'. In: *Phys. Rev.* 60.9 (Nov. 1941), pp. 661–674. DOI: 10.1103/PhysRev.60.661 (cit. on p. 74).

[173] S. Debnath, K. A. Haupa et al. 'Triggering near-infrared luminescence of vanadyl phthalocyanine by charging'. In: *Angewandte Chemie* 134.25 (2022), e202201577. DOI: https://doi.org/10.1002/ange.202201577 (cit. on p. 78).

[174] N. Krane. *Manual: Vibronics and VAT with Gaussian and Igor Pro*. 2020 (cit. on p. 79).

[175] S. Trishin, C. Lotze et al. 'Variations of Vibronic States in Densely Packed Structures of Molecules with Intramolecular Dipoles'. In: *physica status solidi (a)* 221.1 (2024), p. 2300105. DOI: 10.1002/pssa.202300105 (cit. on p. 83).

[176] W. Schottky. 'Zur Halbleitertheorie der Sperrschicht- und Spitzengleichrichter'. In: *Zeitschrift für Physik* 113.5 (1939), pp. 367–414. DOI: 10.1007/BF01340116 (cit. on p. 85).

[177] R. T. Tung. 'The physics and chemistry of the Schottky barrier height'. In: *Applied Physics Reviews* 1.1 (Jan. 2014), p. 011304. DOI: 10.1063/1.4858400 (cit. on p. 85).

[178] A. Kahn. 'Fermi level, work function and vacuum level'. In: *Mater. Horiz.* 3.1 (2016), pp. 7–10. DOI: 10.1039/C5MH00160A (cit. on p. 87).

[179] M. J. Mleczko, A. C. Yu et al. 'Contact Engineering High-Performance n-Type $MoTe_2$ Transistors'. In: *Nano Letters* 19.9 (2019). PMID: 31314531, pp. 6352–6362. DOI: 10.1021/acs.nanolett.9b02497 (cit. on p. 87).

[180] T. Shimada, F. S. Ohuchi and B. A. Parkinson. 'Work Function and Photothreshold of Layered Metal Dichalcogenides'. In: *Japanese Journal of Applied Physics* 33.5R (May 1994), p. 2696. DOI: 10.1143/JJAP.33.2696 (cit. on p. 87).

[181] L. A. H. Jones, Z. Xing et al. 'Band Alignments, Electronic Structure, and Core-Level Spectra of Bulk Molybdenum Dichalcogenides (MoS_2, $MoSe_2$, and $MoTe_2$)'. In: *The Journal of Physical Chemistry C* 126.49 (2022), pp. 21022–21033. DOI: 10.1021/acs.jpcc.2c05100 (cit. on p. 87).

[182] Bonnet, A., Conan, A. et al. 'Influence of the stoichiometry deviation on the electrical properties of $MoTe_2$-x'. In: *J. Phys. France* 49.5 (1988), pp. 803–811. DOI: 10.1051/jphys:01988004905080300 (cit. on p. 87).

[183] J. Chen, Z. Feng et al. 'Contact Engineering of Molybdenum Ditelluride Field Effect Transistors through Rapid Thermal Annealing'. In: *ACS Applied Materials & Interfaces* 9.35 (2017). PMID: 28816041, pp. 30107–30114. DOI: 10.1021/acsami.7b06739 (cit. on p. 87).

[184] S. Aftab, M. Samiya et al. 'A reversible and stable doping technique to invert the carrier polarity of $MoTe_2$'. In: *Nanotechnology* 32.28 (Apr. 2021), p. 285701. DOI: 10.1088/1361-6528/abe2cb (cit. on p. 87).

[185] M. Pfeiffer, A. Beyer et al. 'Controlled doping of phthalocyanine layers by cosublimation with acceptor molecules: A systematic Seebeck and conductivity study'. In: *Applied Physics Letters* 73.22 (Nov. 1998), pp. 3202–3204. DOI: 10.1063/1.122718 (cit. on p. 95).

[186] W. Gao and A. Kahn. 'Controlled p-doping of zinc phthalocyanine by coevaporation with tetrafluorotetracyanoquinodimethane: A direct and inverse photoemission study'. In: *Applied Physics Letters* 79.24 (Dec. 2001), pp. 4040–4042. DOI: 10.1063/1.1424067 (cit. on p. 95).

[187] M. Bendikov, F. Wudl and D. F. Perepichka. 'Tetrathiafulvalenes, Oligoacenenes, and Their Buckminsterfullerene Derivatives: The Brick and Mortar of Organic Electronics'. In: *Chemical Reviews* 104.11 (2004). PMID: 15535637, pp. 4891–4946. DOI: 10.1021/cr030666m (cit. on p. 95).

[188] J. Fraxedas, S. García-Gil et al. 'Modulation of Surface Charge Transfer through Competing Long-Range Repulsive versus Short-Range Attractive Interactions'. In: *The Journal of Physical Chemistry C* 115.38 (2011), pp. 18640–18648. DOI: 10.1021/jp2050838 (cit. on p. 95).

[189] T. R. Umbach, I. Fernandez-Torrente et al. 'Enhanced charge transfer in a monolayer of the organic charge transfer complex TTF-TNAP on Au(111)'. In: *Journal of Physics: Condensed Matter* 24.35 (Aug. 2012), p. 354003. DOI: 10.1088/0953-8984/24/35/354003 (cit. on p. 96).

[190] A. Yousofnejad. 'Structural and Electronic Properties of Organic Molecules on Monolayer Molybdenum Disulfide on Ag(111)'. PhD thesis. Freie Universität Berlin, 2021. DOI: 10.17169/refubium-35004 (cit. on p. 97).

Curriculum Vitae

The curriculum vitae is not published in the electronic version because of data protection.

List of Publications

Publications related to this thesis:

- J. R. Simon, D. Maksimov, C. Lotze, P. Wiechers, J. P. Guerrero Felipe, B. Kobin, J. Schwarz, S. Hecht, K. J. Franke and M. Rossi. 'Atomic-scale perspective on individual thiol-terminated molecules anchored to single S vacancies in MoS_2'. In: *Phys. Rev. B* 110.4 (2024), p. 045407. DOI: 10.1103/PhysRevB.110.045407

Publications not related to this thesis:

- O. Peters, N. Bogdanoff, S. Acero González, L. Melischek, J. R. Simon, G. Reecht, C. B. Winkelmann, F. von Oppen and K. J. Franke. 'Resonant Andreev reflections probed by photon-assisted tunnelling at the atomic scale'. In: *Nature Physics* 16.12 (2020), pp. 1222–1226. DOI: 10.1038/s41567-020-0972-z

Conference Contributions

2019

31.03. – 05.04. DPG Spring Meeting of the Condensed Matter Section, Regensburg, Germany
Poster Changing the Characteristic Critical Current in an STM Josephson Junction by Magnetic Adatoms

27.10. – 31.10. 704. WE-Heraeus-Seminar on "Exploring the Limits of Nanoscience with Scanning Probe Methods", Bad Honnef, Germany
Poster The alloy Mn_{88} Ni_{12}: An Intrinsically Spin-Polarised Tip Material?

2020

10.09. – 11.09. Online Symposium on Hybrid Inorganic/Organic Systems for Opto-Electronics 2020
Poster Structural and electronic properties of F6-TCNNQ on monolayers of MoS_2 investigated by STM/AFM

18.11. – 19.11. HIOS Young Researcher Workshop 2020 – Online Workshop
Poster Structural and electronic properties of F6-TCNNQ on monolayers of MoS_2 investigated by STM/AFM

2021

11.10. – 12.10. HIOS Young Researcher Workshop 2021 – Online Workshop
Talk *p*-Terphenyl-based thiols bound to top-layer sulphur defects on MoS_2/Au(111) investigated by STM

01.11. – 05.11. 756. WE-Heraeus-Seminar on "Faster, Smaller, Stronger, Brighter – Advances in Scanning Probe Techniques", Bad Honnef, Germany
Poster *p*-Terphenyl-based thiols bound to top-layer sulphur defects on MoS_2/Au(111) investigated by STM

2022

24.07. – 29.07. Bad Honnef Physics School “As thin as it gets: Physics of 2D Materials and Heterostructures", Bad Honnef, Germany

Poster Emergence of a singly-occupied state of *p*-terphenyl-based thiols bound to sulphur defects on MoS_2/Au(111)

04.09. – 09.09. DPG Spring Meeting of the Condensed Matter Section, Regensburg, Germany

Talk Emergence of a singly-occupied state of *p*-terphenyl-based thiols bound to sulphur defects on MoS_2/Au(111)

30.10. – 04.11. 747. WE-Heraeus-Seminar on "Molecular Functionality at Surfaces: Self Assembly, Manipulation, Reactivity and the Role of Decoupling”, Bad Honnef, Germany

Poster Emergence of a singly-occupied state of *p*-terphenyl-based thiols bound to sulphur defects on MoS_2/Au(111)

2023

26.03. – 31.03. DPG Spring Meeting of the Condensed Matter Section, Dresden, Germany

Poster Decoupling of Vanadyl-Naphthalocyanine from a Metal Substrate by Monolayer MoS_2

Acknowledgements

This thesis is not the work of only one person. Now that I can finally drop the royal We adopted in the main text, it is time to acknowledge those who made all this possible.

First of all, of course, Katharina. After I joined your group in 2016 as a fresh-faced bachelor student who most of the time thought they had an idea of what was happening, but truly did not, to letting me rejoin your group for my master project and then offering me a PhD position, I have spent now in total what must be six years working in your group. It has been a special time in my life, a formative time and that is by no small means thanks to you. Thank you for letting me join your group, for letting me work on your machines and for always having an open ear (and reading things at the very last minute on short notice). What I especially appreciate about you and probably what I will remember most is the incredible amount of knowledge and insight that you possess and are willing to share. In almost every discussion, meeting or just during general chit-chat, you had so many insightful comments about physics and also life in general that it has been truly a pleasure to have you as my boss.

Secondly, my second supervisor Wolfgang Kuch. Thank you, Wolfgang, for agreeing to be my second supervisor, even though you already had so many other students to take care of. Especially thank you for hosting me in your group seminar every year. Giving these talks always inspired me to reflect on the achievements of the past year and to get them into a coherently presentable form. After I have told you and your group members what seems like the same story three times, always with the addition of new insights that changed the picture almost completely, here it is now in its hopefully final form.

Other people, without whom this thesis would not have come to be, are Idan Tamir, Christian Lotze and Gaël Reecht.

Idan, even though you're not in the group anymore and probably will never even read this, you have been such an important figure at the beginning of my PhD. Without you and your unconditional help in the lab, I don't think I would have made it through the initial months or even the following years. Fuji – a machine with its problems and special quirks that you taught me how to properly handle, one we opened together so many times and which you taught me how to fix. It was also an incredibly fun time and I learned so much from you that I will probably remember forever, even though I haven't always heeded your advice. And no, I didn't break Fuji.

Chris, without you no gas-phase calculation would be in this thesis. Thank you for teaching me how to wrangle the incredibly uncooperative programs and more than once nudging me in the correct direction when some cryptic, undocumented error message popped up. But also in the real world your help was invaluable, be it soldering, spot-welding or picking up samples that weren't where they were supposed to be. I'll never forget looking through the window in Etna and seeing something that was not supposed to be there.

Gaël, the molecule wizard. Before evaporating any new molecule, I would go to you and you would have the answer on how to handle it. You were also the one who explained to me what those bananas I was seeing in the stacked spectra were. Starting in Kili during my masters, it probably would not have gotten anywhere without you there to

help. You were always ready to share your vast knowledge, to lend a helping hand and to give some sage advice.

Then of course there is the rest of AG Franke. Of all the current and former members of this group, there are a few who I *have* to mention here specifically.

Laëti, you were my first introduction to STM and that is a time I will never forget, even though we had our share of problems in the lab. You taught me STM and you continue to be an inspiration for me, but most importantly: a very dear friend. After joining the kindergarten office when I came back for my masters, it's always been fun and games and drama and deep philosophical discussions, and the 8th of March 2019 will always hold a special place in my heart. Thank you also for pulling me out of a deep hole when you returned, you helped me pull through. I wish you all the best in your future and I hope, or rather, I know that our paths will cross again.

Next, Martina and Jenny. Both of you have also played an important role in these last few years of my life. All our chats, airing our frustrations and overcoming them, comparing notes and discussions about physics, work and life and just everything, and a really nice, relaxing and just so congenial environment is what I appreciate so much about you two. Of course having similar interests also helps. I very much look forward to many more musical adventures, bouldering adventures, sewing adventures and gaming adventures with both of you.

Bharti, it's been such a joy to see you grow in the past years and I know that this growth will continue. You have a lot within you, don't forget that, and I'll gladly continue to hand out all sorts of unsolicited advice.

These acknowledgements are becoming long, so let's pick up the pace. Sergey, always up for a laugh, always up for some quick banter. It's been a lot of fun and I wish you all the best in the US and beyond. Verena, take good care of Fuji, the old lady. Also keep enjoying costumes and musicals and stay stylish. Paul, it was a pleasure having you as a bachelor student, even though Covid complicated matters, and I know that your technical expertise will serve you very well. Vibhuti, the discussions and talks we had, even though few, were always full of insight and new ideas, I appreciated them a lot. And: write it!

The whole of AG Franke, a truly special group with so many fun activities without which every day would have been very boring. Even though the pandemic sadly put a hold on many activities during three years of my PhD, where would we be without coffee club, cake club, ice club, volleyball club, boulder club and game nights? And of course the people: Birgit, Carlos, Carmen, Caroline, Daniela, Eva, Florian, Giada, Jannik, Juan Pablo, Junyoung, Katharina (die Kleine), Lisa, Margarete, Melvin, Micha, Nils, Nils, Nino, Olga, Olof, Terra, and everyone else I forgot to mention.

Last but not least, my family and friends. Thank you to my parents for always supporting me in all my endeavours, I cannot properly express in words how grateful I am for all your support throughout my life. 本当にありがとう。 Daek! All misplaced commas are entirely my own.

Thank you also to my Musical family who have given me much needed respite from science and allowed me to escape into worlds that we create ourselves.

Selbstständigkeitserklärung

Ich erkläre gegenüber der Freien Universität Berlin, dass ich die vorliegende Dissertation selbstständig und ohne Benutzung anderer als der angegebenen Quellen und Hilfsmittel angefertigt habe. Die vorliegende Arbeit ist frei von Plagiaten. Alle Ausführungen, die wörtlich oder inhaltlich aus anderen Schriften entnommen sind, habe ich als solche kenntlich gemacht. Diese Dissertation wurde in gleicher oder ähnlicher Form noch in keinem früheren Promotionsverfahren eingereicht.
Mit einer Prüfung meiner Arbeit durch ein Plagiatsprüfungsprogramm erkläre ich mich einverstanden.

Berlin, den 28.03.2024

_____

J. Rika Simon